Structural and magnetic properties and superconductivity in $Ba(Fe_{1-x}TM_x)_2As_2$

(TM=Ru, Mn, Cr/Co, Mn/Co) single crystals

by

Alexander Nicholas Thaler

A dissertation submitted to the graduate faculty

in partial fulfillment of the requirements for the degree of

DOCTOR OF PHILOSOPHY

Major: Condensed Matter Physics

Program of Study Committee:

Paul C. Canfield, Major Professor

Ruslan Prozorov

Bruce Harmon

William McCallum

John Lajoie

Iowa State University

Ames, Iowa

2012

DEDICATION

I would like to dedicate this thesis to friends and family, without whom I would never have been able to complete this work. I would especially like to thank my parents for always being supportive and helpful, even in the most trying of times.

TABLE OF CONTENTS

LIST OF TABLES

LIST OF FIGURES

ACKNOWLEDGEMENTS

First and foremost, I would like to thank Professor Paul Canfield for his guidance, support and patience throughout this research. I would also like to thank my committee members for their efforts and contributions to this work.

I would like to thank Ni Ni for teaching me the tricks of the trade of sample growth; Shuang Jia and Eun Deok Mun for helping me to understand and interpret transport and magnetic measurements; and Yuri Janssen for teaching me how to use x-ray machines and encouraging me to always question what's going on. I would like to thank Jiaqiang Yan for his help synthesizing precursor materials and Kevin Dennis for showing me how to use so many of his cool toys. Alfred Kracher and Warren Straszheim provided invaluable help performing WDS analysis.

I would also like to thank group members past and present, Stella Kim, Ran Sheng, Estelle Colombier, Halyna Hodovanets, Milton Torikachvili and Sergey Bud'ko, for their work on my samples in our lab. Daniel Pratt, Mingyu Kim, Greg Tucker, Shibabrata Nandi, Andreas Kreyssig, Rob McQueeney and Alan Goldman did wonderful scattering work that I am fascinated by. Makariy Tanatar and Erick Blomberg made detailed transport and magneto-optical measurements which I think are beautiful.

I would finally like to thank Ryan Gordon and Rafael Fernandes for always entertaining my questions, no matter how wild, and my past and present graduate school roommates – Jake Hoberg, Brett McCarty, Sarah Carney, Tim Sklenar, Lindy, Knox, Castle, Ryan Dierks, Marcio Zaccaron, Kayce Rich, John Sappington and Joe Moellers – for putting up with me.

CHAPTER 1. Introduction

Superconductivity has been one of the most studied fields in condensed matter physics since its discovery more than a century ago by Onnes (1911). Immense experimental and theoretical attention has been focused on it. In addition to pure elements and alloys, many families of intermetallic compounds and oxides have been discovered to superconduct and it has become clear that the phenomenon is not as rare as initially thought.

In addition to the nearly half of the elements that are superconducting in their pure form, thousands of superconducting compounds have been found. The highest superconducting transition temperature (T_c) found in an elemental superconductor is 9.5 K in niobium (Chou et al. (1958)). The first compound which exceeded this was NbN, with $T_c \sim 16$ K. Over the first 65 years of the study of superconductors, T_c gradually increased to about 25 K in Nb_3Ge. The holy grail of this period was a compound that would superconduct at room temperature, or at least in liquid nitrogen, which is considerably cheaper and easier to obtain than the cryogens used for lower temperatures (such as liquid helium). $(La_{1-x}Ba_x)CuO_4$, the first high-T_c superconductor, was discovered in 1986 with a seemingly modest T_c of 30 K (Bednorz and Müller (1986)) . What wasn't clear at that time, from T_c alone, was that this was the first of a new class of superconductors. It took only nine months for T_c to make a dramatic increase to 93 K in $YBa_2Cu_3O_{7-\delta}$ (Wu et al. (1987)), above the boiling point of liquid nitrogen (77 K). This new family of superconductors, the high-T_c cuprates, proved to be huge and showed great promise for increasing T_c further. By 1993, T_c was as high as 138 K at ambient pressure (Chu et al. (1993)), and even higher under applied pressure. While this is still well below room temperature, it is high enough that it is easily obtainable with good closed-cycle refrigeration.

For more than 20 years, the cuprates were the only known "high-T_c" compounds. This changed in 2008, when Kamihara et al. (2008) found superconductivity at 26 K in $La(O_{1-x}F_x)FeAs$

$(0.05 < x < 0.12)$. Once again, the relatively modest T_c hid just how big a deal this new family was. Within a month, T_c had risen to 55 K at ambient pressure in $NdFeAsO_{1-x}F_x$ (Zhi-An et al. (2008)). While still below the boiling point of liquid nitrogen, this is still well above the base temperature ~20 K) of simple closed-cycle refrigerators. Unfortunately, large single crystals of these RFeAsO (1111) compounds remain elusive, limiting the ability to do research on this system.

Later that year, a related compound was discovered by Rotter et al. (2008a). This compound, $(Ba_{1-x}K_x)Fe_2As_2$, had a max T_c of ~38 K. Whereas this is considerably lower than the maximum in the 1111 series, this new 122 series proved to be much more willing to form large single crystals (Ni et al. (2008a)). Unfortunately, these K substituted samples were found to be inhomogeneous when grown with a Sn flux, even from layer to layer within one piece (Ni et al. (2008a)). Fortunately, a related substitution series was discovered shortly thereafter. Transition metal substitution on the Fe site was found to induce superconductivity up to 24 K (Sefat et al. (2009a); Ni et al. (2008b)). While this is considerably lower than the 38 K found in K-substitution, transition metals (TM) were found to easily substitute much more uniformly within the single crystals. The change from K, which is both volatile and highly reactive, to the much more stable transition metals also meant that a self flux could be used (see Chapter 3), allowing much larger crystals to be synthesized.[1] The homogeneity in this series (for TM=Co, Ni, Rh and Pd) is quite excellent as well: typical 2σ spread of x_{WDS} is $\lesssim 0.003$ across the sample surface. The large volumes and excellent homogeneity made these samples excellent candidates for detailed study using advanced methods.

Luo et al. (2008) showed that K substitution could be achieved through this same self-flux method, avoiding the volatility of K by pre-reacting it with Ba. Homogeneity as determined by superconducting transition width is excellent and T_c remains high, ~36 K, but the crystals formed this way are only ~1 mm^2, which is smaller than both TM substituted samples and Sn grown K substituted ones (which can be as large as several mm on a side).

$BaFe_2As_2$ crystallizes in the $ThCr_2Si_2$ structure – more formally the $I4/mmm$ space group.

---

[1]To my knowledge, the largest crystal formed this way was a single ~700 mg sample of Co-substituted $BaFe_2As_2$ that had a volume of more than 0.2 cm^3.

The Ba atoms are interleaved between FeAs planes. $BaFe_2As_2$ was also found to have an transition characteristic of a spin-density wave transition at ~ 140 K (Rotter et al. (2008b)). Above this temperature, $BaFe_2As_2$ is a poor metal with little temperature dependence in its resistivity. Below, the resistivity drops rapidly as the material enters an antiferromagnetic state and spin disorder scattering is reduced. A drop in the magnetic susceptibility is also observed at this temperature. Rotter et al. (2008b) showed that this change is associated with a structural phase transition. Below 140 K, several of the peaks seen in powder x-ray diffraction (XRD) are seen to first broaden then split as the temperature is decreased. This low temperature phase belongs to the a different category: the orthorhombic $Fmmm$ space group. A neutron scattering study of the magnetic structure found that the structural and magnetic phase transitions occur at (nearly) the same temperature (Huang et al. (2008); Pratt et al. (2011)).
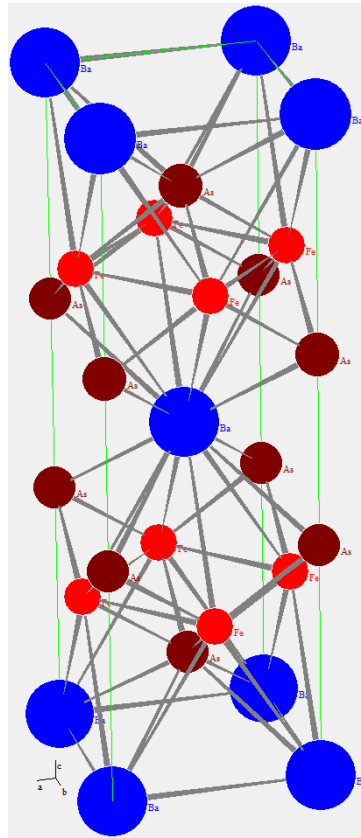
Figure 1.1: Crystallographic structure of $BaFe_2As_2$. Blue are Ba, red are Fe, maroon are As.

A systematic study of the substitution dependence of this family of compounds seemed the logical next step. Turning various chemical tuning dials and noting the changes in structural, magnetic and transport properties – including the emergence of superconductivity – can provide valuable insight into what the origin of these properties may be. Whereas K on the Ba site and P on the As site both proved to induce superconductivity, other substitutions on these sites were largely fruitless. On the other hand, a *large* number of 3d, 4d and 5d transition metals have been found to successfully substitute for Fe, and many of these have been found to induce superconductivity. The superstar of the TM substitution family is $Ba(Fe_{1-x}Co_x)_2As_2$, which has shown excellent behavior in terms of transition temperature, homogeneity, reproducability and crystal size. Ni, Rh, and Pd have shown similar behavior. Meanwhile, Cu was shown to barely induce superconductivity (Ni et al. (2010)) and Cr has been shown not to induce it at all (Sefat et al. (2009b); Bud'ko et al. (2009)). I will discuss two other TM substitutions in this thesis: Chapter 5 will discuss Ru substitution which induces superconductivity and Chapter 6 will cover Mn substitution which does not (see also Rullier-Albenque et al. (2010) or Thaler et al. (2010) for Ru and Thaler et al. (2011) for Mn).

During my thesis work, I have expanded the TM substitutions to Ru and Mn (which will be discussed in Chapters 5 and 6) and collaborated extensively with other research groups on studies of many TM substitutions of $BaFe_2As_2$, much of which I will outline in Chapter 9. For perspective, Chapter 2 gives some background into superconductivity from both phenomenological and theoretical points of view. Chapter 3 will outline the growth and characterization methods I employed. Chapter 7 will show some results of my investigation of the somewhat more complex double-substitution systems $Ba(Fe_{1-x-y}Co_xCr_y)_2As_2$ and $Ba(Fe_{1-x-y}Co_xMn_y)_2As_2$. Chapter 8 will briefly present some work on heat treated samples of $Ba(Fe_{1-x}Co_x)_2As_2$ and $Ba(Fe_{1-x-y}Co_xCr_y)_2As_2$.

CHAPTER 2.   Overview of superconductivity

Superconductivity differs from perfect conductivity in that a superconductor displays nearly perfect diamagnetism in addition to zero resistance. This is known as the Meissner effect, and the first phenomenological theory of superconductivity which took it into account was described by London and London (1935). Unfortunately, while the Londons' theory is qualitative, it is also an outgrowth of classical electrodynamics, and superconductivity is fundamentally a quantum phenomenon, so while it is a correct description of the macroscopic behavior of superconductors in an applied magnetic field, it cannot describe the underlying microscopic behavior. Ginzburg-Landau theory also does not describe the microscopic behavior, but it tries to describe the phenomenology of the superconducting phase transition by taking quantum mechanics into account, and introduces the electrons' wavefunction, $\psi(\mathbf{r})$, as the order parameter (Ginzburg and Laundau (1950)). Because of the accurate description of the behavior of the phase transition even under applied field, one of the its largest successes was the prediction of type-II superconductivity (Abrikosov (1957)).

It was not until 1957 that a successful microscopic theory of superconductivity was introduced. Bardeen, Cooper and Schrieffer (BCS) published three papers (Cooper (1956); Bardeen et al. (1957a,b)) that led to a microscopic understanding of what a superconductor is, rather than simply a description of how one behaves. The first observation of the BCS theory is that any pair of electrons that experience an arbitrarily small net attractive interaction will form a bound state with $\overleftarrow{k}$ and $\overrightarrow{k}$ and spins $\uparrow$ and $\downarrow$. Assuming that the interaction is phonon mediated and describing the electron-phonon interaction as a constant, an energy gap between the ground state and first excited state can be found. This is fortunate, as a previous microscopic theory had proposed that such a gap might be responsible for superconductivity Bardeen (1955)). Finally, BCS theory made detailed – and reasonably good – quantitative predictions

of the thermodynamic properties of elemental superconductors. BCS theory was an excellent start upon which further, more realistic descriptions of the interaction were constructed (Eliashberg (1960)). Magnetism and superconductivity have an interesting relationship. Nonmagnetic and magnetic impurities require special, and separate, descriptions. These were first provided by Abrikosov and Gor'kov (1958), Anderson (1959) and Abrikosov and Gor'kov (1961). Furthermore, the upper critical field of type-II superconductors was systematically studied by Werthamer et. al. (Helfand and Werthamer (1964, 1966); Werthamer et al. (1966); Hohenberg and Werthamer (1967); Werthamer and McMillan (1967)).

Although BCS theory and its derivatives work extremely well for conventional superconductors, they fails to completely describe other families of superconductors, such as the high-T_c cuprates and heavy fermion materials. Quick fixes to BCS theory such as altering the pairing mechanism from being mediated by phonons to spin fluctuations, polarons or magnons have failed to adequately explain all features of these other families. Nevertheless, the fundamental idea of BCS theory that electrons form pairs through some kind of quasiparticle interaction which allows them to fall into the same state with an energy gap required for excitations above this appears to hold even in these non-conventional superconducting materials.

As a basic understanding of the phenomenology and mechanism of superconductivity is essential for following more complex work, I will give a brief introduction to both in this chapter. I will then outline how phase diagrams for basic superconductors and high-T_c, heavy fermion and FeAs compounds provide insight and context for the systems studied in this thesis.

2.1   Phenomenology and Macroscopic Theory

As the name implies, one of the primary properties of superconductors is zero resistance. It was this property which was first discovered by Onnes (1911) in mercury. Above the critical temperature T_c (4.15 K in mercury), the material behaves as a normal metal with finite resistance. Below T_c, the resistance rapidly drops to zero. This transition can be shown to be second order.

The second primary property of superconductors, and the one distinguishing them from what would be expected for a classical perfect conductor, is perfect diamagnetism, as observed

by Meissner and Ochsenfeld (1933). Mere perfect conductivity would not predict this behavior. Let us assume a perfect metal whose behavior is described by the classical Maxwell's equations and explore what happens. One of the basic measurements we perform on superconducting materials is low field $M/H(T)$. This may be performed in one of two ways: either we cool under zero field to below T_c, apply field and then warm back up measuring the magnetic response, or we apply field above T_c and then cool down into the superconducting state. In practice, these sequences are used for different purposes. The first is called zero field cooled (ZFC), the second field cooled (FC). Under ZFC conditions and considering Maxwell's equation

$$\mathbf{j}\rho = -\frac{1}{c}\frac{\partial \Phi}{\partial t} \tag{2.1}$$

zero resistance below T_c leads to $\mathbf{B} = const$. Since $\mathbf{B} = 0$ before switching on, it must remain zero after the field is applied. Now consider the FC situation: $\mathbf{B} \neq 0$ above T_c, so Eq. 2.1 says that it must remain nonzero below T_c (see Fig. 2.1(a)). This is not what Meissner and Ochsenfeld observed. Instead, they found that $\mathbf{B}$ is always zero, for both ZFC and FC sequences (see Fig. 2.1(b)). That this cannot be explained by perfect conductivity means that it must be a separate, intrinsic property of the superconducting state. During the superconducting transition, the flux is expelled by the induction of large currents in the surface region. This is commonly known as the Meissner effect.

Using the Meissner effect ($\mathbf{B} = 4\pi\mathbf{M} + \mathbf{H}_0 = 0$) allows us to determine that the work done by an external field is

$$W = -\int_0^{H_0} \mathbf{M}d\mathbf{H} = \frac{\mathbf{H}d\mathbf{H}_0}{4\pi} = \frac{H^2}{8\pi}, \tag{2.2}$$

giving a Helmholtz free energy

$$F_s(H) = F_s(H = 0) + \frac{H^2}{8\pi}. \tag{2.3}$$

So when

$$F_s(H_c) = F_n = F_s(H = 0) + \frac{H_c^2}{8\pi} \tag{2.4}$$

the superconducting state is destroyed. We call H_c the thermodynamic critical field.
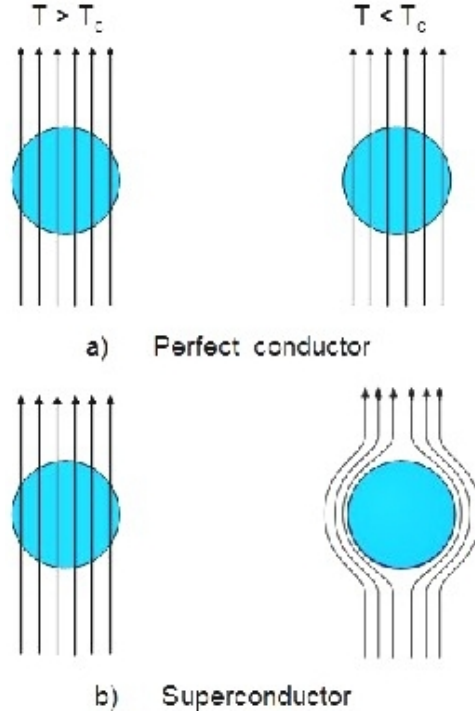
Figure 2.1: B from an applied H in a perfect conductor (a) and a superconductor (b).

2.1.1 Ginzburg-Landau Theory

Ginzburg-Landau theory macroscopically describes the behavior of superconductors, including quantum effects. It assumes a second order phase transition, which is correct for ZFC. It also assumes that the conduction electrons in a superconductor behave in a coherent manner, allowing them to be described by a single wave function – with a possible phase difference – $\psi(\mathbf{r}) = |\psi(\mathbf{r})| \, e^{i\phi}$. Finally, it assumes that ψ can be used as the order parameter. We write the Gibbs free energy as

$$G_s(H) = G_n + \int \left(\frac{\hbar^2}{2m^*} \left| \nabla \psi - i\frac{e^*}{\hbar c} \mathbf{A}\psi \right|^2 + a\,|\psi|^2 + \frac{b}{2}\,|\psi|^4 + \frac{B^2}{8\pi} - \frac{B \cdot H}{4\pi} \right) dV \qquad (2.5)$$

For $T \sim T_c$, we say that

$$a(T) \;=\; a_0 \left(\frac{T}{T_c} - 1 \right) \qquad (2.6)$$

$$b(T) \;=\; b_0. \qquad (2.7)$$

Minimizing G_s with respect to ψ and $\mathbf{A}$, we get two coupled equations:

$$\begin{cases} \frac{\partial G_s}{\partial \psi} = \int \left(\frac{\hbar^2}{m^*} \left[\frac{e^{*2}}{\hbar^2 c^2} \mathbf{A}^2 |\psi| \right] + 2a |\psi| + 2b |\psi|^3 \right) dV = 0 \\ \frac{\partial G_s}{\partial \mathbf{A}} = \int \left(\frac{\hbar^2}{m^*} \frac{e^{*2}}{\hbar^2 c^2} \mathbf{A} |\psi|^2 \right) dV = 0 \end{cases} \qquad (2.8)$$

.

We must now define two characteristic lengths for a superconductor. The first is the coherence length

$$\xi = \sqrt{\frac{\hbar^2}{2m^*|a|}} \qquad (2.9)$$

over which ψ displays significant variation. The other is the penetration depth

$$\lambda = \sqrt{\frac{m^* c^2 b}{4\pi e^{*2} |a|}}, \qquad (2.10)$$

which is the depth to which an applied magnetic field penetrates (Tinkham (2004)).

One victory of Ginzburg-Landau theory is the prediction of type-II superconductivity. Defining $\kappa = \frac{\lambda}{\xi}$, we can make a statement about the sign of the interface energy σ_{ns}.

$$\kappa < \frac{1}{\sqrt{2}} \quad \Rightarrow \quad \sigma_{ns} > 0 \qquad (2.11)$$

$$\kappa > \frac{1}{\sqrt{2}} \quad \Rightarrow \quad \sigma_{ns} < 0. \qquad (2.12)$$

In the first case, the formation of an interface between normal and superconducting states is not energetically favorable. We call such materials type-I superconductors. In these materials, superconductivity is destroyed for $H > H_c$. Most, but not all, elemental superconductors are type-I.

In the second case, the interface formation is energetically favorable. When $\lambda \gg \xi$, $\mathbf{B}$ penetrates much further into the sample than the variation range of the order parameter, which means that a mixture of superconducting and normal states can exist. These are called type-II superconductors. In such materials, there are two critical fields, H_{c1} and H_{c2}. When $H < H_{c1}$, the average B inside the sample is zero and it shows full Meissner expulsion as described above. When $H_{c1} < H < H_{c2}$, the magnetic field penetrates into the sample and it is divided into normal and superconducting domains parallel to $\mathbf{H}_{ext}$. The normal domains are vortices of radius $\sim \xi$, and the density of these vortices increases up to $H = H_{c2}$, at

which point the sample becomes completely normal. Several elemental superconductors – niobium, vanadium and technetium – as well as all non-elemental superconductors are type-II, including conventional superconductors composed of multiple elements, the high-T_c cuprates, heavy fermion materials, and the iron arsenides.

For a tetragonal type-II superconductor (the family to which the $I4/mmm$ BaFe$_2$As$_2$ compounds belong),

$$H_{c1}^{\perp c} = \frac{\Phi_0}{4\pi\lambda_{ab}\lambda_c}(\ln(\kappa_{ab} + c) \qquad H_{c2}^{\perp c} = \frac{\Phi_0}{2\pi\xi_{ab}\xi_c} \tag{2.13}$$

$$H_{c1}^{\parallel c} = \frac{\Phi_0}{4\pi\lambda_{ab}^2}(\ln(\kappa_c + c) \qquad H_{c2}^{\parallel c} = \frac{\Phi_0}{2\pi\xi_{ab}^2} \tag{2.14}$$

where the elementary flux quantum $\Phi_0 = 2.07 \times 10^{-7}$ Oe cm^2. For a single-gap material, $c = 0.08$. The anisotropic H_{c2} parameter is defined as $H_{c2}^{\perp c}/H_{c2}^{\parallel c} = \xi_{ab}/\xi_c$. The lower critical field H_{c1} is often a small field, on the order of a few tens of Oe. The upper critical field H_{c2} can be as high as several 100's of kOe.

One problem with applying Ginzburg-Landau theory to the iron arsenides is that they are two-band materials. A discussion of two gap materials is beyond the scope of this work, but can be found in Kogan and Schmalian (2011).

2.2 Microscopic Theory

2.2.1 BCS Theory

A key clue to a microscopic explanation of superconductors came from what is called the isotope effect. Maxwell (1950) (using ^{198}Hg) and Reynolds et al. (1950) (using samples with average A=199.7, 202.0 and 203.4) found that different isotopes of mercury have different T_c. Maxwell (1950) observed an increase of about 0.021 K and Reynolds et al. (1950) found shifts between +0.011 K (A=199.7) and -0.024 K (A=203.4). This suggested phonon mediation as the mechanism by which the electrons were coupled. Quantitatively, the isotope effect states that $T_cM^\alpha = const.$, with M the mass of the isotope. BCS theory simplifies the math quite a bit by assuming, for example, constant electron-phonon interaction and a spherical Fermi surface. Later theories, such as that of Eliashberg, considered a more realistic situation involving ω

dependent electron-phonon interaction and band structure.

Frohlich (1952) showed that electrons can indirectly interact with each other in a crystal by emitting and absorbing phonons. e_1 with k_1 emits a phonon and goes to k_1'. e_2 with k_2 then absorbs this phonon and goes to k_2'. This interaction means that electrons within $\hbar\omega_D$ of the Fermi surface are attractive to each other. Cooper (1956) considered two electrons in an attractive potential and found that the binding energy is always negative no matter how small the attraction is.

BCS theory combines these two: assuming that the attractive potential is mediated by the phonon scattering, Bardeen, Cooper and Schrieffer found that electron pairs within $\hbar\omega_D$ of the Fermi surface are formed and scattered from inside r_F to outside of it, lowering the potential energy while increasing the kinetic energy. If the potential energy is decreased by more than the kinetic energy is increased, then the ground state is no longer the state in which all electrons are in states within the Fermi surface, but instead one in which some states above E_F are occupied and some below E_F are empty. To maximize the number of these pairs that may be formed, the electrons in each pair must have momentum of equal magnitude but opposite direction, as well as antiparallel spin. If the spins for a singlet state ($S = 0$), then the spatial wave function must have even parity ($L = 0, 2, 4, \cdots$). If the spins form a triplet state ($S = 1$), then the spatial wave function must have odd parity ($L = 1, 3, 5, \cdots$)

BCS theory makes several assumptions to simplify calculation. First, the Fermi surface is assumed to be spherical. Second, the pair is assumed to have $L = 0$ and $S = 0$. Third, the electron-phonon interaction $V_{kk'}$ is assumed to be a constant:

$$
V_{kk'} = \begin{cases} -V & |\epsilon_k| \leq \hbar\omega_D \ \& \ |\epsilon_{k'}| \leq \hbar\omega_D \\ 0 & |\epsilon_k| > \hbar\omega_D \ \& \ |\epsilon_{k'}| > \hbar\omega_D \end{cases} \tag{2.15}
$$

with

$$
\epsilon_k = \frac{\hbar^2 k^2}{2m} - \frac{\hbar^2 k_f^2}{2m} \tag{2.16}
$$

We can express the excitation energy as

$$
E_k = \sqrt{\epsilon_k^2 + \Delta^2}, \tag{2.17}
$$

where Δ is referred to as the "energy gap". To break one Cooper pair, an energy of at least 2Δ is needed. This gap is temperature dependent, and shrinks to zero as $T \to T_c$.

2.2.1.1   Isotope Effect as a Probe of the Pairing Mechanism

Since the energy gap Δ is proportional to ω_c, Δ should vary as $M^{-\alpha}$, with $\alpha = 1/2$ for phonon mediated compounds. Since T_c and H_c are linearly dependent on Δ, they should scale as $M^{-\alpha}$ as well. By varying M via a change in the isotope of otherwise identical materials, we can measure α. If $\alpha \sim 1/2$, then that is strong evidence that the superconductor being studied is phonon mediated. The drastic deviation from prediction in the cuprate superconductors suggested very strongly that they were not phonon mediated (Batlogg et al. (1987); Franck et al. (1991); Zech et al. (1994); Zhao et al. (2001); Khasanov et al. (2004, 2008); Tallon et al. (2005); Chen et al. (2007)). The isotope effect showed its importance more recently by helping to demonstrate that MgB_2 must be phonon-mediated, as there is a ~ 1.0 K shift between samples prepared with ^{10}B and those prepared with ^{11}B (Bud'ko et al. (2001)).

If the isotope effect in the iron arsenides could be shown to have $\alpha \sim 1/2$, then it would be strong evidence that these compounds are phonon mediated. By the same token, $\alpha \nsim 1/2$ would suggest that these compounds are not primarily phonon mediated. Early results were very mixed, with some giving predictions roughly in line with phonon mediation and others giving radically different ones: α varied from ~ 0.8 down to ~ -0.5 (Liu et al. (2009); Shirage et al. (2009, 2010); Khasanov et al. (2010b)). Fortunately, there is a solution: Khasanov et al. (2010a) noted that changing the Fe isotope changed the c lattice parameter in $FeSe_{1-x}$ ($\Delta c/c_0 > 0$), $Ba_{0.6}K_{0.4}Fe_2As_2$ ($\Delta c/c_0 < 0$) and $SmFeAsO_{1-y}$ ($\Delta c/c_0 \gtrsim 0$). As anyone familiar with a stringed instrument will know, the natural frequency of an oscillator is affected by both the mass of the oscillator and its length ($f_{\text{string}} \propto \frac{1}{l\sqrt{\lambda}}$, where λ is the linear mass density), so a change in the separation between the oscillating elements can also change ω_c, which will change T_c. By rewriting $\alpha = \alpha_{struct} + \alpha_M$ and accounting for α_{struct} through lattice parameter data, they were able to show that $\alpha_M \sim 0.35 - 0.4$ for all three compounds. While this is a large effect and has α not *too* far from $\alpha_{\text{phonon}} = 1/2$, Wu and Phillips (2011) showed that it can still be consistent with a non-phononic mechanism for superconductivity in multi band

superconductivity.

2.2.1.2 Energy Gap as a Probe of the Pairing Mechanism

The gap is a very important quantity because it is closely related to the order parameter. The Ginzburg-Landau order parameter can be shown to be the pair wavefunction in the microscopic theory. This means that if we measure the magnitude and shape (including anisotropy) of the superconducting gap, we can glean information about the pairing symmetry, which is critical in determining the pairing mechanism. Phonon coupling, as in BCS theory, predicts an isotropic s-wave gap. High-T_c cuprates have been shown to be d-wave. Since phonon coupling gives a nodeless energy gap, this result eliminates phonon coupling as a possible pairing mechanism in this system, a result consistent with the isotope effect.

The gap symmetry of the FeAs family of superconductors was not immediately clear. Nodeless gaps were directly observed in $Ba_{1-x}K_xFe_2As_2$, $Ba(Fe_{1-x}Co_x)_2As_2$, $K_xFe_{2-y}Se_2$ and $FeTe_{1-x}Se_x$ (Ding et al. (2008); Terashima et al. (2009); Zhang et al. (2011); Miao et al. (2012)). At the same time, signatures of noded gaps were seen in LaOFeP, LiFeP, KFe_2As_2, $BaFe_2(As_{1-x}P_x)$, $Ba(Fe_{1-x}Ru_x)_2As_2$ and FeSe (Fletcher et al. (2008); Hashimoto et al. (2010, 2012); Nakai et al. (2010); Dong et al. (2010); Yamashita et al. (2011); Song et al. (2011); Qiu et al. (2012)). Until recently, no direct measurement of the gap structure was reported, nor was the location of the nodes known. Zhang et al. (2012) used Angle Resolved Photoemission Spectroscopy (ARPES) to make detailed measurements of the gap around the δ and η electron surfaces as well as the α, β and γ hole surfaces. They found strong evidence for a circular line node on the largest hole surface. This eliminates d-wave pairing as a possible origin of the nodes seen in the gap, and suggests that a symmetry called $s^{\pm}$ is the most likely candidate. $s^{\pm}$ is fully gapped with no nodes, but it displays four-fold symmetry instead of the fully circular symmetry seen with single band s-wave. While this does not rule out phonon mediated superconductivity as d-wave symmetry would, but since simple, one-band phonon mediation predicts s-wave symmetry, it also means that something more complex is likely to be happening here.

2.2.2 Impurity Effects

The Hamiltonian of the interaction between the impurities and conduction electrons can be written as (Abrikosov and Gor'kov (1961); Maple et al. (2008); Gor'kov (2008))

$$H_{int} = \sum_a \int \left(U_0(\mathbf{r} - \mathbf{r}_a) + U_{so}(\mathbf{r} - \mathbf{r}_a) + U_{ex}(\mathbf{r} - \mathbf{r}_a) \right) \psi^+(\mathbf{r}) \psi(\mathbf{r}) d^3\mathbf{r}. \tag{2.18}$$

Here, $\mathbf{r}_a$ is the position of impurity atom a and the summation runs over all the impurities. U_0 is the interaction energy of an electron and impurity without considering the effects of the impurity. U_{so} is the spin-orbit interaction energy between the vector potential associated with the spin of the impurities and the momentum of the conduction electrons. U_{so} does not change the equations determining T_c and Δ, so it does not affect the thermodynamic properties; it only affects the magnetic properties. U_{ex} is the exchange energy between $\mathbf{J}_a$ and $\mathbf{S}_e$. This term breaks the time-reversal invariance, which gives non-trivial contributions to T_c and the thermodynamic properties in alloys. For transition metal impurities, $\mathbf{L}$ is quenched, so the exchange interaction can be written as

$$U_{ex} = -2I\mathbf{S} \cdot \sigma \tag{2.19}$$

where I is the coupling between $\mathbf{S}_a$ and $\mathbf{S}_e$, $\mathbf{S}$ is the spin of the impurity atoms and σ is the spin of the conduction electrons. For rare earth impurities, $\mathbf{J} = \mathbf{L} + \mathbf{S}$, so

$$U_{ex} = -2I(g_J - 1)\mathbf{J} \cdot \sigma. \tag{2.20}$$

U_{so} and U_{ex} are related to the contributions from the impurity spin and will be present in the magnetic case.

For nonmagnetic, isoelectronic impurities,

$$\ln \left[\frac{T_{c0}}{T_c} \right] = \Omega \left[\phi \left(\frac{1}{2} + \frac{\mu}{2} \right) - \phi \left(\frac{1}{2} \right) \right] \tag{2.21}$$

where $\phi(x)$ is the digamma function, $\mu = \hbar/2\pi k_B T_c \tau$ and Ω is the gap anisotropy. Since $\Omega = 0$ for s-wave superconductors, nonmagnetic, isoelectronic impurities cannot change the gap size, which means they cannot alter the transition temperature. Since BCS theory also says that T_c is related to the Debye frequency and density of states, the change of density of states from non-isoelectronic impurities can lead to changes in T_c in an isotropic s-wave superconductor.

The presence of magnetic impurities suppresses T_c even in isotropic s-wave superconductors:

$$\ln\left[\frac{T_{c0}}{T_c}\right] = \phi\left(\frac{1}{2} + \frac{\mu_m}{2}\right) - \phi\left(\frac{1}{2}\right). \tag{2.22}$$

or

$$\ln\left[\frac{T_{c0}}{T_c}\right] = \phi\left(\frac{1}{2} + 0.14\frac{\alpha T_{c0}}{\alpha_c T_c}\right) - \phi\left(\frac{1}{2}\right) \tag{2.23}$$

where α is the pair-breaking parameter $\frac{1}{\tau}$. For rare earth impurities,

$$\alpha = \frac{1}{\tau} = \frac{n_i}{\hbar}\left[\frac{D(E_f)}{2k_B}\right]I^2(g_J - 1)J(J+1). \tag{2.24}$$

This means that

$$\ln\left[\frac{T_{c0}}{T_c}\right] = \phi\left(\frac{1}{2} + 0.14\frac{n_i T_{c0}}{n_{ic} T_c}\right) - \phi\left(\frac{1}{2}\right) \tag{2.25}$$

where n_{ic} is the critical impurity concentration when T_c is completely suppressed. For low n_i, $\frac{T_c}{T_{c0}}$ is suppressed linearly with $\frac{n_i}{n_{ic}}$:

$$\frac{T_c}{T_{c0}} = 1 - \frac{\pi\hbar}{4k_B\tau} = 1 - 0.691\frac{n_i}{n_{ic}} \tag{2.26}$$

The rate of suppression of $T_c(n_i)$ is (Maple et al. (2008))

$$\left.\frac{dT_c}{dn_i}\right|_{n_i \to 0} = -\left[\frac{\pi^2 D(E_f)}{2k_B}\right]I^2(g_J - 1)^2 J(J+1), \tag{2.27}$$

so in the dilute limit,

$$\frac{T_c}{T_{c0}} = 1 - \left[\frac{\pi^2 D(E_f)}{2k_B}\right]I^2(g_J - 1)^2 J(J+1). \tag{2.28}$$

Figure 2.2 shows T_c and T_N with respect to the de Gennes factor, $(g_J - 1)^2 J(J+1)$ for pure RNi$_2$B$_2$C compounds (Bud'ko and Canfield (2006); Canfield et al. (1997)). This data shows that it is possible for the de Gennes factor to work as a scaling parameter for both T_c and T_N.

Figures 2.3(a) and (b) demonstrate the power of predictive theory: Abrikosov-Gorkov (AG) predictions of T_c suppression are shown and compared with experimental data for La$_{1-x}$R$_x$Al$_2$ and La$_{0.99}$R$_{0.01}$. The agreement with AG in La$_{1-x}$Gd$_x$Al$_2$ is striking. Fig. 2.3(c) shows a major victory of AG theory over BCS: AG theory predicts a universal specific heat jump with respect to T_c/T_{c0} (Skalski et al. (1964)). The experimental data bears this out, with considerably better agreement with AG theory than with BCS.
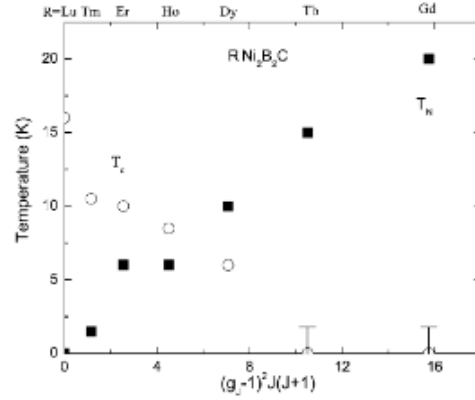
Figure 2.2: T_c and T_N vs. de Gennes factor for pure RNi$_2$B$_2$C.(Bud'ko and Canfield (2006))
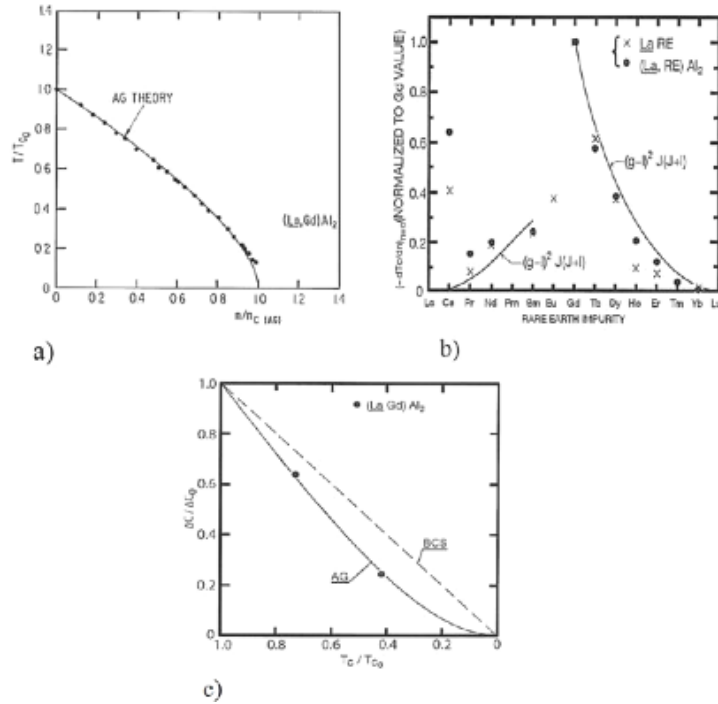
Figure 2.3: (a) $\frac{T}{T_{c0}}$ vs $\frac{n}{n_c}$. The solid line is from AG theory, the dots are experimental data from La$_{1-x}$Gd$_x$Al$_2$. (b) The solid line is the de Gennes factor (normalized to the value of Gd) compared with different rare earth impurities. (c) $\frac{\Delta C}{\Delta C_0}$ vs $\frac{T_c}{T_{c0}}$. The solid line is a numerical prediction from AG theory and the broken line is the theoretical curve from BCS theory. The dots are the experimental data for La$_{1-x}$Gd$_x$Al$_2$ and La$_{0.99}$R$_{0.01}$. (Maple et al. (2008))

2.2.2.1 Impurity Effects in Iron Arsenides

Because the FeAs superconductors are multiband systems with nontrivial, $S^{\pm}$ symmetry, Ω is nonzero. This means that nonmagnetic, isoelectronic impurities can, in fact, affect the transition temperature, since interband scattering is harmful to $S^{\pm}$ gapped superconductivity (see Eq. 2.21). However, the situation is still *more* complex here. The superconducting and SDW states are in competition, so consideration of the suppression of the SDW state is important as well. Since interband and *intra*band scattering both weaken the SDW state, T_c can be increased by disorder induced intraband scattering. When both interband and intraband scattering are present, the exact effect is not immediately obvious: if the combination of interband and intraband scattering is strong enough to suppress the SDW state more rapidly than the interband scattering suppresses the superconducting state on its own, then T_c will increase. However, if the interband scattering is too strong, then both the SDW and superconducting states will be suppressed. Since nonmagnetic impurities promote interband scattering, this is the relevant case here. As an aside, the observation that the superconducting state can be suppressed by the same impurities that suppress the SDW state corroborates the ARPES evidence for $S^{\pm}$ symmetry, as opposed to $S^{\ddagger}$, which is also allowed in fully gapped, multiband superconductors. (Senga and Kontani (2008); Kogan (2009); Vavilov and Chubukov (2011); Fernandes et al. (2012))

2.3   Maps for Superconductivity: Phase Diagrams

Many families of materials which display superconductivity require that some parameter be properly tuned to induce the state. Even in families where the parent compound is superconducting, there are often relatives which are not. Exploring the phase space diagrams produced by measuring the results of this tuning can give useful insight into what may be happening in these systems. This is essentially the basic motivation for all of the work discussed in this thesis. Here, I will discuss the general features of the generic phase diagrams of several classes of superconductors.

2.3.1 Heavy Fermion Materials

Heavy fermion systems are those where the low-temperature specific heat is much larger than the free electron model predicts – up to 1000 times as high (Coleman (2007)). This can be modeled by substituting a much heavier charge carrier mass for that of the electrons:

$$C_{P,el} = \frac{\pi^2}{2}\frac{k_B}{\epsilon_F}nk_BT \tag{2.29}$$

$$= \frac{\pi^2}{2}\frac{k_B}{\frac{\hbar^2 k_F^2}{2m_e}}nk_BT \tag{2.30}$$

$$= \pi^2\frac{m_e k_B^2}{\hbar^2 k_F^2}nT \tag{2.31}$$

$$m_e \rightarrow m^* \Rightarrow C_{P,hf} = \pi^2\frac{m^* k_B^2}{\hbar^2 k_F^2}nT. \tag{2.32}$$

Heavy fermion systems consist of f and conduction electrons, and their physics is dominated by two phenomena: the Kondo effect and the RKKY exchange. The Kondo effect hybridizes the f orbitals and the conduction bands, leading to the formation of a strongly renormalized Fermi liquid. The RKKY exchange governs the interaction between two f electrons via the conduction electrons, which leads to local magnetic order of the f electrons. Competition between these two effects results in a rich phase space for these systems which can be tuned by a number of parameters, including the application of mechanical pressure and chemical substitution (Doniach (1977)).

Figure 2.4 shows a generic phase diagram for heavy-fermion systems.[1] A detailed exploration of these systems and their behavior is beyond the scope of this work, but there are several features of note. For $\delta \sim 0$, the system goes through an antiferromagnetic (AFM) ordering as the temperature is dropped. For large δ, the system displays Fermi liquid behavior. In the intermediate region, the high temperature behavior is that of a non-Fermi liquid (Stewart (2001)). The interface between the AFM ordered and fermi liquid regimes is a $T = 0$ quantum phase transition. Some systems can be coaxed into a superconducting state, which forms around this phase transition (Flouquet et al. (2006)).

---

[1]http://www.toulouse.lncmi.cnrs.fr/spip.php?article134&lang=fr
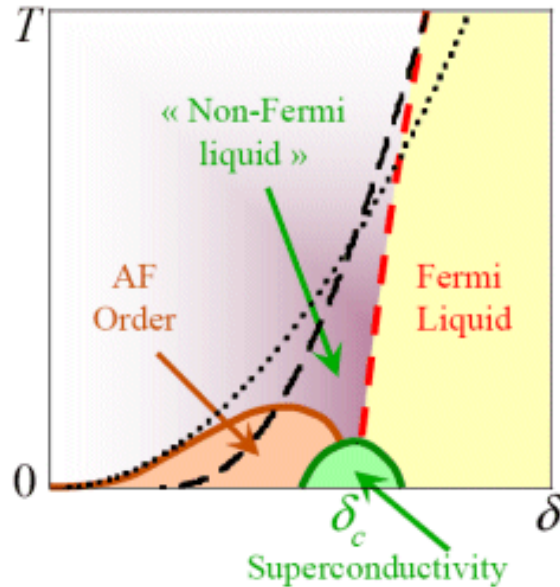
Figure 2.4: A generic phase diagram for heavy fermion systems. δ may be any of several tuning parameters.

2.3.2 Copper Oxides

The copper oxides are perhaps the best known family of nonconventional superconductors. The only materials known to superconduct above the liquification temperature of nitrogen – a cheap, readily available cryogen – are members of this family. This family has a rich phase diagram, displaying many phases as electron and hole substitutions are made (Fig. 2.5). As with heavy fermion materials, a detailed exploration of the behavior of these systems is beyond the scope of this thesis, but there are a few features to point out. The parent materials are insulators at high temperature and go into an AFM state as the temperature is dropped. As electrons are added or subtracted through chemical changes (either substitutions or deficiencies), several other phases can be reached. Superconductivity is observed as one of these phases on both the hole and electron doped sides of the phase space, around the $T = 0$ quantum phase transitions associated with the suppression of the AFM state.
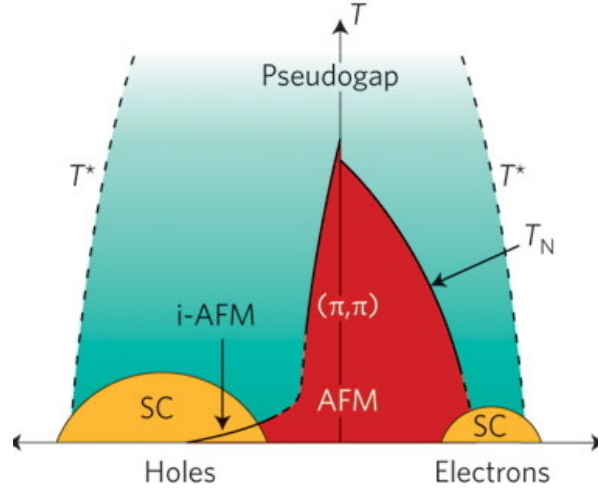
Figure 2.5: Generic electronic phase diagram for layered copper oxide materials (Basov and Chubukov (2011)).

2.3.3   Pnictides

The newest family of nonconventional superconductors are the pnictides, of which $BaFe_2As_2$ is a member. The original subfamily was the RFeAsO (1111) group. Although the parent compounds do not exhibit superconductivity at ambient pressure, they do display low temperature AFM ordering. They also can be induced to superconduct under pressure. Kamihara et al. (2008) showed that superconductivity could be induced through chemical substitution as well.

Figure 2.6 shows two possible generic phase diagrams for the 1111 system. With R=Ce, F substitution gives a smooth, second order phase transition from the AFM parent phase to the superconducting one. With R=La, the same substitution gives an abrupt, first order transition from spin density wave to superconductivity with the same substitution. Nevertheless, both cases show emergence of superconductivity from a magnetically ordered state with chemical substitution.

Figure 2.7 shows the basic phase diagram for $Ba(Fe_{1-x}Co_x)_2As_2$. Here, we see a feature familiar from the discussion of cuprates: emergence of superconductivity around the $T = 0$ point where the AFM state is completely suppressed. Nandi et al. (2010) and Kreyssig et al. (2010) found evidence that there is a so called 'back bend' in the structural and AFM transitions below the superconducting dome. This provides further evidence for the supposition that the
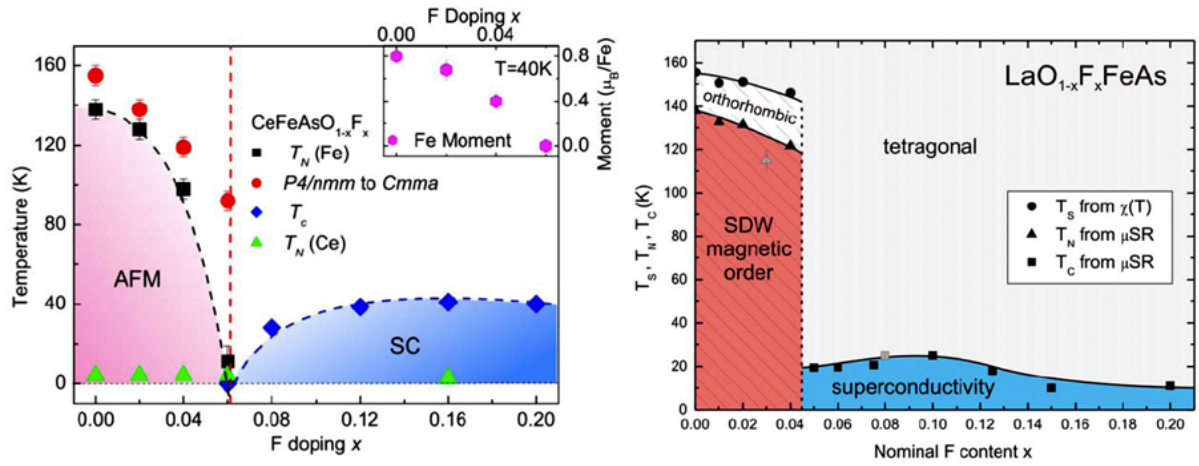
Figure 2.6: (Left) Substitution dependent phase diagram for $CeO_{1-x}F_xFeAs$ (Zhao et al. (2008)). (Right) Phase diagram of fluorine substituted $LaO_{1-x}F_xFeAs$ (Luetkens et al. (2009)).
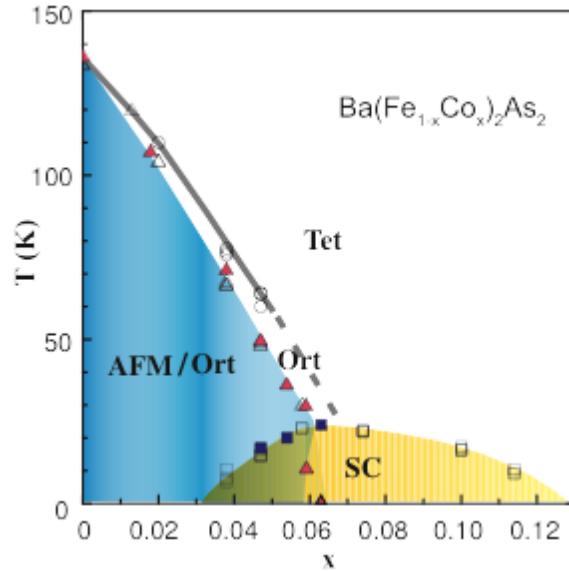
Figure 2.7: Co substitution-dependent phase diagram for $BaFe_2As_2$(Fernandes et al. (2010)).
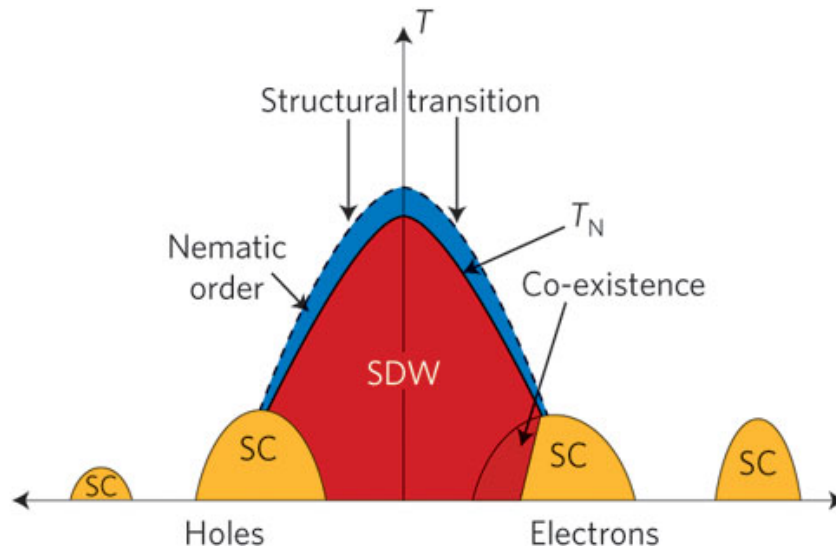
Figure 2.8: Generic electronic phase diagram for pnictide materials (Basov and Chubukov (2011)).

superconducting dome is formed around a $T = 0$ phase transition.

Figure 2.8 shows a generic electronic phase diagram for the pnictide materials. The parallel with the cuprate materials is even more evident here: we see suppression of the spin density wave AFM order and emergence of superconductivity on both the electron and hole doped sides of the phase space, and both of these superconducting domes appear partially underneath the AFM regions. In the case illustrated in Fig. 2.8, the holes were introduced by K substitution for Ba; unfortunately, as will be discussed in Chapters 6 and 7, similar hole doping does not occur for substitution of Mn or Cr for Fe.

CHAPTER 3.   Experimental methods

3.1   Crystal growth

Single crystals are essential for many scientific measurements. Single crystals, by definition, have no grain boundaries, so secondary impurity phases are usually less common. They are also often under less strain than their polycrystalline equivalents. In addition, certain high precision measurements are impossible without single crystal samples. One example is Angle Resolved Photoemission Spectroscopy (ARPES), which can directly measure the Fermi surface and superconducting gap size and symmetry, but which requires a cleaved single crystal surface. Single crystals also have a well-defined orientation, which is important for both x-ray and neutron diffraction measurements. Direct measurement of anisotropic properties also requires single crystalline samples.

Several classes of techniques are used to grow single crystalline samples: melt growth, vapor growth and solution growth. Melt growth and vapor growth both have limitations which make them less suitable for use in synthesizing members of $BaTM_2As_2$ (TM=Fe and surrounding transition metals). Melt growth techniques require congruent or near-congruent melting temperatures of the components, whereas vapor transport methods require that the components be put in a volatile state and may require a transport agent (if self transport is not possible).

3.1.1   High temperature solution growth

A subset of the third category, high temperature solution growth, is a widely used and recognized technique for discovering and growing single crystals of complex materials. (Fisk and Remeika (1989); Canfield and Fisk (1992); Canfield and Fisher (2001)) It is viable for

both congruently and incongruently melting materials and may be used to control high vapor pressures of constituent components. All samples presented in this thesis were grown using a high temperature solution growth method.

High temperature solution growth requires that several factors be considered: solvent, initial concentrations of components, maximum achievable temperature, cooling rate and decanting temperature. The solvent must allow adequate solubility of the other components below the maximum achievable temperature, which necessitates a melting temperature well below the maximum achievable by the experimental setup. This solvent is sometimes called a "flux". There are two possible flux classifications: self flux and non-self flux. When using a self flux, an excess of one or more component of the crystal to be grown is used as the solvent. In a non-self flux growth, an extra element or compound is added to act as the solvent for the crystal constituents.

A self flux method is often preferable, as it does not introduce additional elements into the melt and therefore cannot introduce other elements into the crystal and is less likely to introduce phases other than the desired one. However, it is not always possible or practical to use a self flux method. In many cases, there is no constituent or combination of constituents of the desired material that has a low enough melting temperature to be practical as a flux, either because of limitations of the furnace or the ampoules. In other cases, the vapor pressure may be too high, which may lead to a loss of stoichiometry or even explosion. In these cases, an extra element or compound with a lower melting temperature and high solubility of the crystal constituents may often be used. This flux should also have a low vapor pressure and compatibility with the crucibles. Al, Ga, In, Sn, Sb, Bi and Pb are frequent choices.

In either case, the constituent elements are dissolved in the flux at high temperature and form a uniform solution. As the temperature is decreased, the solubility of the target compound decreases and at some intermediate temperature it starts to precipitate out of the solution, ideally in single crystal form. The crystal size depends on the number of nucleation sites, which itself often depends on the cooling rate. In principle, slower cooling should result in larger crystals. Slow cooling can also reduce the internal strain in the crystals. Once the crystals have been grown, the remaining liquid can be decanted using a centrifuge. The decanting

temperature must be chosen carefully: it must be high enough that no impurity phases can exist and the flux is still liquid, but low enough that the crystal has as large a temperature window as possible to grow in. Any remaining flux left on the surface can be removed by an appropriate chemical or mechanical polishing process.

3.1.2 Growth of single crystals of $BaFe_2As_2$ and $Ba(Fe_{1-x}TM_x)_2As_2$ (TM=Cr, Mn, Co, Cr/Co, Mn/Co, Ni, Cu, Ru, Rh, Pd, Ir)

3.1.2.1 $BaFe_2As_2$

Single crystals of the parent compound, $BaFe_2As_2$, may be grown using either a self flux method or a by using Sn as the flux. However, for $BaFe_2As_2$, Sn enters the structure. (Ni et al. (2008b))

The self flux used in this case is FeAs (see Fig. 3.1). FeAs is produced by a solid state reaction method. Commercially produced Fe powder (Sigma-Aldrich or Alfa-Aesar, 99.9% metals basis) was mixed with finely ground As (Alfa-Aesar, 99.9999% metals basis) in a ratio of 1.05:1. The purpose of the excess Fe in this mixture was to ensure that all the As would be reacted as it is both toxic and volatile. Two methods were used to ensure homogeneous mixture and reaction. The first was to mix the two powders in an agate mortar and pestle, then press the mixture into pellets of approximately 5 g each. Typically, between 20 and 100 g was made at one time. These pellets were then placed in a SiO_2 ampoule, evacuated to at least 30 mTorr and backfilled with 1/6 partial atmosphere of Ar. The ampoule was heated to react the two powders. In the second method, the two powders were sealed in a SiO_2 ampoule with a small cylinder of SiO_2 attached along the length of the inner surface. The ampoule was placed in a rotating furnace and heated. The rotation of the ampoule and motion of the SiO_2 cylinder within mixed the powder as it was being reacted, removing the requirement that it be premixed or pressed into a pellet. Both methods produce high quality binary precursors; choosing one over the other was simply a matter of preference and convenience. In both cases, the ampoule was heated to 580°C and held for 15 hours, then heated to 900°C and held for an additional 15 hours. In both cases, the mixture was prepared under a dry nitrogen atmosphere
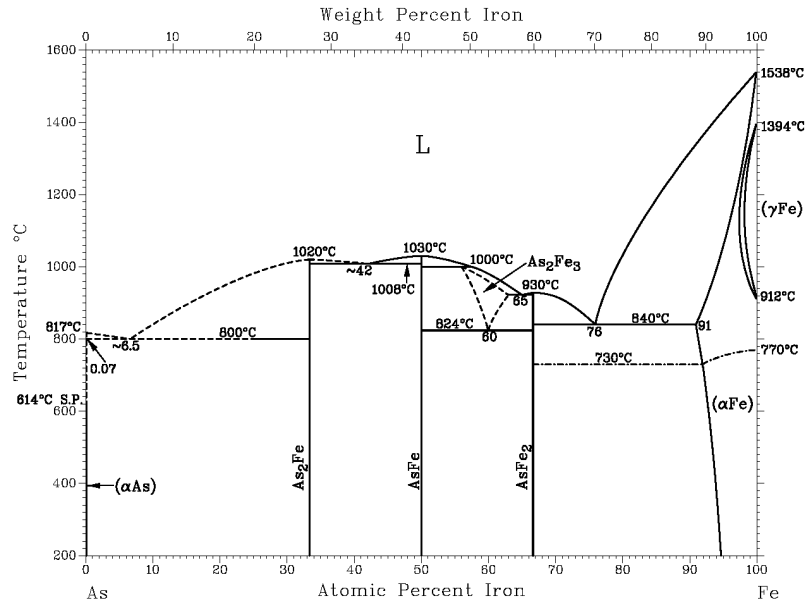
Figure 3.1: Phase diagram of the Fe-As binary system. (Copyright ©1996 ASM International [ASM (1996)])

in a glove box because of the toxicity of As.

$BaFe_2As_2$ crystals grown from self flux were synthesized by combining Ba chunks (Sigma-Aldrich, $\geq 99\%$ metals basis) with FeAs powder in a molar ratio of one to four ($BaFe_4As_4$; see Fig. 3.3). Because of the extreme air sensitivity of Ba and the toxicity of As, this was done in the same dry nitrogen glove box as for the binary preparation. This mixture was layered within an Al_2O_3 "growth" crucible that was paired with an identical "catch" crucible filled with quartz wool. Both were then sealed in a SiO_2 ampoule under 1/6 partial atmosphere of Ar. The extreme air sensitivity of Ba meant that the tubes had to be sealed without exposing the contents to the outside. A detachable valve assembly was placed into the glove box so that the tube could be attached to the valve inside the inert atmosphere. A second, smaller tube was placed inside the main one in order to facilitate sealing the tube while under soft vacuum. These ampoules were placed in a "box" furnace at 300°C and heated to a temperature of 1180°C over a period of 18 hours, with a one hour rest at 600°C to ensure that any possible remaining As is reacted before going to even higher temperatures. The mixture was then held at 1180° for 8-12 hours to ensure that the melt had a chance to homogenize, then it was cooled over a period of

Figure 3.2: Left: hydraulic press used for making TMAs powder pellets. Right: horizontal furnaces used for solid state synthesis of TMAs. The foreground furnace has the rotating sample attachment inserted.

several days to $1000°$ and decanted by spinning in a centrifuge. The quartz wool in the "catch" crucible strains the solid crystals from the excess liquid, making them easier to extract. This apparatus, including a doubly-sealed tube and valve assembly, can be seen in Fig. 3.4.

3.1.2.2 TM substitution

When substituting other transition metals (TM) onto the Fe site in $BaFe_2As_2$, some of the FeAs is replaced by other TMAs binaries. These binaries are produced using a similar solid state reaction as is used for FeAs: TM and As powders are combined through either the pellet or rotating furnace method described above. Most of these binaries are well behaved and fully react without issue, but several caused problems, requiring changes in the temperature profile used for the solid state reaction, either the maximum temperature or the length of time held at that temperature. CrAs was particularly problematic: when we first attempted to synthesize it, the growth tube exploded. Successful synthesis required that the mixture be reground and reacted several times at low temperature before all of the powder was fully reacted. Phase diagrams of these TMAs binary systems can be seen in Figs. 3.5-3.7. It should be noted that in some cases we were not making a 1:1 TMAs binary, but instead a combination of several TM_xAs_{2-x} binaries.

Once TMAs binaries were created, growth of TM substituted crystals proceeded in a manner similar to the parent compound: Ba chunks and TMAs powders were combined in an Al_2O_3 crucible. In order to encourage homogeneous substitution, the TMAs powders were mixed
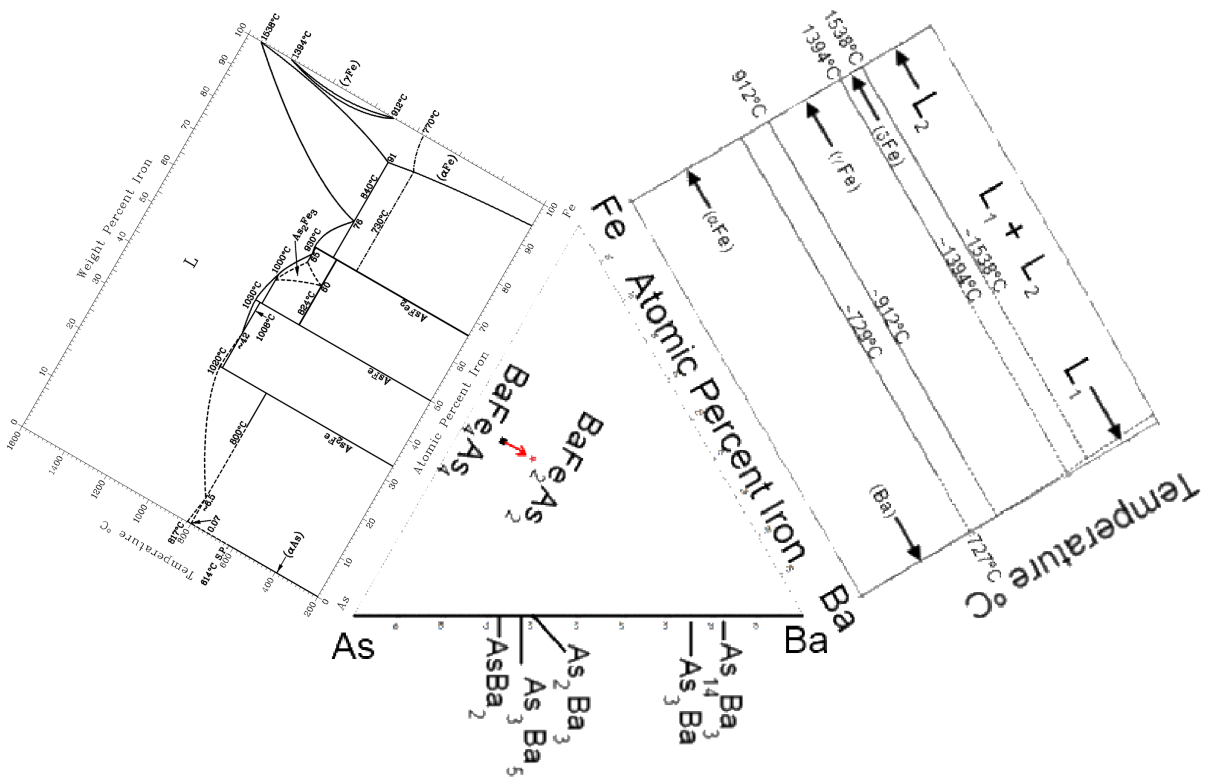
Figure 3.3: Schematic ternary phase diagram of the Ba-Fe-As system, showing starting and final compositions when synthesizing BaFe$_2$As$_2$. (Copyright ©1996 ASM International [ASM (1996)])

Figure 3.4: Top left: dry nitrogen glove box used for air work with air sensitive elements. Top right: detachable valve unit for the glass bench which can be taken into the dry glove box. Middle left: doubly-sealed SiO_2 ampoule representative of those used for synthesis of crystals containing highly volatile, toxic or air sensitive constituents. Middle Right: double-tube and valve assembly together. Bottom left: "box" furnaces used for high temperature sample synthesis. The furnaces are inside a vented metal enclosure to guard against the possibility of explosive accidents. Bottom right: centrifuge used for decanting excess liquid from the growth.
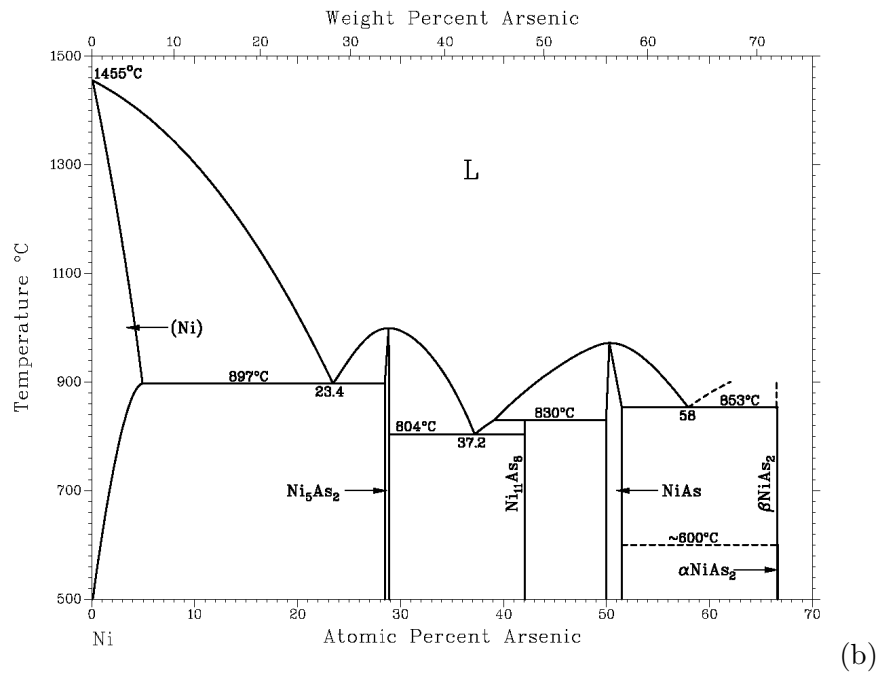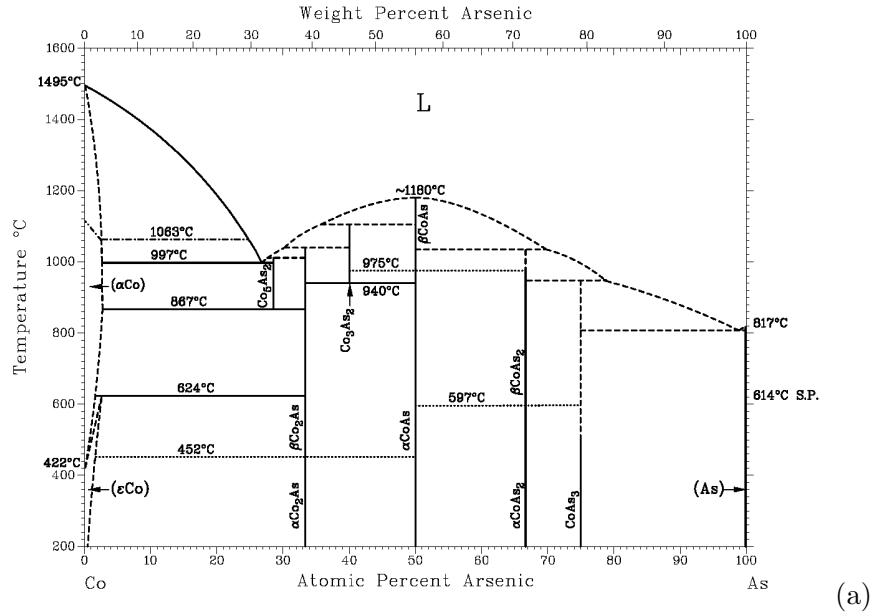
Figure 3.5: Phase diagrams of the Co-As and Ni-As binary systems. (Copyright ©1996 ASM International [ASM (1996)])
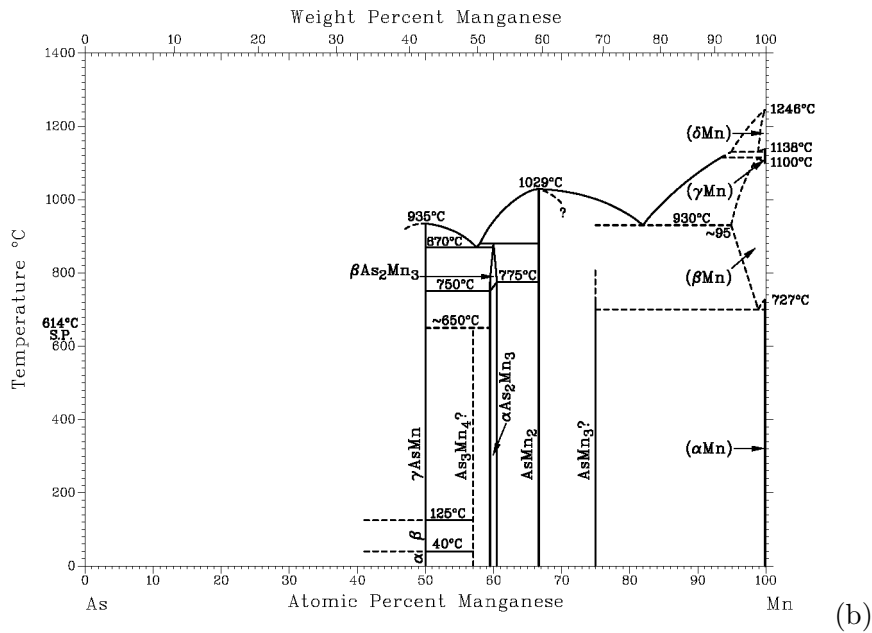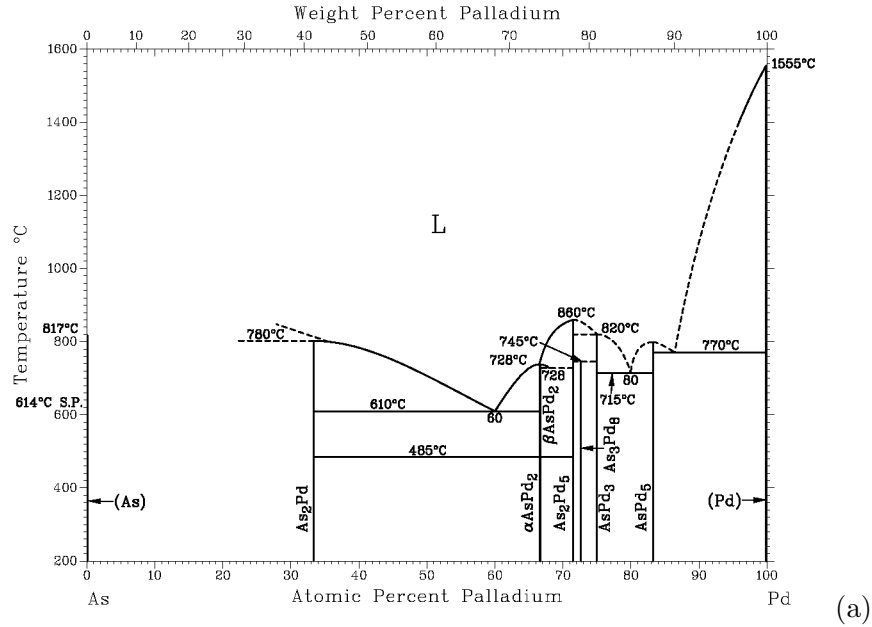
Figure 3.6: Phase diagrams of the Pd-As and Mn-As binary systems. (Copyright ©1996 ASM International [ASM (1996)])
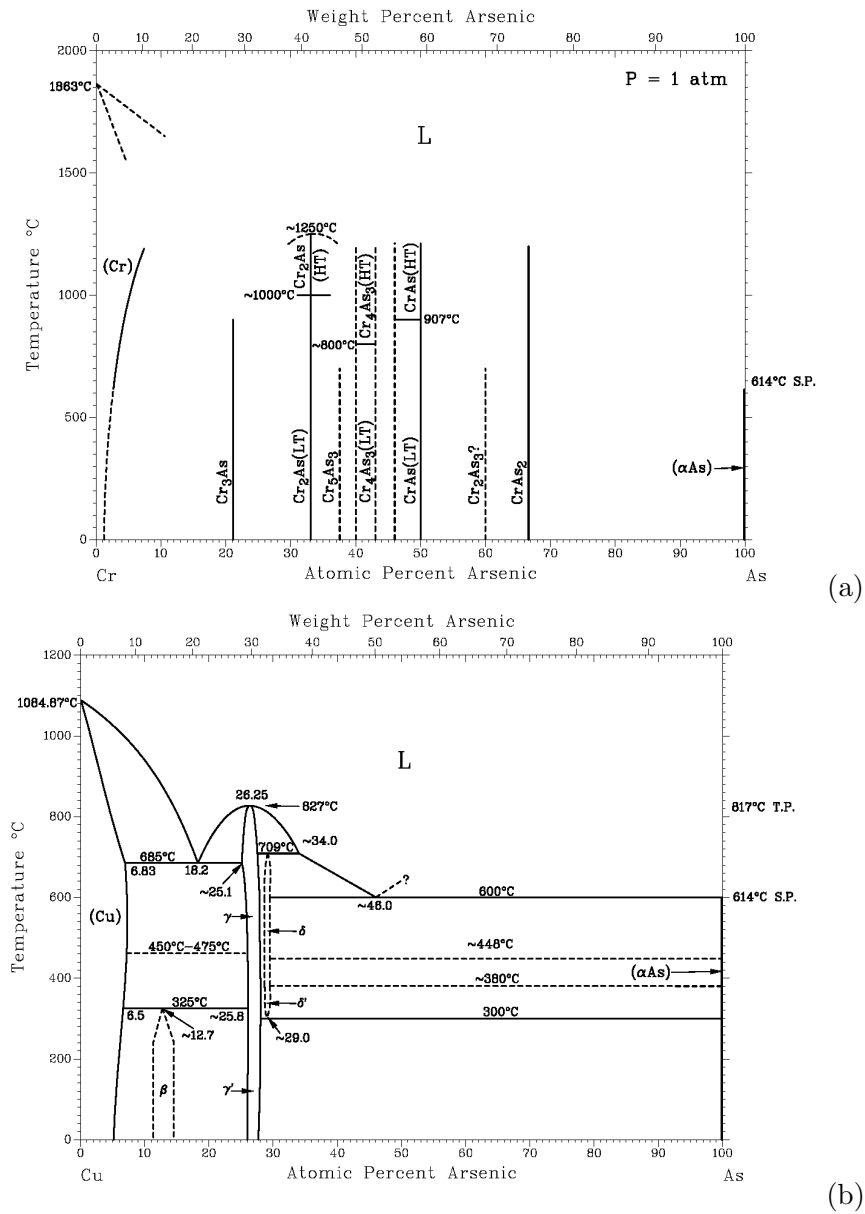
Figure 3.7: Phase diagrams of the Cr-As and Cu-As binary systems. (Copyright ©1996 ASM International [ASM (1996)])

together in an agate mortar and pestle, once again in a dry nitrogen glove box. The crucible was then sealed in a SiO_2 ampoule along with a corresponding 'catch' crucible. Depending on the particular substitution and substitution level, the decanting temperature sometimes had to be raised, but the basic temperature profile remained unchanged.

The nominal TM substitution fraction was not the same as the actual fraction obtained in the crystals. The ratio of nominal to real substitution fraction varied depending on both the substitution being made and the substitution fraction. (Ni et al. (2008b, 2009, 2010)) Details of the technique used for quantifying the level are given below.

3.2   Characterization methods

3.2.1   Powder x-ray diffraction

Powder x-ray diffraction (XRD) measurements were performed on ground samples of the crystals at room temperature. This was done using a Rigaku Miniflex diffractometer with Cu K_α radiation. We performed this measurement for two reasons. The first was to attempt to detect any impurity phases or inhomogeneity that might have been present in the crystals. As a general rule, the phase purity and homogeneity of these samples was very good, with sharp peaks indicating little spread in the crystallographic lattice parameters and no significant secondary phase detectable. The exception was in Mn substitution, which will be discussed later.

The second reason for performing powder XRD was to measure the variation of the lattice parameters with substitution level. In order to make quantitative statements about the lattice parameters, the ground crystals were combined with Si powder, with lattice parameter $a = 5.4301$ Å. The Si acted as an internal standard reference. *Rietica*[1] software was used to fit the lattice parameters. First, the pattern was fitted to the Si standard peaks in order to adjust for any zero offset in our apparatus. The lattice parameters of the growth could then be fitted by measuring the shifts in the peaks from those of the parent compound. An example xray pattern along with the fit can be seen in Fig. 3.8. Samples prepared in this manner do not

---

[1] http://www.rietica.org/
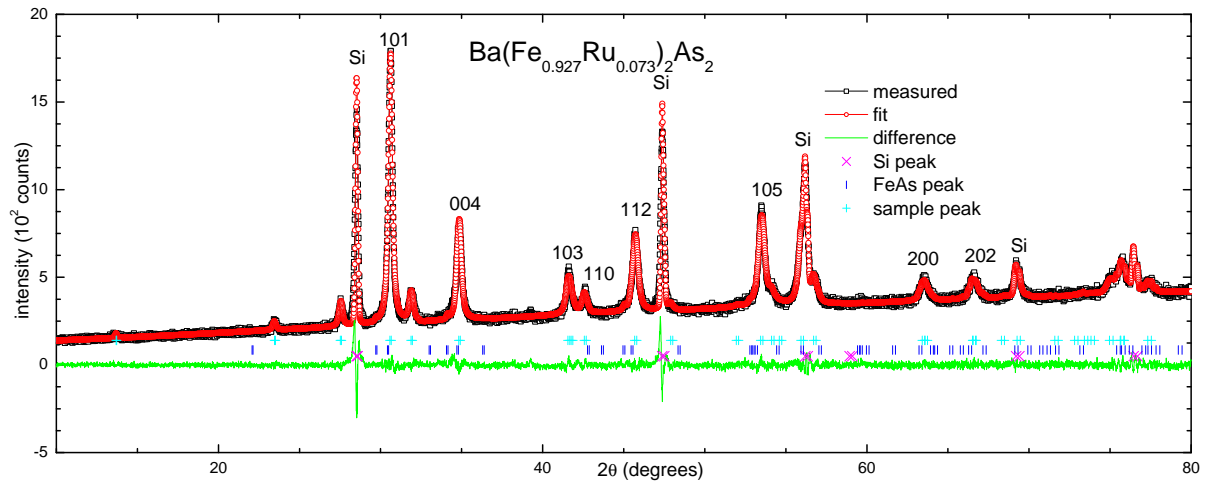
Figure 3.8: Clean powder x-ray pattern from $Ba(Fe_{0.927}Ru_{0.073})_2As_2$. Also shown are the Si peaks used as a standard for correction and the fit found by Rietica.

show significantly different lattice parameters from those measured with single crystal x-ray diffraction (Rullier-Albenque et al. (2010)), suggesting that grinding them into powder does not significantly distort the structure.

3.2.2 Wavelength dispersive spectroscopy

As mentioned previously, the nominal and real TM substitution fractions were not generally the same. In addition, although real TM substitution levels were generally reproducible given the same nominal level, there was some variation between nominally identical batches. In order to determine the actual concentration of TM in the crystals, we used wavelength dispersive spectroscopy (WDS). This was performed in the electron probe microanalyzer of a JEOL JXA-8200 *SuperProbe* electron microprobe[2]. For quantitative measurement of chemical composition, WDS is superior to the more common energy dispersive spectroscopy (EDS) method of spectrographic analysis. This is because while EDS attempts to collect xrays produced from all elements at the same time through the same detector using a wide-band detector, WDS selects a narrow energy band and measures the locations of the individual peaks expected from the element(s) the diffractometer has been tuned to. Under ideal circumstances, a WDS mi-

---

[2]http://www.jeolusa.com/PRODUCTS/ElectronOptics/SurfaceAnalysisSA/JXA8230/tabid/223/Default.aspx

croprobe will have multiple diffractometers, each set to only look for peaks from a particular element (ours has five). This allows the operator to eliminate nearby peak overlap as a source of error in the measurement. The resolution in WDS spectroscopy is between 2 and 15 eV, as compared to a typical EDS resolution of 70 to 180 eV. (Goldstein et al. (2003)) The primary disadvantages of WDS over EDS are that the sample must be able to withstand higher electron beam energy, the cost of the apparatus and operator, the relative complexity of making quali- tative measurements (eg. "What elements are in this mineral deposit?" or "Did this sample get contaminated by oxygen?"), and the time required for each measurement. Since intermetallic samples are generally robust, the equipment is already in place here (negating most of the cost problem), and we normally know what elements went into our samples, only the time required is a concern. Because knowing the composition of our samples to as great a degree of accuracy as possible is paramount and we are usually not in a hurry, the tradeoff between time and accuracy is easy to justify.

In WDS, an electron beam with sufficient energy is incident on a flat sample surface. These electrons interact with the atoms in the sample near the surface. These atoms are excited and emit x-rays. The x-ray wavelengths produced are unique to each element. By measuring the wavelength and relative intensity of these x-rays, we were able to determine the relative concentrations of elements within the samples.

Because WDS requires flat surfaces normal to the electron beam, it is essential to make sure that the samples are properly prepared. Fortunately, this family of compounds make such preparation relatively simple: these crystals may be split and exfoliated by inserting a razor blade between layers of the crystal. By doing this, we were able to produce flat samples with two parallel surfaces which were not previously exposed to atmosphere (helping to prevent the presence of surface impurities). By attaching one of these surfaces to a piece of conductive Cu tape attached to a metal microprobe mounting post, the sample was made to have a flat surface normal to the electron beam. By splitting several layers of the sample out and measuring surfaces from each, we were able to determine that the stoichiometry was (nearly) uniform across the depth of the samples.

3.2.3 Resistance

Temperature dependent resistance measurements were performed in either a Quantum Design (QD) Magnetic Properties Measurement System[3] (MPMS) using a Linear Research/LakeShore LR-700 AC resistance bridge[4] ($f = 16Hz$, $I = 1mA$) or in a QD Physical Properties Measurement System[5] (PPMS) using either the AC transport option ($f = 16Hz$, $I = 1mA$) or the DC resistivity option ($I = 1mA$). In general, the temperature range used was 2 K to 300 K, but some measurements were made up to 375 K.

As with WDS, the macroscopic layered structure of the samples made preparing resistance samples relatively simple. After cutting a piece of the crystal of appropriate length and width, a razor blade was used to split two adjacent layers and expose the flat surface between them. Because this is an internal surface, it is clean and flat and generally has no flux on it.

With the surface thus exposed, Pt wires were attached to the bar using Epotex H20E silver epoxy in a standard four-probe configuration with the current flow in the ab plane (perpendicular to the c axis). These were cured at either 120°C for 30 minutes or 175°C for 10 minutes. I observed no difference between samples prepared using the two temperatures. Typical contact resistance was between 1 Ω and 3 Ω.

Unfortunately, the same layered structure that allows for easy preparation of the surface for contact attachment also makes it difficult to get resistivity rather than simply resistance. When a thin sample is further cut, it has a tendency to further exfoliate or crack, leading to non-trivial current paths and poorly defined effective lengths and cross sectional areas (Ni et al. (2008b)). Therefore, normalized resistance, $R(T)/R_{300K}$, is generally used in this thesis.

3.2.4 Magnetization

Magnetization measurements were made using either a 5.5 T or 7 T QD-MPMS. When measuring magnetic properties in the superconducting state, a demagnetization sequence was used before any low field measurement. This sequence was run at a temperature well above the superconducting transition temperature. The field was ramped up to maximum, then to

---

[3]http://www.qdusa.com/products/mpms.html
[4]http://www.lakeshore.com/ObsoleteAndResearchDocs/LR700_V1_3_%20Manual.pdf
[5]http://www.qdusa.com/products/ppms.html

the maximum in the opposite direction. The field was roughly halved at each subsequent step and the positive and negative direction was repeated. 10-12 of these steps were made from the maximum H of the machine being used (either 55 kOe or 70 kOe) down to ~ 50 Oe, then finally to zero. Zero field cooled (ZFC) and field cooled (FC) magnetization data were then taken at 50 Oe from below the supeconducting transition temperature (T_c) to several Kelvins above so that an estimate of the superconducting volume fraction could be made. The fraction of the sample which is superconducting is determined by comparing the magnetic signal from the sample being measured to that of an ideal, fully superconducting sample displaying perfect diamagnetism (ignoring the geometric demagnetization factor). To get the fraction of the sample which is superconducting, we need to know three things: the volume of the sample, the applied field and the measured moment. Since it is somewhat difficult to measure the volume of an irregularly shaped sample with any accuracy, we instead measure its mass and calculate its density from the molar masses of its constituent elements and its unit cell parameters. The susceptibility (M/H) of a perfect spherical diamagnet is $-1/4\pi$, so we multiply by 4π in order to get -1.0 as 100% superconducting (-1 instead of +1 by convention). Thus, the final formula used for calculating superconducting fraction (in CGS-Gaussian units) is

$$\text{SV} = 4\pi \frac{|\mathbf{M}|}{|\mathbf{H}|} \cdot \frac{\rho}{m} \tag{3.1}$$

Since low field magnetization measures the bulk properties of a sample, we generally expect to see $T_{c,\text{onset}}$ as determined by $M(T)$ at approximately the same temperature as $T_{c,\text{offset}}$ as determined by resistance. The relative insensitivity of low field magnetization to filamentary superconductivity means that it is, is in some ways, a better measure of bulk T_c than resistance. This is especially important in the AFe$_2$As$_2$ (A=Ca, Sr, Ba) system, as there are indications that it is quite sensitive to strain under certain conditions (Saha et al. (2009)). On the other hand, this same insensitivity means that it is more difficult to use the superconducting transition to determine whether a sample is homogeneous through magnetization than it is through resistance: a sample which has regions of differing substitution fraction will show a "step" in the superconducting transition as measured by resistance, but magnetization will normally not see the superconducting state until it is fully manifested. The difference in sensitivity of

the magnetic measurement to bulk vs filamentary superconductivity is important for the work discussed in Chapter 8.

Samples were mounted either with $H||c$ or with $H \perp c$. In the case of $H \perp c$, the samples were mounted between two plastic straws. The inner straw is split down one side to allow it to fit within the outer straw. Small holes were punctured through both straws around the sample to make it less likely that it would move, and the end was sealed with teflon tape as an added security against sample loss. In the case of $H||c$, a similar techique was used. In this case, the inner straw was cut in half and both halves were folded in on themselves to give added surface area for contact with the sample. The sample was stabilized between the two half straws and the end was once again sealed with teflon tape.

3.2.5 Signatures of structural, antiferromagnetic and superconducting phase transitions in transport and magnetic measurements

Structural, antiferromagnetic and superconducting phase transitions manifest with characteristic signatures in both resistance and magnetization measurements. Although the situation in this system is somewhat more complex, these typical signatures are shown in Fig. 3.9 for metallic systems. A loss of spin disorder scattering manifests as a decrease in resistance, and the long range ordering of the antiferromagnetic state shows as a drop in the temperature dependent susceptibility. The antiferromagnetic transition temperature can be determined either from $d\rho/dT$ or from $d\chi/dT$: T_N is at the maximum in $d\chi/dT$ and $d\rho/dT$. (Chu et al. (2009); Lester et al. (2009))

A structural phase transition – such as a charge density wave (CDW) transition – can lead to a decrease in the density of states at the Fermi level, $D(E_F)$. In the case of a charge density wave, this may partially gap the Fermi surface, which will manifest as an abrupt upturn in resistivity because of the decrease in conduction electrons and a decrease in the susceptibility caused by the decrease in $D(E_F)$. Figure 3.9(b) shows the resistive and magnetic signatures of the structural phase transition. The structural phase transition temperature, T_S, can be inferred from the minimum in $d\rho/dT$ and the maximum in $d\chi/dT$. (Ni et al. (2008b))

Because there are both structural and magnetic transitions, the situation is more complex
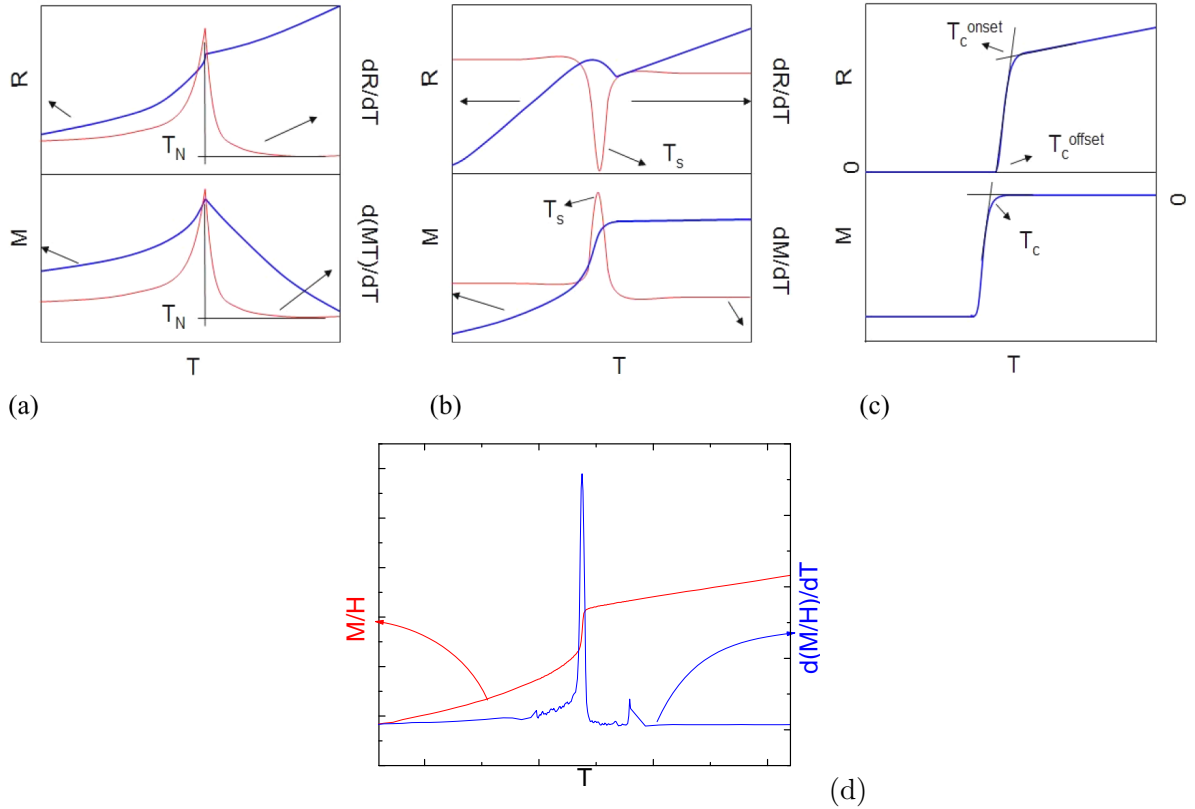
Figure 3.9: Top: Characteristic signatures in resistivity and magnetization near the transition temperatures of metallic samples with (a) local moment antiferromagnetic, (b) structural (CDW), and (c) superconducting phase transitions. Bottom: M/H signature of the structural and magnetic transition in $BaFe_2As_2$. The anomaly in the derivative a few Kelvins above the transition is an artifact of changing the temperature spacing when performing the measurement.

in this system. For the parent compound without any dopant, the M/H transition signature appears as in Fig. 3.9(d).

A compound which undergoes a superconducting phase transition will display zero electrical resistance and large (ideally perfect) diamagnetism. Figure 3.9(c) shows these features and demonstrates the criteria used to determine $T_{c,\text{onset}}$ and $T_{c,\text{offset}}$ in this thesis.

CHAPTER 4.   Motivation and Previous Work

Fe based superconductivity was first discovered in LaFePO (Kamihara et al. (2006)) with $T_c \approx 5$ K. The discovery, two years later, of superconductivity in LaFeAs($O_{1-x}F_x$) (Kamihara et al. (2008)) with $T_c \approx 26$ K led to extensive interest in this family of FeAs based compounds. An applied pressure of 12 GPa induced superconductivity in LaFeAsO at 21 K (Okada et al. (2008)) and as high as 43 K in LaFeAs($O_{0.89}F_{0.11}$) under a pressure of 4 GPa (Takahashi et al. (2008)). Other rare earth metals have produced even more striking results: T_c has risen as high as 56 K for F-substituted RFeAsO (R=Ce-Gd, Zhi-An et al. (2008)). Superconductivity was also observed in Co substituted RFeAsO (Sefat et al. (2008a)).

A few months later, Rotter et al. (2008a) discovered that ($Ba_{1-x}K_x$)Fe_2As_2 has T_c as high as 37 K. Over the past several years, a large amount of work has been done on members of this system and its relatives. In this Chapter, I will review some of the salient background that motivated my thesis work.

4.1   BaFe$_2$As$_2$

The parent compound of this family is interesting on its own. At room temperature, it is a poor metal ($\rho_{300K} \approx 10^{-4}\Omega \cdot cm$) with no ordered moment (paramagnetic) (Colombier et al. (2009); Kim et al. (2011c)), and is in the ThCr$_2$Si$_2$-type tetragonal $I4/mmm$ crystal structure (Pfisterer and Nagorsen (1980)). At 134 K, it undergoes a magnetic phase transition into an antiferromagnetic state, as well as a (nearly) simultaneous (Kim et al. (2011a)) structural transition into the orthorhombic $Fmmm$ crystal structure (Rotter et al. (2008b)). However, it does not show any sign of superconductivity down to the lowest achievable temperatures (Rotter et al. (2008b); Ni et al. (2008b)). Figure 4.1 shows typical temperature dependent

normalized resistance $(R(T)/R_{300\,K})$ and magnetization (M/H) data. Both data sets clearly show signatures of the coupled, nearly simultaneous phase transitions.
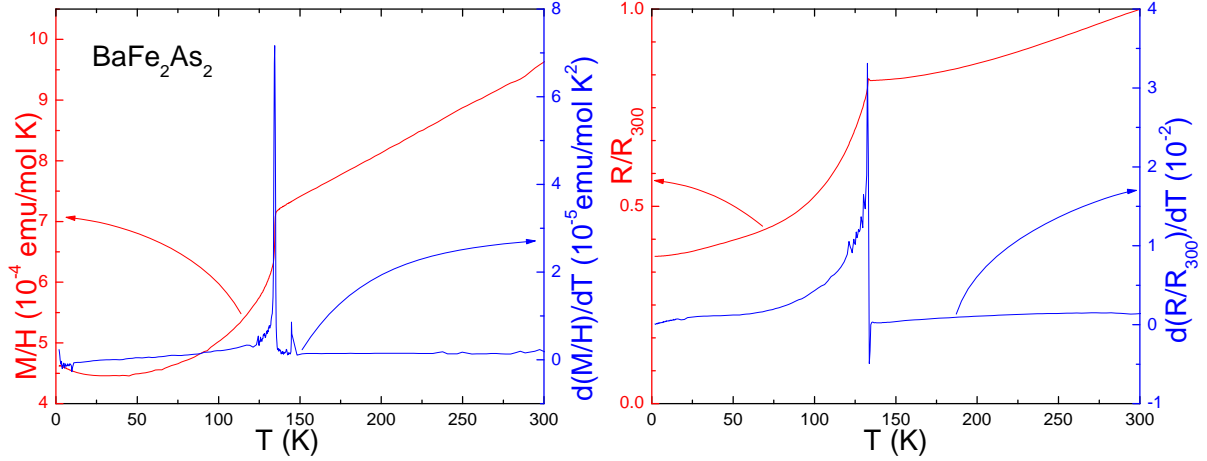
Figure 4.1: $M/H\,(T)$ (left) and $R(T)/R_{300}$ (right) for $BaFe_2As_2$. The feature seen just above the transition in the derivative of M/H is an artifact of a change in temperature step size ΔT. In both plots, the red line is the measured data and the blue line is the derivative. This data was taken in our lab on crystals grown in-house.

4.1.1 $BaFe_2As_2$ Under Pressure

Based on the behavior of LaFeAsO under pressure as reported by Okada et al. (2008), pressure was applied to $BaFe_2As_2$. Its behavior changed dramatically: with increasing pressure, the structural and magnetic transition temperatures are suppressed from their ambient pressure values until they finally vanish at a pressure of approximately 40 kBar (a value that varies with the degree of non-hydrostaticity of the apparatus or medium being used). There is also a clear low temperature superconducting state, which begins to manifest at an applied pressure of about 15 kBar and is fully formed (zero resistance) by 40 kBar. Sadly, although the maximum T_c achievable through the application of pressure is rather high ($\sim$33 K at $\sim$50 kBar), the transition into this state is not very clean: the transition width is very wide. Just above the minimum pressure required for full onset of supercondtivity, $T_{c,\text{onset}} - T_{c,\text{offset}} \approx 19$ K. The transiiton width is narrow only very near the optimal applied pressure (Colombier et al. (2009)). This large transition width is thought to be associated with non-hydrostatic conditions inherent

to these high pressures, coupled to the FeAs based materials' strain sensitivity. Exceptionally extreme examples of this can be found in the $CaFe_2As_2$ materials (Yu et al. (2009); Torikachvili et al. (2009); Canfield and Bud'ko (2010)).
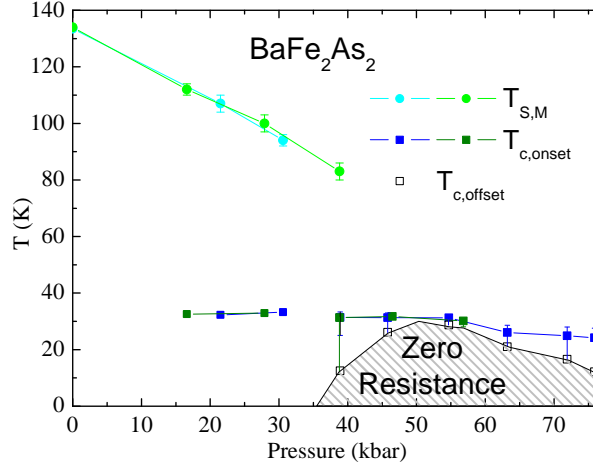
Figure 4.2: Pressure dependent phase diagram for $BaFe_2As_2$ (Colombier et al. (2009)).

4.2 $(Ba_{1-x}K_x)Fe_2As_2$

The first chemical changes in $BaFe_2As_2$ which produced superconductivity were alkali metal substitutions on the Ba site, with K the primary successful example. Rotter et al. (2008a) synthesized polycrystalline samples of $(Ba_{1-x}K_x)Fe_2As_2$ with x=0.3 and 0.4, and found that a nominal substitution of x=0.4 suppressed the structural and magnetic transitions to 0 K and induced superconductivity with $T_c \sim 37$ K. This high T_c means that it may be useful for industrial applications. Ni et al. (2008a) describe synthesis of single crystalline, K-substituted $BaFe_2As_2$. Here, Sn was used as a solvent rather than FeAs (see Chapter 3) because K boils at 1033 K, which is below the melting temperature of FeAs. Unfortunately, the K substitution was found to be nonuniform when a Sn flux is used, which makes the transition quite wide. Luo et al. (2008) were able to synthesize single crystals of $(Ba_{1-x}K_x)Fe_2As_2$ using a self flux by prereacting the Ba and K to circumvent the volatility of the K. These samples are homogeneous – as determined by the narrow resistive superconducting transition – with $T_c \sim 36$ K. The crystal quality is excellent, and detailed photoemission studies have been done (Neupane et al.

(2011); Xu et al. (2011)). Unfortunately, the crystals are also small ($\lesssim 1$ mm^2), which limits their usefulness for many measurements, such as xray and neutron diffraction.

4.3 Ba(Fe$_{1-x}$TM$_x$)$_2$As$_2$ (TM=Co, Ni, Cu, Rh, Pd, Cr)

Superconductivity was first reported in TM substituted BaFe$_2$As$_2$ and RFeCoAsO by by Sefat et al. (Sefat et al. (2008a,b)). In contrast with K substitution on the Ba site, substituting other transition metals onto the Fe site is generally well behaved and uniform (with some exceptions as will be discussed in Chapters 5 and 6).

4.3.1 Ba(Fe$_{1-x}$Co$_x$)$_2$As$_2$

Co is Fe's nearest electron-contributing neighbor, and was therefore a logical first choice for TM substitution. Increasing Co substitution suppresses $T_{s,m}$ up to $x \approx 0.06$, above which the transition is fully suppressed. Superconductivity begins at $x \approx 0.03$ and reaches a maximum T_c of ~ 25 K at $x \sim 0.074$. Further Co substitution decreases T_c, until it finally vanishes again at $x \sim 0.16$ (see Fig. 4.3). Additionally, because Co is not volatile until much higher temperatures than K, it is possible to use a self-flux method (FeAs as a solvent) to synthesize these crystals (Sefat et al. (2008b); Ni et al. (2008b)). This allows Co to go into the lattice more uniformly than K (which requires a separate flux, such as Sn, or difficulty with volatility and reactivity if FeAs is used), which gives much sharper, narrower transitions (Ni et al. (2008b)). It also allows much larger crystals to be formed. The increased homogeneity and large crystals make Co substitution more suitable for detailed, sensitive probes of superconductivity in this system.

One feature of note is the split of the structural and magnetic transitions into separately observable features (Ni et al. (2008b); Pratt et al. (2011); Kim et al. (2011a)). This is different from K substitution and application of pressure, where the transition appears to remain simultaneous as the tuning variable is changed.

Because of the suitability of this system for detailed study, much work has been done on it. Many examples are described in Chapter 9.

4.3.2 $Ba(Fe_{1-x}Ni_x)_2As_2$

The next nearest neighbor after Co is Ni, providing two extra electrons per Ni instead of one per Co. As with Co, Ni substitution induces superconductivity when substituted into the lattice on the Fe site. As shown in Fig. 4.3, suppression of the structural and magnetic transitions as well as maximum T_c are similar to the behavior in Co substitution (Li et al. (2009); Ni et al. (2009)). In fact, they are nearly identical, with one key difference: Ni substitution appears to induce the changes twice as rapidly as Co substitution. Suppression of $T_{s,m}$ shows this scaling fairly well, but the features of the superconducting dome are even more clearly scaled (Ni et al. (2009)). The split in the high temperature transition is seen here, as well.

4.3.3 $Ba(Fe_{1-x}Cu_x)_2As_2$

After Ni, the next neighbor to Fe is Cu. Cu substitution was investigated to see if it would cause similar behavior as Co and Ni, essentially to answer the question, "What happens if we keep going?" As shown in Fig. 4.3, suppression of the structural and magnetic phase transitions does appear to further scale with electron count in Cu as it does in Co and Ni. There is also a splitting in the transition similar to the other transition metals. However, our group has only ever found one superconducting sample of Cu-substituted $BaFe_2As_2$, and T_c was quite low in this solitary case. The conclusion drawn from this has been that $T_{s,m}$ must be suppressed sufficiently to induce superconductivity, but that this happens too slowly in Cu compared with the increase in electron count so that by the time $T_{s,m}$ is sufficiently suppressed, this latter is too high for superconductivity to emerge. See Figs. 4.3 and 4.4. (Ni (2009); Ni et al. (2010))

One issue with Cu substitution is that there is no known convenient binary compound of Cu and As (see Fig. 3.7(b)), so it is impossible to prepare CuAs as a precursor for substituting Cu into the lattice as is done with other TM substitutions (as described by Ni et al. (2008b), for example). Instead Cu shot is added to the powder so that the stoichiometry going into the growth is $Ba(FeAs)_4Cu_x$ (Ni (2009); Ni et al. (2010)). Unfortunately, the elemental Cu does not appear to mix uniformly or predictably into the melt, so the Cu concentration varies widely from batch to batch. This makes it extremely difficult to predict what final stoichiometry will

result from a given input, which is especially problematic when preparing samples for neutron scattering experiments, which require large sample volumes.
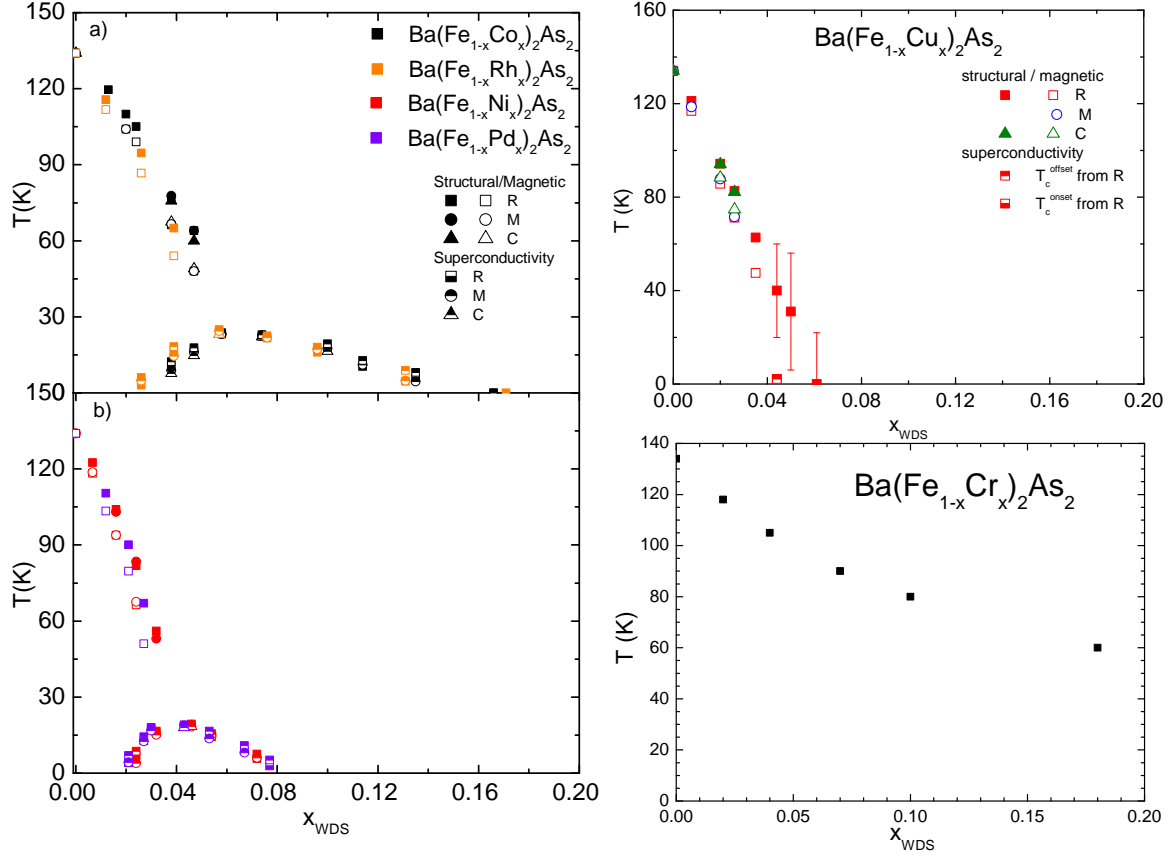
Figure 4.3: T-x phase diagrams for various TM substitutions of $BaFe_2As_2$ (Ni et al. (2008b); Sefat et al. (2009b); Ni (2009); Ni et al. (2010)).

4.3.4 $Ba(Fe_{1-x}Rh_x)_2As_2$ and $Ba(Fe_{1-x}Pd_x)_2As_2$

As shown in Fig. 4.3, Rh and Pd substitution scale almost identically to Co and Ni, both in their suppression of $T_{s,m}$ and scaling of the superconducting dome (Ni et al. (2009)). In fact, Rh and Pd substitution behave so similarly to Co and Ni (Kreyssig et al. (2010); Kim et al. (2011a)) that comparatively little work has been done on them. This is particularly interesting considering that the lattice parameters change in different ways in the 3d vs 4d TM substitutions. With Co and Ni, both a and c shrink with increasing x, resulting in an overall decrease in unit cell volume V (Ni et al. (2008b)). By contrast, both Rh and Pd substitution
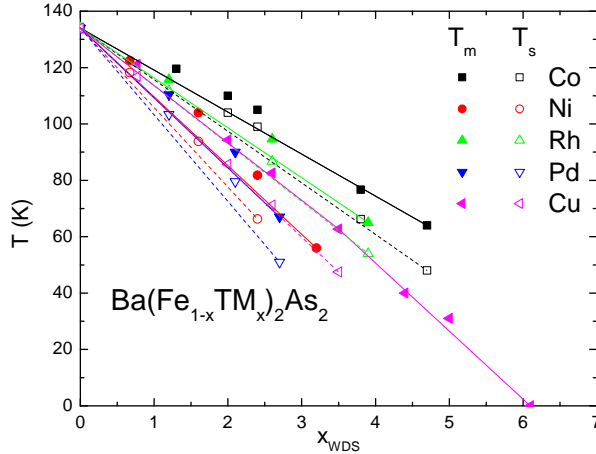
Figure 4.4: x dependence of $T_{s,m}$ in Ba(Fe$_{1-x}$TM$_x$)$_2$As$_2$(TM=Co, Ni, Rh, Pd, Cu). Here, the scaling of $T_{s,m}$ with electron count can be seen to be weaker than what is seen in the features of the superconducting dome. These points are all determined from resistance data alone (Ni et al. (2008b); Ni (2009); Ni et al. (2010)).

decrease c while increasing a, giving an overall increase in V (Ni et al. (2009)). That the phase diagrams remain so similar suggests that either the crystallographic lattice parameters are not particularly important for the behavior of this system or the c parameter alone is much more important than either a or V.

The scaling of the superconducting dome with electron count is extremely good across both 3d and 4d transition metal substitutions. This can be seen quite clearly in Fig. 4.5 (Ni et al. (2009); Ni (2009)).

4.3.5   Ba(Fe$_{1-x}$Cr$_x$)$_2$As$_2$

A limited amount of work has been put into studying the hole carrying TM substitutions of BaFe$_2$As$_2$. Of primary note are studies by Sefat et al. (2009b) and Bud'ko et al. (2009) which studied Cr substitution on the Fe site. These studies find that whereas Cr substitution suppresses $T_{s,m}$ (Fig. 4.3), there is no noticable splitting of the transition nor superconductivity down to base temperature. The lack of superconductivity is somewhat surprising given that K substitution on the Ba site (another hole carrying substitution) produces robust superconductivity. A few explanations have been proposed. Structural changes may account for part of
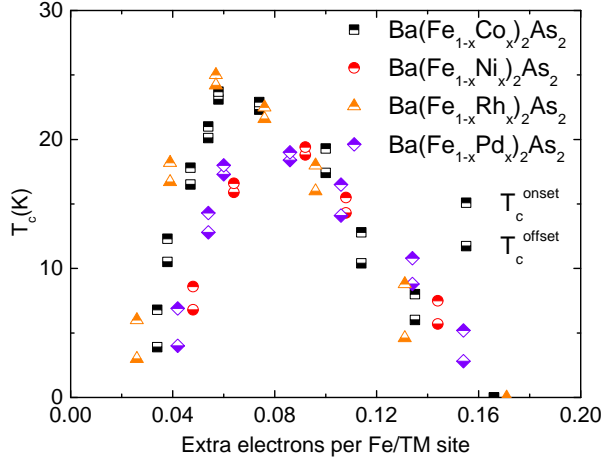
Figure 4.5: T-e phase diagram of $Ba(Fe_{1-x}TM_x)_2As_2$(TM=Co, Ni, Rh, Pd) showing only the superconducting state as determined from resistive measurements.

the difference, as Cr increases both a and c with increasing x. Another possibility is that the magnetic properties of Cr may be coming into play, destroying any nascent superconductivity. Suppression of $T_{s,m}$ is also rather slow with Cr substitution, so it may be that it is not suppressed sufficiently in the region where superconductivity would otherwise occur. It may also be that simple band filling is not an adequate explanation for superconductivity in this system, and hole contributions on the Ba site are simply different from those on the Fe site in some way.

4.4 $BaFe_2(As_{1-x}P_x)_2$

The only successful substitution onto the As site in $BaFe_2As_2$ is P. Jiang et al. (2009) demonstrated that P may be substituted onto the As site of $BaFe_2As_2$ in sufficient quantity to induce superconductivity, and Kasahara et al. (2010) showed that single crystals could be synthesized. A large fraction of the As must be substituted with P in order to induce superconductivity, with the optimal substitution for maximum T_c occuring at $x \sim 0.3$. P is also a somewhat unexpected superconductivity-inducing substitution, since it is isovalent with As and therefore should provide neither holes nor electrons. On the other hand, both a and c lattice parameters shrink and $T_{s,m}$ is suppressed with increasing x. The use of isovalent

substitution to induce superconductivity will be explored in more depth in Chapter 5.

4.5 $AEFe_2As_2$ (AE=Ca, Sr)

Ca or Sr may be fully substituted for Ba in $BaFe_2As_2$ to produce other parent compounds for related materials. Although neither of these compounds superconducts on its own under ambient conditions, both can be induced to superconductivity relatively easily (via pressure and/or chemical substitution). $SrFe_2As_2$ will superconduct under applied pressure (Alireza et al. (2009); Colombier et al. (2009)) or with some applied strain (the strain of growth is often enough). Meanwhile, $CaFe_2As_2$ behaves oddly when grown from a FeAs self flux: instead of the structural and magnetic transitions seen in $BaFe_2As_2$, $SrFe_2As_2$ and Sn grown $CaFe_2As_2$, there is, instead, a transition to a nonmagnetic, collapsed tetragonal phase below 100 K. (Ran et al. (2011)). The original behavior may be restored via annealing.

For both AE=Sr and Ca, superconductivity may be induced through chemical substitution. Unfortunately, use of Sn flux tends to dehomogenize the substitution across the sample, and the odd behavior of $CaFe_2As_2$ grown out of FeAs flux made us, as well as other groups, hesitant to explore chemical substitution in detail. However, Schnelle et al. (2009) and Qi et al. (2009) both showed that superconductivity may be induced in $SrFe_2As_2$ by substitution of Ru onto the Fe site. As described above and in Chapter 5, this is somewhat surprising given the general assumption that electron or hole contributions are important for the emergence of superconductivity in this system.

Hu et al. (2011) demonstrated that Co substitution onto the Fe site of $SrFe_2As_2$ will induce superconductivity in a similar manner as it does in $BaFe_2As_2$, though with a somewhat lower maximum T_c ($\sim$ 13 K) and higher x required for this maximum. They also show that Eu substitution onto optimally Co substituted $SrFe_2As_2$ can increase T_c further, to $\sim$17 K.

4.6 Motivation for Further Study

With these studies in mind, two transition metal substitutions that clearly needed to be examined were Ru and Mn. Ru is nominally isovalent with Fe, and Mn is the closest 3d

transition metal on the left (electron-poor) side of Fe (see Fig. 4.6). In the next two chapters, I will review Ru and Mn substitution and discuss what conclusions may be derived from this work and where they fit into the existing knowledge base.

6	7	8	9	10	11
24 Cr 52.00	25 Mn 54.94	26 Fe 55.85	27 Co 58.93	28 Ni 58.69	29 Cu 63.55
42 Mo 95.94	43 Tc 98.91	44 Ru 101.1	45 Rh 102.9	46 Pd 106.4	47 Ag 107.9

Figure 4.6: 3d and 4d transition metal neighbors of Fe.

CHAPTER 5. Physical and magnetic properties of $Ba(Fe_{1-x}Ru_x)_2As_2$ single crystals

In contrast with its 4d neighbors Rh and Pd, Ru substitution formally provides no extra electrons to the bands. However, recent polycrystalline studies in both the $SrFe_2As_2$ (Schnelle et al. (2009); Qi et al. (2009)) and $BaFe_2As_2$ (Sharma et al. (2010)) systems show that Ru substitition on the Fe site suppresses the structural/magnetic phase transition and leads to superconductivity, indicating that this system may allow a direct comparison of nominally isovalent substititon to electron doping TM substitution and pressure studies. Isovalent substition induced superconductivity, as pressure before it, indicates that whereas x and e are important parameters for tuning the phase transitions in these systems, anisotropic changes in the unit cell parameters or changes in the Stoner enhancement of the transition metal site are important as well.

Based on this, we have studied Ru substituted $BaFe_2As_2$ single crystals in order to compare the effects of isoelectronic substitution to 3d and 4d transition metal, electron substituted compounds. As we wrote this work up, similar, complimentary, studies were posted (Rullier-Albenque et al. (2010); Brouet et al. (2010)). Comparison to these data will be made as well.

5.1   Specifics of Crystal Growth

RuAs is slightly more difficult to produce than FeAs. In order to get full reaction of the Ru and As powders, longer reaction times and/or multiple reactions are required. Otherwise, the procedure is identical: Ru and As powders were combined and mixed then pressed into pellets. These pellets were sealed in SiO_2 tubes and heated as described in Chapter 3.

Crystal growth was also more troublesome than with the parent compound or with Co or

Ni substituted growths. RuAs has a higher melting temperature than FeAs, so higher concentrations of Ru require a higher spin temperature. This also causes problems with the quality of crystals produced at higher concentrations, both in terms of size and homogeneity. As Ru content increases, so does the spin temperature, decreasing ΔT between the max temperature achieved during synthesis (which can be no more than $1200°C$) and the spin temperature. Because of this, we were extremely reluctant to increase the spin temperature above $1100°C$, so above about $x = 0.35$, the crystals are too small to be usable except in basic bulk measurements and powder crystallography. Details of the inhomogeneity can be seen below.

5.2 Results

A summary of the WDS measurement data is presented in Table 5.1. For each batch, between 1 and 5 crystal surfaces were measured. The table shows the number of points measured, the nominal x value inferred from melt stoichiometry, the average x value, and two times the standard deviation of the x values measured. All x values given in this chapter are the average x_{WDS} values determined by wavelength dispersive x-ray spectroscopy (WDS). Figure 5.1 shows the measured vs nominal Ru concentration, as well as the error bars ($\pm 2\sigma$) on the measured values. For $x_{WDS} \leq 0.21$ the variation in Ru content within a batch is small, in the range of $1-5\%$ of the x value. Such variation is similar to what is found for other 3d and 4d substitution series (Ni et al. (2008b, 2009); Canfield et al. (2009); Canfield and Bud'ko (2010)). For $x \geq 0.24$ there is a sudden and rather dramatic increase in the variation of the Ru concentration within a single batch (and even a single sample). It is not clear what the origin of the change in homogeneity is, but it is also noted, albeit in a qualitative manner, in Rullier-Albenque et al. (2010) as well.

Powder x-ray diffraction measurements confirm that $Ba(Fe_{1-x}Ru_x)_2As_2$ forms in the $I4/mmm$, $ThCr_2Si_2$ structure and that impurities are minimal (Fig. 5.2). Rietveld refinement of the XRD data gives the a and c lattice parameters, which are plotted, along with the unit cell volume, as a function of x_{WDS} in Fig. 5.3.

					Ba(Fe$_{1-x}$Ru$_x$)$_2$As$_2$						
Batch #	KQ383	KQ384	KQ918	KQ919	KQ920	KQ355	KQ577	KQ368	KQ565	KQ482	KQ385
N	14	16	12	12	11	19	30	13	14	15	25
$x_{nominal}$	0.05	0.1	0.125	0.15	0.175	0.2	0.225	0.25	0.265	0.27	0.3
x_{WDS}	0.021	0.048	0.073	0.092	0.126	0.161	0.210	0.24	0.29	0.29	0.36
2σ	0.001	0.001	0.001	0.003	0.003	0.005	0.013	0.05	0.05	0.05	0.05

Table 5.1: WDS data for Ba(Fe$_{1-x}$Ru$_x$)$_2$As$_2$. N is the number of points measured in each batch, x_{WDS} is the average x value for that batch, and 2σ is twice the standard deviation of the N values measured.
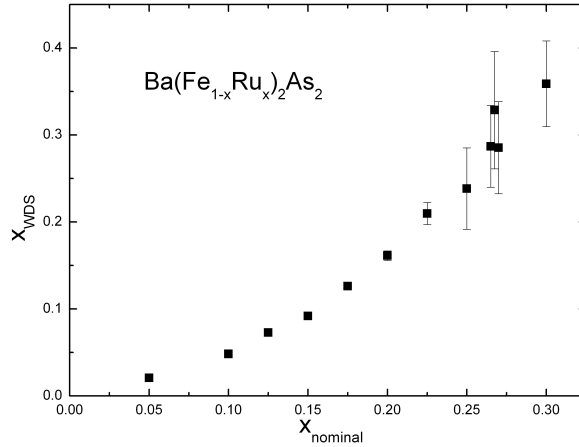
Figure 5.1: Experimentally determined Ru concentration, x_{WDS}, vs nominal Ru concentration. Error bars are $\pm 2\sigma$ (values from Table 5.1).

Figure 5.4 shows the normalized electrical resistance data of the Ba(Fe$_{1-x}$Ru$_x$)$_2$As$_2$ series from 5 K to 300 K. Normalized resistance is plotted instead of resistivity because of the tendency of these samples to exfoliate or crack (Ni et al. (2008b); Tanatar et al. (2009a,b)). The anomaly in normalized resistance at 134 K for pure BaFe$_2$As$_2$ is associated with the near simultaneous transition to the low temperature orthorhombic antiferromagnetic state (Rotter et al. (2008b)). As in the case of Co, Ni, Cu, Rh and Pd substitution (Ni et al. (2008b); Canfield et al. (2009); Ni et al. (2009); Canfield and Bud'ko (2010)), the temperature of the resistive anomaly is suppressed monotonically and the shape is changed from the sharp loss of resistance on cooling through $T_{s,m}$ seen in pure BaFe$_2$As$_2$ to a broader increase in resistance on cooling through $T_{s,m}$ for intermediate x values. For $x \geq 0.29$, anomalies associated with $T_{s,m}$ are no longer detectable. Superconductivity begins to appear above $x = 0.161$, but at this substitution fraction, we only
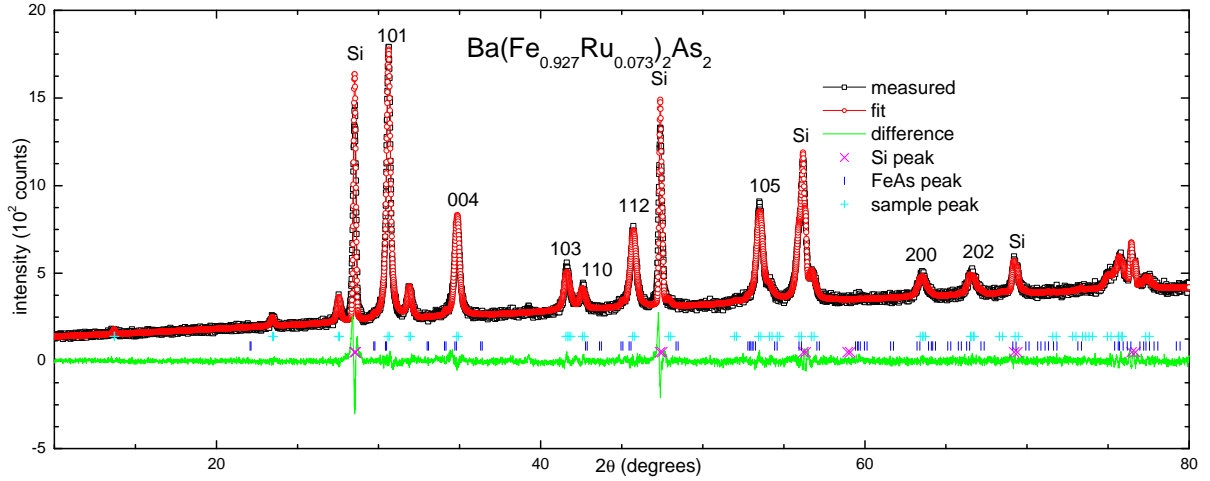
Figure 5.2: Powder x-ray pattern for $Ba(Fe_{1-x}Ru_x)_2As_2$, $x = 0.073$, with Si standard. Open symbols are measured data, closed ones are fit, the line shows the difference. $\times$, $|$ and $+$ symbols are calculated peak positions for Si, FeAs and the sample.

detect resistive onset – a rapid downturn in electrical resistance characteristic of the upper temperature region of the superconducting transition. However, the superconducting state is fully manifested ($R = 0$) by $x = 0.210$. A maximum T_c of 16.5 K is achieved at $x \approx 0.29$. T_c is suppressed for higher values of x. The superconducting transition is quite broad compared to other TM substitutions: more than 7 K wide for $x_{WDS} = 0.210$ compared with a 3 K width for a Co substitution level of $x = 0.038$ (Ni et al. (2008b)). Such a wide transition is more typical of pressure induced superconductivity rather than chemical substitution (Colombier et al. (2009)), but in this case may be associated with the Ru inhomogeneity.

Figure 5.5(a) shows high field (H=70 kOe) M/H data for representative members of the $Ba(Fe_{1-x}Ru_x)_2As_2$ series. At high temperatures the $M(T)/H$ ratio is roughly linear and decreases with decreasing temperature, with a slope that decreases with increasing Ru substitution. As with normalized resistance, the magnetization of the parent compound manifests a clear change at 134 K, correlated with the structural/magnetic phase transition (Rotter et al. (2008b)). As x is increased up to $x = 0.126$, this transition is suppressed and broadened without qualitative change. Starting with $x = 0.161$ the transition becomes much flatter and broader, and by $x = 0.24$ it is barely visible. At $x = 0.29$ it has completely vanished.
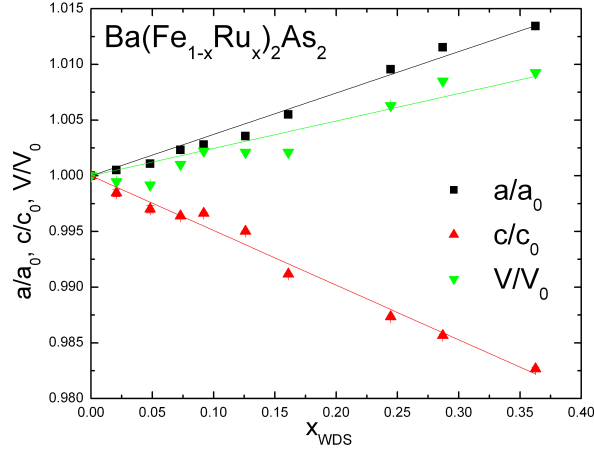
Figure 5.3: Lattice parameters for $Ba(Fe_{1-x}Ru_x)_2As_2$, compared to $BaFe_2As_2$, for which $a_0 = 3.96$ Å, $c_0 = 13.0$ Å, and $V_0 = 204$ Å^3. The slopes are $a/a_0 : (3.7 \pm 0.1) \times 10^{-4}$/Ru atom, $c/c_0 : (-4.9 \pm 0.1) \times 10^{-4}$/Ru atom, $V/V_0 : (2.4 \pm 0.2) \times 10^{-4}$/Ru atom. The trend lines are determined by a least squares fit. The error in the slope is the standard error from this fit.

Figure 5.5(b) shows the low field (50 Oe) M/H data for the superconducting members of the $Ba(Fe_{1-x}Ru_x)_2As_2$ series. These samples show a clear diamagnetic signal in the zero field cooled (ZFC) data, as well as some Meissner expulsion. It is worth noting that whereas the ZFC diamagnetic signal for Co, Ni, Rh, Pd and Cu/Co substititons are all similar and close to $-1/4\pi$ (Ni et al. (2008b, 2009); Canfield et al. (2009); Canfield and Bud'ko (2010); Ni (2009)), the low temperature values for Ru substitution (Fig. 5.5(b)) are smaller in amplitude and vary more.

5.3   Discussion

Figures 5.6 and 5.7 show normalized resistance and magnetization data, along with their derivatives, for $x = 0.073$ and $x = 0.16$ samples respectively. These figures show the criteria used for determining the structural/magnetic phase transition temperatures for these materials.

Figures 5.6(c) and 5.7(c) show comparisons of normalized resistance derivatives for Ru, Co and Rh substitutions in $BaFe_2As_2$ with similar $T_{s,m}$ values. In the Co and Rh series, a clear splitting of the two transitions is visible. (At the same temperatures, the derivatives of magnetization and heat capacity show split features as well (Ni et al. (2008b, 2009); Canfield
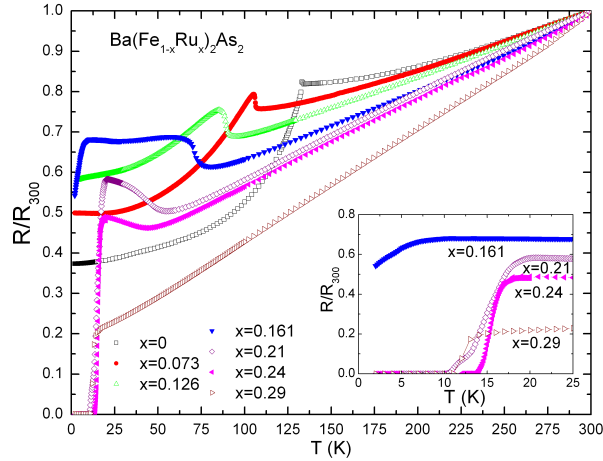
Figure 5.4: Temperature dependent resistance, normalized to the room temperature value, for select Ba(Fe$_{1-x}$Ru$_x$)$_2$As$_2$ substitution levels. Inset shows low temperature behavior.

et al. (2009); Canfield and Bud'ko (2010)).) By contrast, we do not see these separated features in the derivatives of the normalized resistance from the Ru system. These features have been shown to correspond to a splitting of the near simultaneous antiferromagnetic and structural phase transition into two separate transitions. (Ni et al. (2009); Canfield et al. (2009); Pratt et al. (2009); Canfield and Bud'ko (2010); Kreyssig et al. (2010)). Although Rullier-Albenque et al. (2010) claim to see a split transition, it appears to be a subtle feature compared to Co or Rh data. The single feature in the Ru substituted series dR/dT data suggests that either the splitting is much smaller, or absent, in this system or that the resistive feature associated with T_s is much weaker in this system. It is possible that the splitting is caused by the extra electrons provided by other TM substitutions (eg. Co, Ni, Cu, Rh, Pd).

Onset and offset criteria were used to determine T_c from the resistance data. T_c was determined from the magnetization data by extrapolating the maximum slope of the ZFC data back to the normal state. There is fair agreement between T_c^{offset} determined from normalized resistance and T_c determined from magnetization. It should be noted, though, that (i) superconductivity primarily occurs in the region where the spread in x_{WDS} is large, and (ii) the superconducting transition is broad in $R(T)$ and both ZFC and field cooled Meissner data are somewhat lower than for other TM substituted series.
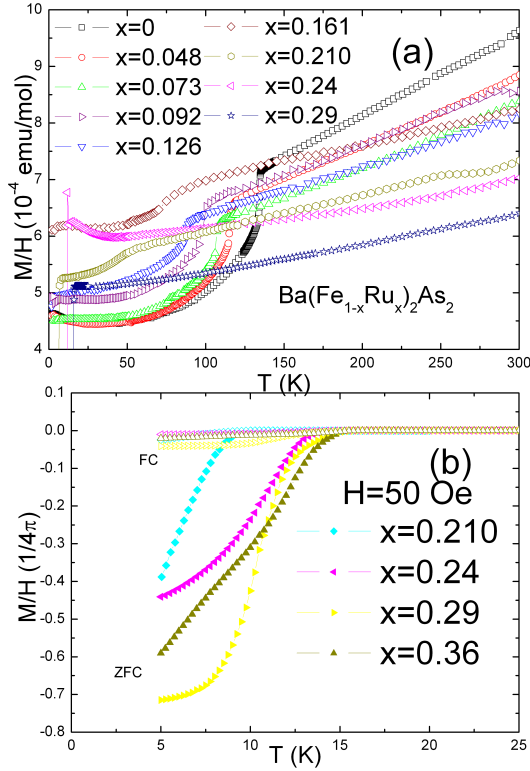
Figure 5.5: (a) Temperature dependent magnetization, scaled by applied field H=70 kOe, for $Ba(Fe_{1-x}Ru_x)_2As_2$. (b) Low temperature, low field, zero field cooled and field cooled magnetization for several superconducting members of the $Ba(Fe_{1-x}Ru_x)_2As_2$ family. $H \perp c$ for all data sets. The relatively large, low temperature, diamagnetic shielding in the zero field cooled measurements approaches that found for Co, Ni, Rh and Pd substitution (Ni et al. (2009, 2008b); Canfield et al. (2009); Canfield and Bud'ko (2010)).

Using these criteria, the data presented in Figs. 5.4 and 5.5 are summarized in a $T - x$ phase diagram shown in Fig. 5.8. Overall, the phase diagram for the $Ba(Fe_{1-x}Ru_x)_2As_2$ series is qualitatively quite similar to that of the Co, Ni, Rh and Pd diagrams: increasing x suppresses the structural/magnetic phase transition temperature ($T_{s,m}$), a superconducting dome appears above some critical x value, and this dome has a maximum near the point where $T_{s,m}$ extrapolates to zero. However, there is a key difference: suppression of $T_{s,m}$ is much slower than for other TM substitutions (Co, Ni, Cu, Rh, Pd) (Ni et al. (2008b, 2009); Canfield et al. (2009); Canfield and Bud'ko (2010); Ni (2009)). In previous comparisons of 3d and 4d TM substitutions (Ni et al. (2009); Canfield et al. (2009); Canfield and Bud'ko (2010)), we showed that suppression of $T_{s,m}$ occurs at roughly the same rate regardless of differences in size and
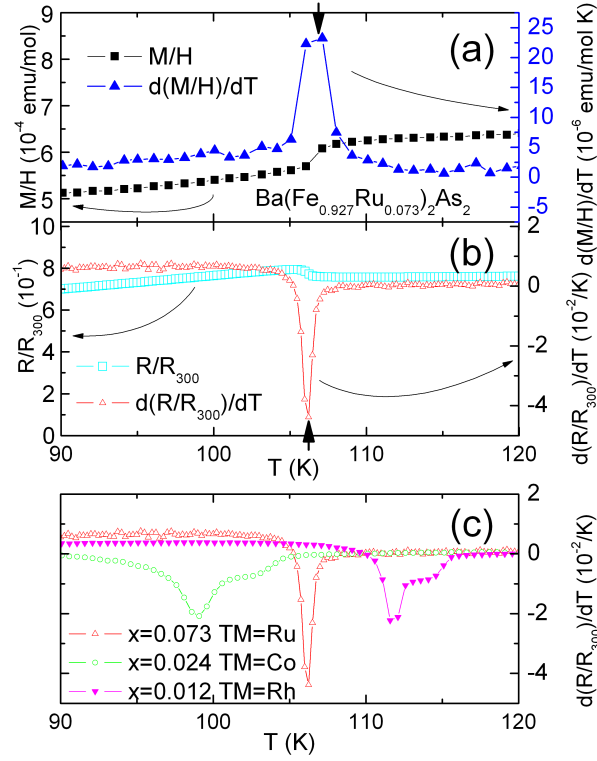
Figure 5.6: Magnetization (a) and normalized resistance (b), along with derivatives, for $Ba(Fe_{1-x}Ru_x)_2As_2$ ($x = 0.073$). Vertical arrows show the criteria for determination of the transition temperature. (c) shows normalized resistance derivative data for Co substitution (x=0.024) and Rh substitution (x=0.012) with similar transition temperatures.

electron count between substitutions; the suppression of $T_{s,m}$ in $Ba(Fe_{1-x}Ru_x)_2As_2$ is about three times slower.

Figure 5.11 shows the same lattice parameters as Fig. 5.3, but now compared with those for Rh substitution as well. The two neighboring 4d substitutions change the lattice parameters in similar ways, even though Rh substitution causes the changes faster than Ru substitution. Adding an electron is evidently much more significant to the phase diagram than steric or Stoner changes.

As in the case of Rh and Pd substituted $BaFe_2As_2$ (Ni et al. (2009)), with Ru substitution the c-lattice parameter shrinks compared to the parent $BaFe_2As_2$, while the a-lattice parameter and the unit cell volume, V, grow. (This is in contrast to the 3d TM substitutions, where all three shrink with increasing x.) As shown in Fig. 5.11, the lattice parameters of Rh and Ru
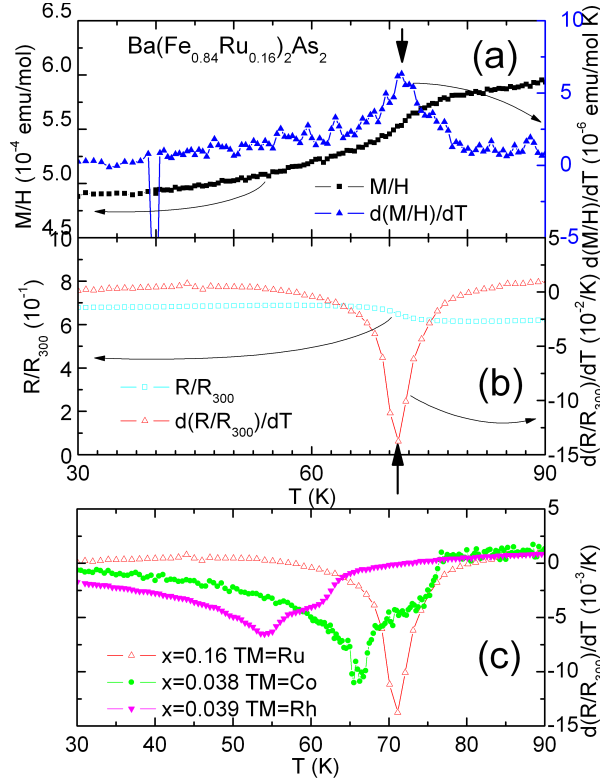
Figure 5.7: Magnetization (a) and normalized resistance (b), along with derivatives, for Ba(Fe$_{1-x}$Ru$_x$)$_2$As$_2$ ($x = 0.16$). Vertical arrows show the criteria for determination of the transition temperature. (c) shows normalized resistance derivative data for Co substitution (x=0.038) and Rh substitution (x=0.039) with similar transition temperatures.

substituted samples are nearly identical for the same substitution level. However, as seen in Fig. 5.10, the phase diagrams are quite different: Rh substitution scales much faster than Ru substitution. Because the crystallographic trends of all three 4d TM substitution series (Ru, Rh and Pd) are so similar, the major differences in their $T - x$ phase diagrams suggest that steric effects alone are not enough to explain the differences in behavior of this system with substitution (ie. the extra electrons in Rh and Pd are responsible for the much more rapid effects of TM substitution).

Although the maximum superconducting critical temperature, T_c^{max}, is significantly lower in the Ru substituted system, there is at least a superficial similarity between the Ru substituted $T - x$ phase diagram and the pressure dependent, $T - p$, phase diagram of the parent BaFe$_2$As$_2$ compound (Colombier et al. (2009)), as can be seen in Fig. 5.9. The similarity of the phase
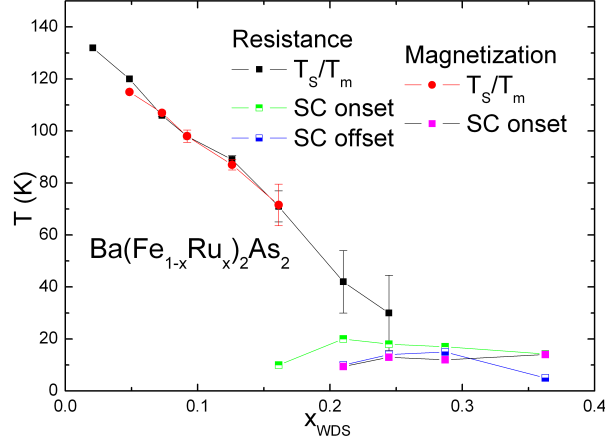
Figure 5.8: x dependent phase diagram, showing T for salient features in $Ba(Fe_{1-x}Ru_x)_2As_2$.

diagrams suggests that changes in the unit cell dimensions may be playing a large role in determining the superconducting behavior, with the effects of Ru substituion in this system being similar to physical pressure in the parent $BaFe_2As_2$ system. The difference in T_c^{max} is most likely caused by the Ru substitution disordering the Fe-plane, whereas pressure induces no such disorder.

Whereas the agreement between the $T - x$ and $T - p$ phase diagrams in Fig. 5.9 is good, the scaling between x and p was arbitrarily choosen to optimize the overlap of the two data sets. Using our data on the x-dependence of the unit cell parameters (Fig. 5.3) in combination with the data from Kimber et al. (2009) on the pressure dependence of the unit cell parameters of $BaFe_2As_2$, we can make this comparison more quantitative. Of the four combinations of the unit cell parameters: a, c, V and c/a, only c and c/a show similar responses to pressure and substitution; a and V both increase with substitution whereas they decrease with p. Figures 5.12(a) and (b) present our Ru-substitution data as well as the pressure data from Colombier et al. (2009) plotted as functions of the changes in c and c/a. A comparison of these two figures clearly indicates that c/a rather than c better parameterizes the effects of substitution and pressure. Although the agreement between the Ru substitution and pressure data is still semi-qualitative at best, this result means that, based on *these two* isoelectronic perturbations (pressure and Ru substitution), <u>if</u> a structural change has to be responsible for
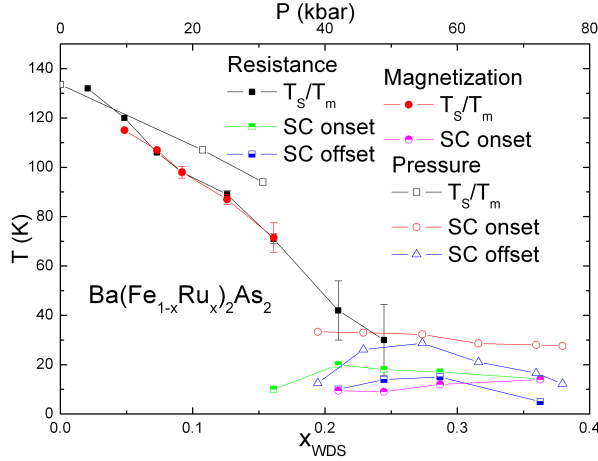
Figure 5.9: Comparison of Ru substituted phase diagram with that of the parent $BaFe_2As_2$ compound under applied pressure. (Colombier et al. (2009))

the phase diagram, then changes in the c/a ratio appear to be more important than changes in c alone. This being said, as will be discussed below, it is likely that pressure and Ru substitution affect the system differently.

The other isoelectronic substitution which produces superconductivity in $BaFe_2As_2$ is P substitution on the As site (Jiang et al. (2009); Kasahara et al. (2010)). Although the maximum T_c in the $BaFe_2(As_{1-x}P_x)_2$ system is quite a bit higher than in the $Ba(Fe_{1-x}Ru_x)_2As_2$ system ($\sim$ 30K), several key properties are similar. $T_{s,m}$ is suppressed in a relatively gradual manner and the maximum T_c value occurs at a comparably high substitution level ($x_{Ru} = 0.29$, $x_P = 0.32$) and extends over a much wider range than in any of the electron doped TM series (Jiang et al. (2009); Kasahara et al. (2010)). On the other hand, taking changes in c and a with P substitution into account, $T_{s,m}$ and T_c for P-substituted and Ru-substituted $BaFe_2As_2$ scale better with changes in c than with changes in c/a (Kasahara et al. (2010)) as shown in Fig. 5.14. This means that, if we include P-substitution as a third isoelectronic perturbation, then neither changes in c nor c/a universally describe the $T - x$ and $T - p$ phase diagrams.
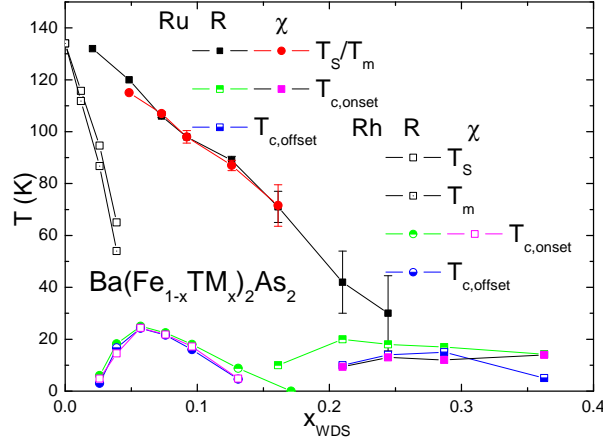
Figure 5.10: Comparison of Ru substituted phase diagram with that of the Rh substituted phase diagram.

5.4   Recent ARPES Results

Dhaka et al. have done ARPES measurements on several Ru substituted samples. (Dhaka et al. (2011)) They find that the chemical potential and Fermi surface shape of $Ba(Fe_{1-x}Ru_x)_2As_2$ does not change significantly in a wide range of Ru concentrations $(0 < x < 0.55)$. This makes Ru unique, as it does not change the low energy electronic excitation spectrum but still results in a phase diagram similar to other TM substitutions, as seen above.

The low energy band dispersion and Fermi surface are found to be very similar to the parent compound for Ru concentrations with $x \lesssim 0.55$. They also find that the band structure is highly dependent on temperature, with large changes seen between 160 K and 50 K. It is especially curious that the Fermi surface does not seem to change significantly from the low substitution levels where no superconductivity is observed to the higher ones where it is seen. These are in contrast with Co substitution, where the Fermi surface is highly dependent on the concentration, and where a Lifshitz transition is clearly observed when the concentration increases enough to produce superconductivity.
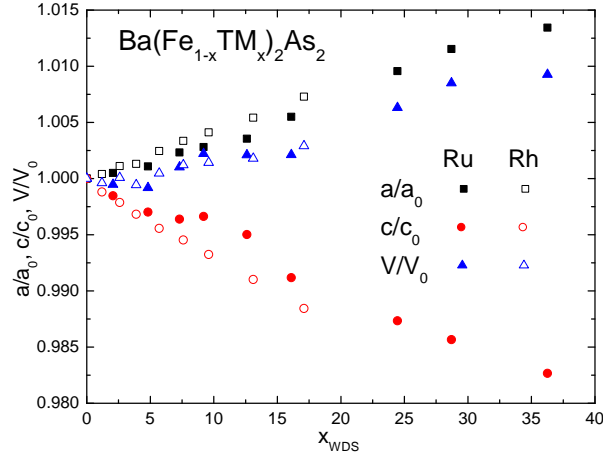
Figure 5.11: Lattice parameters for Ru and Rh substititution.

5.5 Summary

Single crystals of $Ba(Fe_{1-x}Ru_x)_2As_2$ can be grown for $x < 0.37$, although Ru homogeneity becomes less well controlled for $x > 0.21$. The structural and magnetic phase transition temperature, $T_{s,m}$, is suppressed as x increases but does not clearly split, as it does for TM = Co, Ni, Cu, Rh, and Pd substitution. As $T_{s,m}$ is suppressed superconductivity appears, reaching a maximum T_c value of 16.5 K for $x = 0.29$, near the point that $T_{s,m}$ extrapolates to $T = 0$ K. Whereas the suppression of $T_{s,m}$ and the stabilization of T_c occur at a much slower rate for Ru substitution than they do for substitution with TM = Co, Ni, Cu, Rh, or Pd, indicating that the additional electrons brought by these substitutions play a significant role in tuning of this system, there is a remarkable agreement between two isoelectronic phase diagrams (Ru-substitution and pressure) of $BaFe_2As_2$ when plotted as a function of c/a, but not when plotted as merely a function of c. However, the correlation is weak and no clear structural change seems likely to be the source of the similarity. Instead, a Stoner dilution effect seems much more plausible.
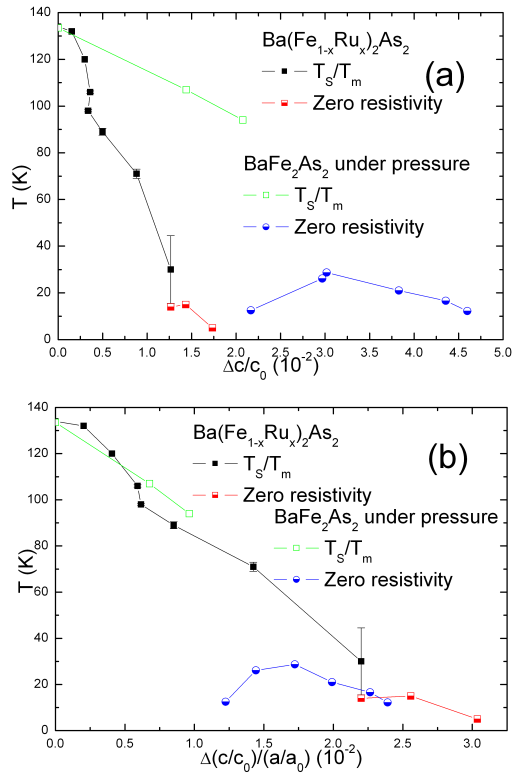
Figure 5.12: Phase diagrams of $Ba(Fe_{1-x}Ru_x)_2As_2$ and of parent $BaFe_2As_2$ under pressure, scaled by lattice parameters. (a) is scaled by $\Delta c/c_0$. (b) is scaled by $\Delta(c/c_0)/(a/a_0)$.
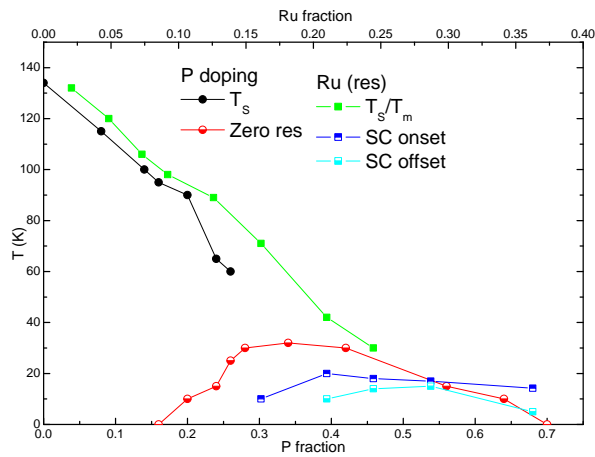
Figure 5.13: Comparison of the phase diagrams of $Ba(Fe_{1-x}Ru_x)_2As_2$ and $BaFe_2(As_{1-x}P_x)_2$. (P substitution data from Kasahara et al. (2010))
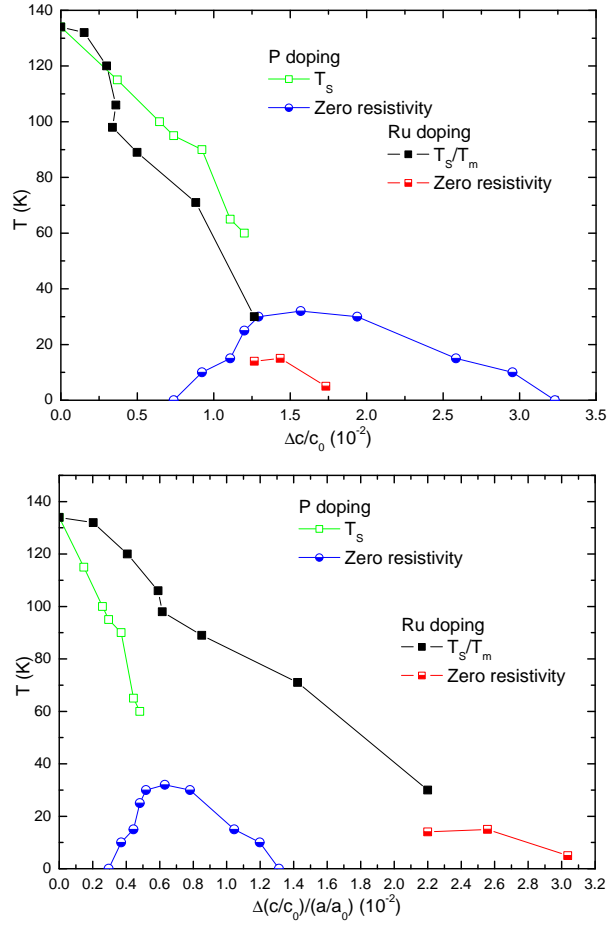
Figure 5.14: Comparison of the phase diagrams of $Ba(Fe_{1-x}Ru_x)_2As_2$ and $BaFe_2(As_{1-x}P_x)_2$, scaled by changes in c (top) and c/a (bottom). (P substitution data from Kasahara et al. (2010))

CHAPTER 6.   Physical and magnetic properties of $\mathbf{Ba(Fe_{1-x}Mn_x)_2As_2}$ single crystals

6.1   Introduction

In $BaFe_2As_2$, in contrast both with electron substitution on the Fe site and hole doping on the AE site, attempts to hole dope on the Fe site do not induce superconductivity (Sefat et al. (2009b); Bud'ko et al. (2009); Kim et al. (2010b); Marty et al. (2011)), so by comparing the properties of hole and electron doped compounds it may be possible to make inferences about the requirements for (and possibly even the mechanism of) superconductivity. Motivated by the similarity of the Co and Ni substituted phase diagrams (Ni et al. (2009); Canfield et al. (2009); Canfield and Bud'ko (2010)) and the quite different behavior of $BaFe_2As_2$ upon Cr substitution (Sefat et al. (2009b); Bud'ko et al. (2009); Marty et al. (2011)), we studied the effect of Mn substitution on the Fe site.

6.2   Specifics of Crystal Growth

MnAs is synthesized in a manner identical to FeAs, which is described in Chapter 3. Likewise, crystal growth is identical to other TM substitutions: some FeAs is replaced with MnAs and combined with Ba in a ratio of $Ba : TM : As = 1 : 4 : 4$. One issue that presents in Mn substitution is that it has a preference for phase separation, preferring to form a high Mn phase and a low Mn phase rather than a single intermediate phase above $x_{WDS} \approx 0.15$. Details are given below.

6.3 Results

WDS was performed in order to determive actual rather than nominal substitution concentration. Each WDS measurement provides composition information about sample volumes of ~ 1 μm diameter. WDS measurement data are summarized in Table 6.1 and Fig. 6.1. For each batch, up to 5 crystalline surfaces were examined. The Table shows the number of points measured, the average x value, and two times the standard deviation of the x values measured. Unless otherwise noted, all x values given here are the average x_{WDS} values determined by WDS, not the nominal x substitution. As shown, there is a clear tendency for $x > x_{nominal}$. For $x < 0.09$ the slope of the $x(x_{nominal})$ line is $\frac{\Delta x}{\Delta x_{nominal}} \approx 1.3$. For $x > 0.15$, this trend becomes dramatically stronger: x shoots upward (in comparison to $x_{nominal}$) and hints at possible phase stability or phase separation problems (see inset to Fig. 6.1).

Ba(Fe$_{1-x}$Mn$_x$)$_2$As$_2$										
Batch #	KQ902	KQ971	KQ999	SA008	KQ904	KQ905	SA022	KQ923	SA113-1	SA114	KQ924
N	15	12	12	12	13	9	12	13	12	12	14
$x_{nominal}$	0.01	0.02	0.02	0.027	0.04	0.06	0.07	0.08	0.09	0.095	0.1
x_{WDS}	0.014	0.017	0.026	0.033	0.052	0.074	0.092	0.102	0.118	0.129	0.148
2σ	0.001	0.001	0.001	0.001	0.002	0.002	0.002	0.005	0.004	0.006	0.005

Table 6.1: WDS data for Ba(Fe$_{1-x}$Mn$_x$)$_2$As$_2$, $x < 0.15$. N is the number of points measured in each batch, x_{WDS} is the average x value for that batch, and 2σ is twice the standard deviation of the N values measured.

Powder x-ray diffraction data are consistent with Ba(Fe$_{1-x}$Mn$_x$)$_2$As$_2$ forming in the I4/mmm, ThCr$_2$Si$_2$ structure. Rietvelt refinement of powder x-ray patterns using Si as a standard allows lattice parameters to be determined, from which unit cell volumes can be calculated. Normalized lattice parameters and unit cell volumes are displayed in Fig. 6.2. There is a monotonic increase in the a and c lattice parameters and unit cell volume as x increases from zero up through $x \sim 0.1$. This is consistent with the partial substitution of Fe with Cr (Ni et al. (2009); Sefat et al. (2009b)). The saturation of a and c for x larger than 0.15 is a departure from Vegard's rule, and it suggests a limit of phase stability.
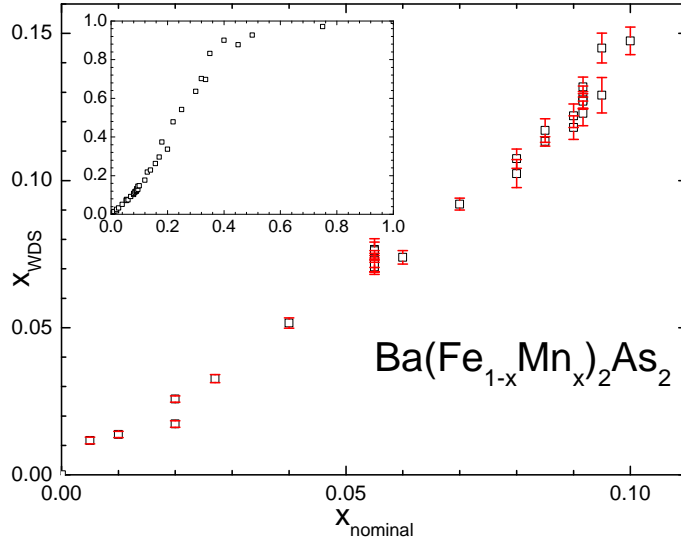
Figure 6.1: Experimentally determined Mn concentration, x_{WDS}, vs nominal Mn concentration. Error bars are $\pm 2\sigma$ (values from Table 6.1). Inset shows full substitution range.

As shown in the inset of Fig. 6.2, there is a large jump in the size of a- and c-lattice parameters near $x = 0.5$, inferred from the fits of the diffractograms. Between $x \approx 0.336$ and $x \approx 0.6$, two phases can be detected. Below $x = 0.5$, the majority phase has lattice parameters closer to the $x = 0$ values and the minority phase lattice parameters are closer to the $x = 1$ values. Above $x \sim 0.5$, the majority is near $x = 1$ and the minority is near $x = 0$. The presence of these two, closely related phases can be seen for a representative diffractogram in Fig. 6.3: neither phase can fit all of the peaks alone, but together they adequately describe all of the major features seen. The ratio of the two 200 peaks is close to unity for $x \sim 0.55$. On either side of $x \sim 0.55$, the scattering power of the minority phases decreases rapidly.

These results are consistent with a clear phase separation, as described in detail by Pandey et al. (2011). The lattice parameters of $BaMn_2As_2$ are $a = 4.1686$ Å and $c = 13.473$ Å. This is a much larger deviation from $BaFe_2As_2$ ($a = 3.9653$ Å and $c = 13.036$ Å (Ni et al. (2008b))) than either $BaCo_2As_2$ ($a = 3.9537$ Å and $c = 12.6524$ Å (Sefat et al. (2009a))) or $BaCr_2As_2$ ($a = 3.9678$ Å and $c = 13.632$ Å (Sefat et al. (2009b))). This is the likely source of the immiscibility at high x in Mn substitution. The source of this large change in lattice parameters is not fully clear: the free atomic radii of Cr, Mn, Fe and Co are all very close
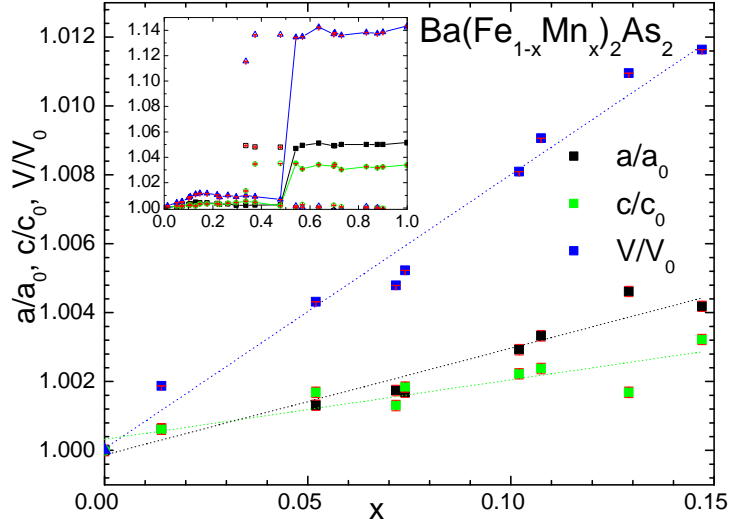
Figure 6.2: Unit cell parameters, a and c, as well as volume, V, normalized to those of the parent compound $BaFe_2As_2$, for which $a_0 = 3.96$ Å, $c_0 = 13.0$ Å and $V_0 = 204$ Å^3. The open symbols at $x = 0$ are previously published data for the parent compound. Dashed lines are guides to the eye. Inset: full range $0 < x < 1$. Open symbols are minority phase lattice parameters.

(Ni et al. (2009); Sefat et al. (2009b)), with Co deviating the most from Fe. The ionic radii of the four transition metals are also similar (depending on the charge and spin state), with Cr deviating the most from Fe (Burns (1993)). Thus, steric effects alone are not enough to account for the large shift in lattice parameters when comparing $BaMn_2As_2$ with its transition metal neighbors. It is likely that the strong magnetism of the Mn atoms is at least partly responsible for the difference, most probably via high spin/low spin effects (Pandey et al. (2011)).

For these reasons, we limit our investigation of thermodynamic and transport properties of this series to $x < 0.15$, where the parameters shown in Fig. 6.2 still roughly follow Vegard's law. It is important to note, though, that we did not see any such immiscibility manifesting as a dramatic increase in the standard deviation of x (see Table. 6.1). This implies that the spot volume probed by the electron beam of the WDS microprobe ($\sim 1\mu m^3$) is larger than the characteristic length scale of the phase separated regions.

Fig. 6.4 shows the normalized electrical resistivity data of the $Ba(Fe_{1-x}Mn_x)_2As_2$ series from 2 K to 300 K. Normalized resistivity is plotted instead of resistivity because of the ten-
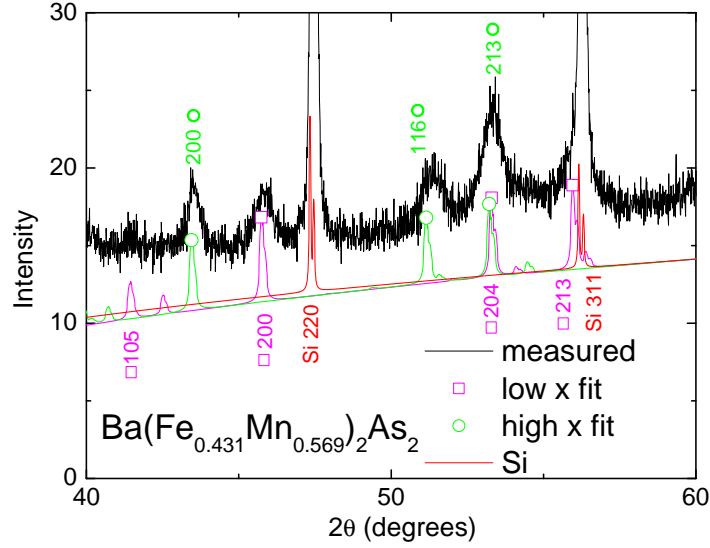
Figure 6.3: Powder x-ray pattern for $x = 0.569$, showing both high and low concentration fits. The strong peaks near $47°$ and $56°$ are from the Si standard. The $56°$ peak is near to the hkl=213 peak expected from the lower concentration fit.

dency of these samples to exfoliate or crack (Ni et al. (2008b); Tanatar et al. (2009a,b)). The anomaly in resistivity at 134 K for pure $BaFe_2As_2$ is associated with the structural/magnetic phase transitions (Rotter et al. (2008b)), and can clearly be seen in the derivative of the resistivity (Ni et al. (2008b)), which is shown in Fig. 6.5. As in the case of other TM substitutions (Ni et al. (2008b); Canfield et al. (2009); Ni et al. (2009); Canfield and Bud'ko (2010)), with Mn substitition the temperature of the resistive anomaly is suppressed and the shape is changed from a sharp decrease to a broadened increase as x increases. The anomaly becomes extremely broad around $x = 0.1$, and is no longer detectable by $x = 0.147$. For $T > 2$ K, no superconductivity (not even hints of filamentary superconductivity) is observed for any measured substitution level.

Although this low x anomaly in resistivity disappears slightly above $x \sim 0.1$ (Figs. 6.4(a) and 6.5(a)), there is still a feature of note at higher substitution levels (Figs. 6.4(b) and 6.5(b)). For $x > 0.1$, a broad minimum in the derivative of the resistance, associated with a maximal, negative dR/dT value, is evident. The temperature of this minimum gradually increases with substitution level and, as will be discussed below, follows the temperature above which neutron

scattering no longer observes magnetic scattering characteristic of long range order (Kim et al. (2010b)).
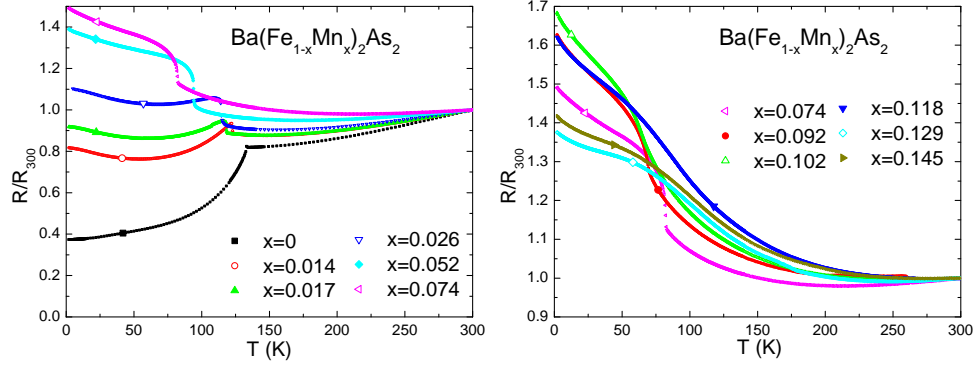
Figure 6.4: Temperature dependent resistivity, normalized to the room temperature value, for $Ba(Fe_{1-x}Mn_x)_2As_2$. The $x = 0.074$ data are shown in both panels for the sake of comparison.
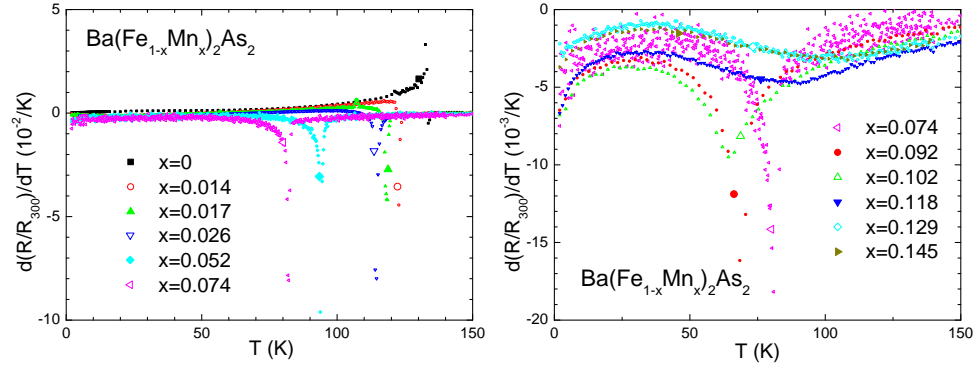
Figure 6.5: First derivative of normalized resistivity for $Ba(Fe_{1-x}Mn_x)_2As_2$. The $x = 0.074$ data are shown in both panels for the sake of comparison.

Signatures of the structural/magnetic phase transition in the lower substitution region are also seen in magnetization data: Figures 6.6 and 6.7 show temperature dependent magnetization data of the $Ba(Fe_{1-x}Mn_x)_2As_2$ series from 2 K to 300 K for both directions of the applied field and Figs. 6.8 and 6.9 show the derivatives of the temperature dependent magnetization data. For both directions of the applied field, a sharp feature can be seen at the structural/magnetic transition temperature for $x \leq 0.092$. For $x = 0.102$ the feature has broadened and become harder to resolve, and for $x > 0.102$ no feature that can be easily associated

with a transition can be found in the $M(T)$ or $dM(T)/dT$ data. It is also at this concentration that the general trend of $M(T)$ increasing with increasing x ends.
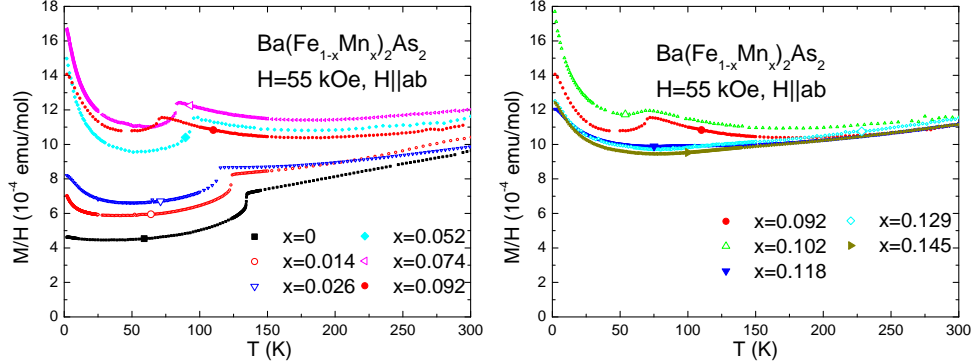
Figure 6.6: Temperature dependent magnetization for $Ba(Fe_{1-x}Mn_x)_2As_2$ with $H||ab$. In all cases, $H = 55\ kOe$. The $x = 0.092$ data are shown in both panels for the sake of comparison.
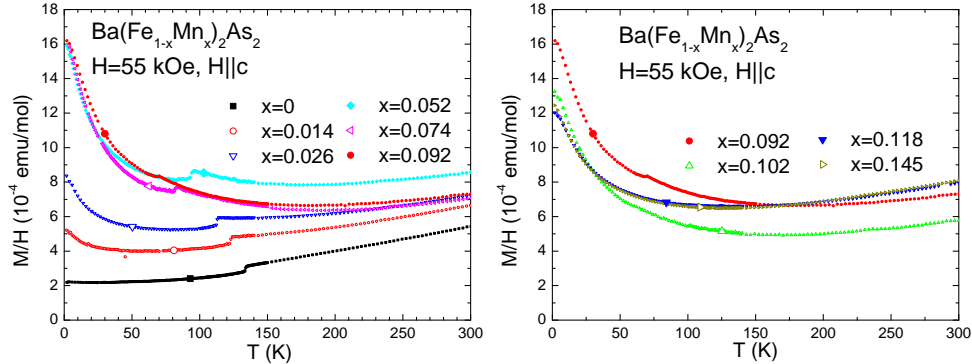
Figure 6.7: Temperature dependent magnetization for $Ba(Fe_{1-x}Mn_x)_2As_2$ with $H||c$. In all cases, $H = 55\ kOe$. The $x = 0.092$ data are shown in both panels for the sake of comparison.

Fig. 6.10 shows the field dependent magnetization (with $H||ab$) of the $Ba(Fe_{1-x}Mn_x)_2As_2$ series at 2 K. In the substitution range we have explored, there is no evidence of a ferromagnetic component to the magnetization, and only slight non-linearity that could be associated with Brillouin saturation of paramagnetic local moments. This suggests that if there is a little residual flux present in these samples, it does not contain MnAs since MnAs is a ferromagnet with $T_C \approx 318$ K (Singh et al. (2009)). Although it is tempting to try to associate the low temperature upturn in magnetization, seen most clearly for intermediate x values, with a Curie
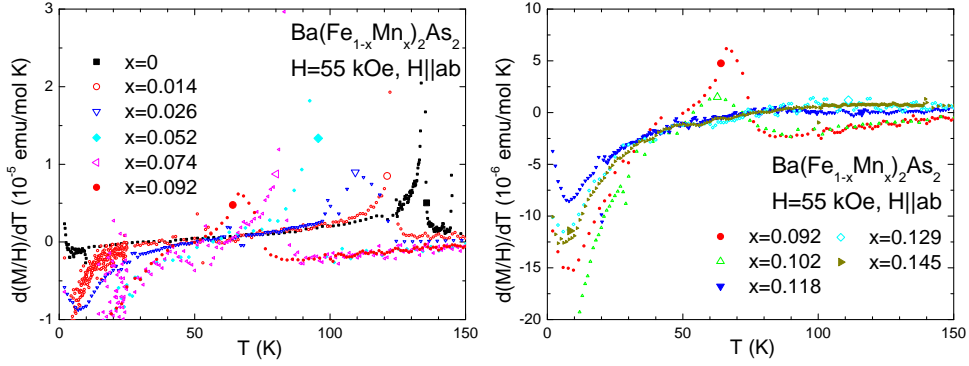
Figure 6.8: Derivatives of the temperature dependent magnetization for $Ba(Fe_{1-x}Mn_x)_2As_2$ with $H||ab$. In all cases, $H = 55\ kOe$. The $x = 0.092$ data are shown in both panels for the sake of comparison.
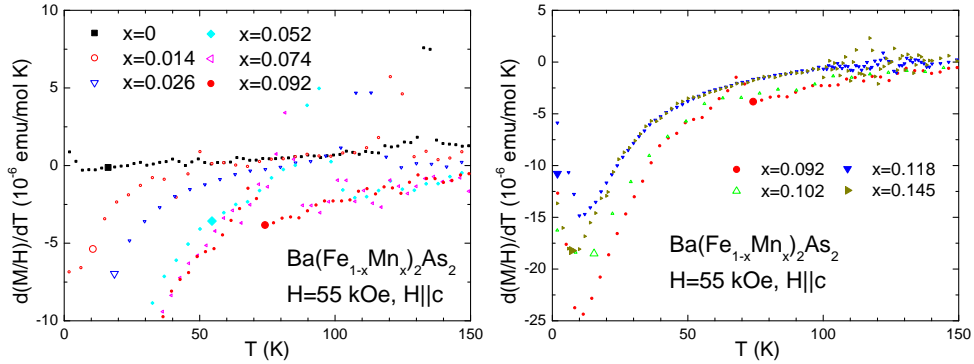
Figure 6.9: Derivatives of the temperature dependent magnetization for $Ba(Fe_{1-x}Mn_x)_2As_2$ with $H||c$. In all cases, $H = 55\ kOe$. The $x = 0.092$ data are shown in both panels for the sake of comparison.

tail coming from paramagnetic impurities, this is difficult. Since the size of this upturn-like feature diminishes as x increases for higher substitution levels, it is hard to simply associate with increased Mn levels.

6.4   Discussion

Figures 6.11(a) and (b) show magnetization data with its derivative and normalized resistance with its derivative, respectively, for one substitution level ($x = 0.074$). The maximum (minimum) of a Gaussian fit of the feature in the derivative, shown with an arrow, gives the
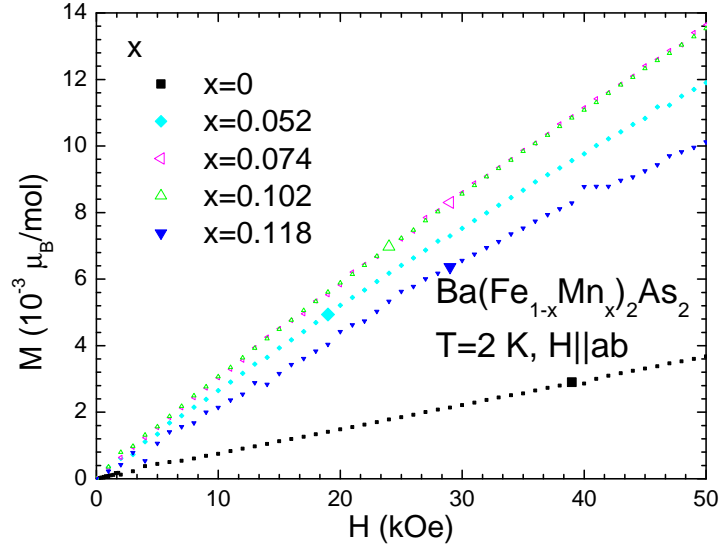
Figure 6.10: Field dependent magnetization for $Ba(Fe_{1-x}Mn_x)_2As_2$, $H||ab$. In all cases, $T = 2K$.

value of the transition temperature used throughout this work. The uncertainty is taken as the full-width, half-max of this Gaussian fit.

As seen in Fig. 6.12, a T-x phase diagram for the $Ba(Fe_{1-x}Mn_x)_2As_2$ system can be constructed by applying these criteria to the data from each member of the substituted series. Note that whereas a resistive feature is seen for all $x < 0.15$, the magnetic transition signature is absent for $x > 0.1$. Substitution of Mn for Fe suppresses the high temperature tetragonal to orthorhombic and antiferromagnetic phase transition, bringing it to a clear minimal value of ~ 65 K for $x \sim 0.1$, at the approximate rate of 7 K/%Mn. Of primary interest are the absence of superconductivity and the lack of splitting between the structural and magnetic phase transition temperatures. This latter point is most clearly illustrated in Fig. 6.11(c), where we show resistive derivatives of both Mn and Co substituted samples with similar transition temperatures. The data from the Co substituted sample show two distinct features: a sharp minimum which has been associated with the magnetic transition and a somewhat higher temperature "shoulder" associated with the structural transition. By contrast, the data from the Mn substituted sample shows only the sharp minimum. This is similar to the parent compound, where the transitions are seen at essentially the same temperature (134 K). This clear lack of splitting
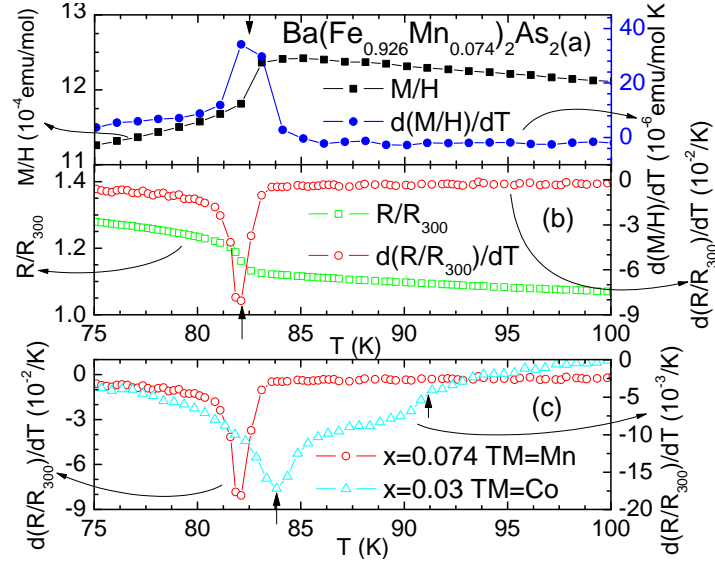
Figure 6.11: Magnetization (a) and resistivity (b), along with derivatives, for $Ba(Fe_{1-x}Mn_x)_2As_2$ ($x = 0.074$). Vertical arrows show criterion for transition temperature. (c) shows resistivity derivative data for Co substitution (x=0.03) with a similar transition temperature, with the vertical arrows indicating the higher temperature structural and lower temperature magnetic transitions.

for $x < 0.1$ is conclusively demonstrated by neutron and x-ray scattering measurements (Kim et al. (2010b)).

Figure 6.12 shows that there is excellent agreement between transition temperature values inferred from different measurement techniques for $x < 0.1$: $T_{s/m}$ as measured by resistance, magnetization, thermopower and scattering techniques (Kim et al. (2010b); Thaler et al. (2011)) are very close (less than 1 K difference). For $x > 0.1$, the features are broadened. The temperature associated with the broad minimum in the temperature dependent derivative of the resistance agrees well with the temperature associated with the onset of long range magnetic order (T^* in Fig. 6.12) and for several series members with $0.10 < x < 0.15$ a small shoulder-like feature can be detected near the temperature that magnetic scattering is first detected (Fig. 6.12, with scattering data from Kim et al. (2010b)).

Kim et al. have done xray and neutron scattering on this substitution. (Kim et al. (2010b)) They find that while the magnetic Bragg peaks are consistent with the stripelike antiferromagnetic structure found in other iron arsenide compounds, the splitting of the (1 1 10) charge peak
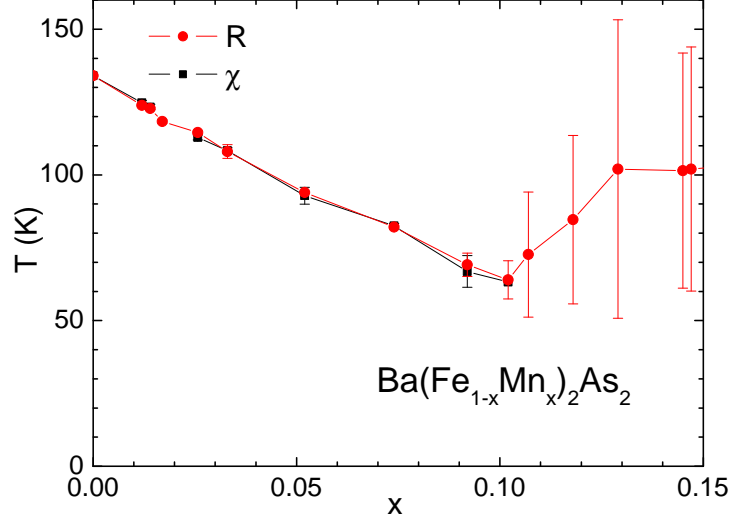
Figure 6.12: T-x phase diagram for $Ba(Fe_{1-x}Mn_x)_2As_2$ single crystals for $0 < x < 0.15$.

associated with the orthorhombic distortion seen with other substitutions does not appear to happen here. For $x \leq 0.074$, they see antiferromagnetic and structural transitions coincident in temperature. For $x = 0.102$, a weak "tail" of magnetic scattering extends to temperatures above the structural transition. For $x \geq 0.118$, the structural transition is absent entirely and the temperature evolution of the antiferromagnetic order is very different from what is seen at lower Mn concentrations. The data on these low substitution levels shows that the structural and magnetic transitions are tightly locked, consistent with what we have seen in resistance and magnetization.

At these higher concentrations, there is a broadening of the magnetic peak above a temperature T^* which is itself above the magnetic transition temperature. For $x \leq 0.074$, the phase line between the paramagnetic tetragonal and antiferromagnetic orthorhombic phases is easily determined. However, for $x \geq 0.102$, the onset of long range order is more difficult to detect. Thus the clarification of T^*, which is the temperature below which the width of the magnetic peak is limited by the instrumental resolution. T^* follows the same trend seen for the maxima of $\frac{dR}{dT}$ seen in Fig. 6.5(b).

The effects of Mn substitution can be compared with those of Cr substitution. Both substitutions increase both the a and c lattice parameters with x (Sefat et al. (2009b)), but at
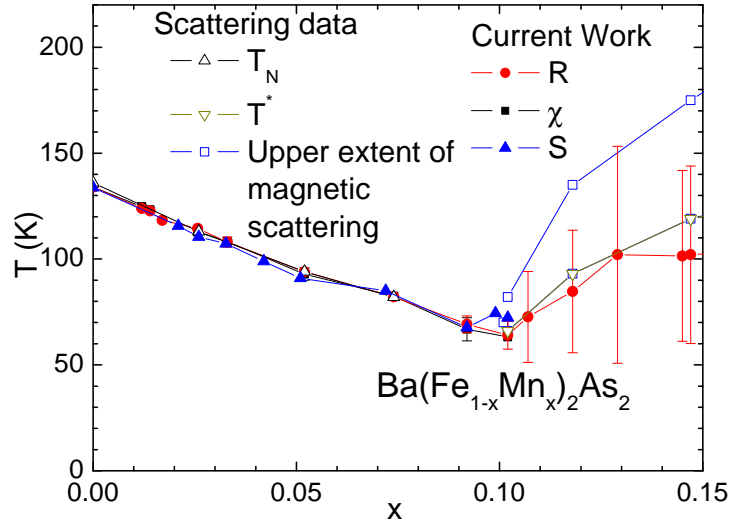
Figure 6.13: T-x phase diagram for $Ba(Fe_{1-x}Mn_x)_2As_2$ single crystals for $0 < x < 0.2$, now compared with results from neutron scattering and from thermopower measurements for comparison.Thaler et al. (2011); Kim et al. (2010b) For $x \gtrsim 0.1$ the transition temperature inferred from the broad resistive feature roughly agrees with the temperature (T^*) below which neutron scattering detects long range magnetic order (Kim et al. (2010b)).

different rates. At $x \sim 0.1$, the change in unit cell volume for both Mn and Cr substitutions is about 0.8%, even though the change in a is about 0.05% in Cr and 0.3% in Mn and the change in c is 0.7% in Cr and 0.2% in Mn. Figure 6.14 shows a comparison of the T-x phase diagrams of the two compounds. Below $x \sim 0.1$, they are quite similar: both display suppression of $T_{s/m}$ to similar degrees, and neither shows any evidence of superconductivity. Above $x \sim 0.1$ however, they begin to differ: in contrast to the full suppression of the structural transition in $Ba(Fe_{1-x}Mn_x)_2As_2$ above $x \sim 0.1$ (Kim et al. (2010b)), the structural transition is observed in $Ba(Fe_{1-x}Cr_x)_2As_2$ up to at least $x \approx 0.18$.(Marty et al. (2011)) In addition, the magnetic transition temperature monotonically decreases over the entire range in the Cr substituted series (Sefat et al. (2009b); Marty et al. (2011)), in contrast with the upturn seen in Mn substitution.

Fig. 6.15 highlights some of the key differences between Mn and Co substitution for $x < 0.15$. Of primary interest is the difference in the slope of the suppression of $T_{s/m}$. When comparing Co, Ni and Cu substitution, the suppression is seen to be dependent on atomic substitution concentration regardless of which substitution is used, and is thus not seen to be dependent
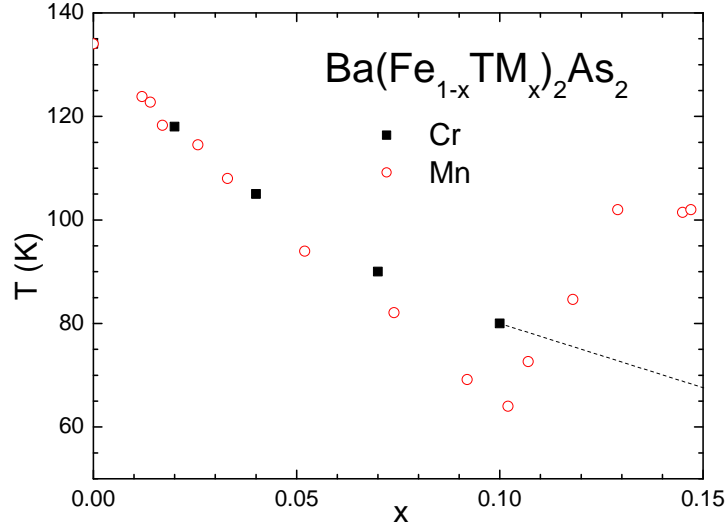
Figure 6.14: Comparison of the T-x phase diagrams of $Ba(Fe_{1-x}Mn_x)_2As_2$ and $Ba(Fe_{1-x}Cr_x)_2As_2$ (Sefat et al. (2009b)) for $0 < x < 0.15$. The dashed line connects to the next higher substitution concentration in the Cr series ($x = 0.18$), but we do not present that part of our data here because we are unsure of the possible effect of phase separation above $x \sim 0.15$.

on the number of extra carriers (Canfield et al. (2009)). By contrast, the slope with Mn (or Cr) substitution is about half as steep. It is unclear if this is due to the difference between electron and hole substitution or other differences such as structural changes. In addition, for Co, Ni, Rh, Pd and Cu, substitution appears to split the structural and magnetic transition temperatures (Canfield and Bud'ko (2010)), T_s and T_m, with a maximum split of 16 K at 5.8% Co, 19 K at 3.2% Ni and 15 K at 3.5% Cu.(Ni et al. (2010)) For Mn substititution though, there is no resoluble splitting in the transport, thermodynamic or microscopic (Kim et al. (2010b)) data for $x \lesssim 0.1$.

Taking the minimum value for $T_{s/m} \approx 65$ K at $x \sim 0.1$ in the $Ba(Fe_{1-x}Mn_x)_2As_2$ system and comparing it to the $Ba(Fe_{1-x}Co_x)_2As_2$ series, we get that the equivalent Co substitution concentration for the same magnetic transition temperature is $x \sim 0.04$. This is on the low substituted side of the superconducting dome, but with a well defined $T_c \approx 11$ K (Ni et al. (2008b)). We clearly do not see any sign of such superconductivity at this Mn composition. This indicates that the well defined scaling of T_c with suppression of T_s or T_m that is seen for
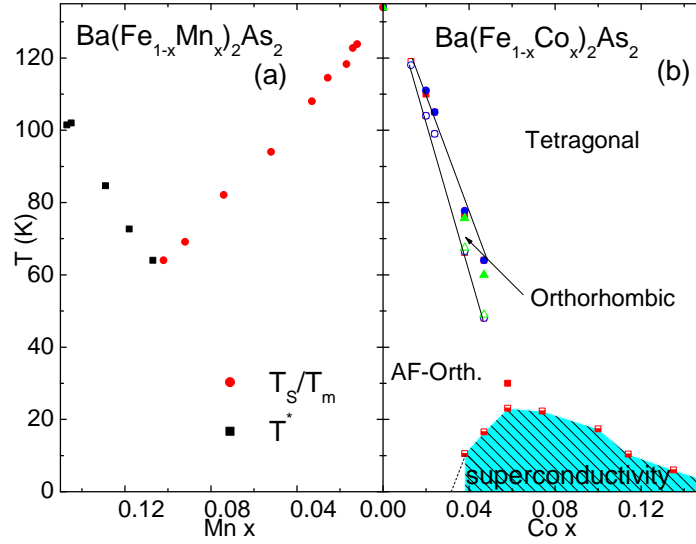
Figure 6.15: (a) $Ba(Fe_{1-x}Mn_x)_2As_2$ $T-x$ phase diagram. (b) $Ba(Fe_{1-x}Co_x)_2As_2$ phase diagram (Ni et al. (2008b)).

TM = Co, Ni, Rh, and Pd substitution (Canfield et al. (2009); Ni et al. (2009); Canfield and Bud'ko (2010)) does not hold for TM = Mn. It is possible that the lack of superconductivity is caused by Mn not suppressing the antiferromagnetic phase to a low enough temperature in the right way: the superconducting transition may be cut off by the minimum in the temperature of the phase transition and the change in the nature of the ordering above that minimum. This is also the substitution level at which T_S vanishes, whereas in superconducting TM substitutions, the tetragonal to orthorhombic phase transition is still quite apparent.

6.5   Summary

Single crystals of $Ba(Fe_{1-x}Mn_x)_2As_2$ can be flux grown for a continuous range of substitution concentrations from $0 < x < 0.15$. Samples with homogeneous, single phase concentrations above this can not easily be grown, as the crystals phase separate into Mn- and Fe-rich mesoscopic regions at intermediate substitutions. As x increases from zero up to $x \approx 0.1$, the structural and magnetic phase transition temperature, T_s/T_m, is suppressed but does not clearly split as it does for TM = Co, Ni, Cu, Rh, and Pd substitution. For $x > 0.1$, a resistive feature associated with magnetic ordering is observed with a transition temperature that in-

creases with x. Superconductivity is not observed for any value of x. The suppression of T_s/T_m occurs at a slower rate for Mn substitution than for substitution with TM = Co, and slightly more quickly than for TM = Cr.

6.6   Further Work

Thermoelectric power and resistance under pressure measurements were performed on these samples. The details of the data and experimental methods are discussed in a publication from our group (Thaler et al. (2011)), but since they were primarily taken and analyzed by Halyna Hodovanets (TEP) and Milton Torikachvili (pressure), rather than myself, they are not presented in detail here. However, Fig. 6.13 shows that there is good agreement between the resistance and magnetization measurements presented here and the thermopower data.

CHAPTER 7.   Double-substitution: properties of $Ba(Fe_{1-x-y}Co_xTM_y)_2As_2$ (TM=Cr, Mn) single crystals

7.1   Introduction

For "electron rich" transition metal substitution on the Fe site of $BaFe_2As_2$, we have observed that many properties of the phase space scale very closely with electron count, with both 3d and 4d transition metal substitutions following this trend (Ni et al. (2009)). As discussed in Chapter 6 (as well as by Sefat et al. (2009b) and Bud'ko et al. (2009)), substitution of Mn or Cr for Fe in $BaFe_2As_2$ suppresses the structural and magnetic phase transitions but does not induce superconductivity at any substitution level. To test whether Mn and Cr introduce hole-like carriers in the same way that Co or Ni introduce electron-like carriers, we wanted to investigate the effects of simultaneous substitution of either Mn or Cr along with Co and see if this would allow us to tune the system by 'walking' back and forth along the superconducting dome (Fig. 4.5).

7.2   Specifics of Crystal Growth

CrAs is synthesized in a manner very similar to that used for FeAs, which is described in Chapter 3. One problem was that Cr powder was difficult to obtain, so small pieces of elemental Cr were smashed in a small, table-top anvil and then ground with an agate mortar and pestle. Another issue is that Cr does not react with As as easily as the other transition metals we commonly use as substitutions (Mn, Fe, Co, Ni, Ru, Rh and Pd), so synthesis required multiple reactions. Our CrAs was synthesized before we had access to the rotating tube furnace attachment described in Chapter 3, so all of our CrAs was prepared by creating CrAs pellets out of Cr and As powders. These pellets were heated as described in Chapter 3,

but then they had to be reground and pressed into new pellets and heated again. This process was repeated until no free As is observed in the reaction tube, which sometimes required several iterations. Fortunately because As sublimates at $\sim 513°$C, any free As became vapor which deposited itself on the inside walls of the tube, making it is fairly easy to detect the presence of free As. The crystal growth process was identical to single transition metal substitutions: some FeAs was replaced with CoAs and either MnAs or CrAs and combined with Ba in a ratio of Ba:TM:As=1:4:4. Because of the presence of Cr, slightly higher spin temperatures of $1025 - 1050°$C had to be used. The problem with phase separation seen in Mn substitution described in Chapter 6 was hopefully avoided by use of low substitution levels.

7.3   Results

WDS was performed in order to determine actual rather than nominal substitution concentration. Each WDS measurement provides composition information about sample volumes of ~ 1 μm diameter. WDS measurement data are summarized in Tables 7.1 and 7.2 For each batch, up to 5 crystalline surfaces were examined. The table shows the number of points measured, the average x and y values, and two times the standard deviation of the x and y values measured. Unless otherwise noted, all x and y values given here are the average x_{WDS} or y_{WDS} values determined by WDS, not the nominal x or y substitution. Comparing the ratio of WDS to nominal substitution concentrations in these double substitututed growths with those in the single substitutions of Co or Mn (see Chapters 4 and 6), we see that Co, Cr and Mn preferentially substitute themselves for Fe rather than competing with each other (see Fig. 7.1). This means that when aiming for a particular WDS substitution of Co and Cr or Mn, our experience from the single substitutions could be used to determine the appropriate nominal substitution level.

Ba(Fe$_{1-x-y}$Co$_x$Cr$_y$)$_2$As$_2$													
Batch #	KQ715	KQ714	MC137-1	SA639	MC137-2	KQ716	MC154	SA640	KQ989	MC161	MC157	MC156	MC155
N	24	26	12	12	12	32	12	12	13	12	12	12	12
$x_{nominal}$	0.063	0.063	0.058	0.063	0.058	0.063	0.070	0.063	0.063	0.075	0.078	0.075	0.073
x_{WDS}	0.036	0.048	0.047	0.048	0.046	0.048	0.050	0.050	0.049	0.054	0.057	0.055	0.053
$2\sigma_x$	0.003	0.002	0.005	0.002	0.004	0.002	0.002	0.004	0.001	0.005	0.001	0.003	0.003
$y_{nominal}$	0.020	0.010	0.020	0.020	0.020	0.030	0.030	0.045	0.072	0.018	0.030	0.030	0.030
y_{WDS}	0.013	0.002	0.011	0.011	0.013	0.020	0.021	0.032	0.069	0.012	0.021	0.021	0.022
$2\sigma_y$	0.002	0.001	0.002	0.003	0.003	0.002	0.002	0.002	0.003	0.002	0.001	0.003	0.002
Batch #	MC160	MC239	MC240	MC243	MC242	KQ717	KQ718	KQ719	SA641	SA556	SA557	SA558	SA559
N	12	12	12	12	12	27	28	26	12	24	12	12	12
$x_{nominal}$	0.075	0.079	0.080	0.087	0.085	0.100	0.100	0.100	0.100	0.150	0.150	0.150	0.150
x_{WDS}	0.055	0.058	0.058	0.066	0.063	0.078	0.076	0.077	0.077	0.122	0.120	0.119	0.121
$2\sigma_x$	0.003	0.002	0.002	0.002	0.003	0.003	0.003	0.002	0.004	0.002	0.003	0.002	0.003
$y_{nominal}$	0.045	0.030	0.030	0.030	0.030	0.010	0.020	0.030	0.045	0.010	0.020	0.030	0.040
y_{WDS}	0.032	0.018	0.019	0.020	0.022	0.003	0.011	0.020	0.031	0.007	0.013	0.020	0.025
$2\sigma_y$	0.001	0.001	0.001	0.001	0.003	0.002	0.002	0.002	0.003	0.002	0.002	0.002	0.002

Table 7.1: WDS data for Ba(Fe$_{1-x-y}$Co$_x$Cr$_y$)$_2$As$_2$. N is the number of points measured in each batch, x$_{WDS}$ and y_{WDS} are the average values for that batch, and 2σ is twice the standard deviation of the N values measured.

Ba(Fe$_{1-x-y}$Co$_x$Mn$_y$)$_2$As$_2$								
Batch #	KQ911	KQ958	KQ959	KQ910	SA596	KQ961	KQ962	SA597
N	16	12	14	15	12	9	13	12
$x_{nominal}$	0.063	0.063	0.063	0.063	0.063	0.100	0.100	0.100
x_{WDS}	0.047	0.047	0.046	0.049	0.050	0.072	0.071	0.076
$2\sigma_x$	0.001	0.002	0.001	0.002	0.001	0.002	0.002	0.002
$y_{nominal}$	0.020	0.040	0.060	0.010	0.030	0.040	0.060	0.010
y_{WDS}	0.023	0.048	0.069	0.012	0.035	0.046	0.075	0.012
$2\sigma_y$	0.001	0.003	0.003	0.001	0.001	0.002	0.003	0.002
Batch #	KQ960	SA598	SA223	MC303	MC304	SA224	SA225	
N	10	12	12	12	12	12	12	
$x_{nominal}$	0.100	0.100	0.150	0.150	0.150	0.150	0.150	
x_{WDS}	0.077	0.074	0.123	0.124	0.114	0.120	0.116	
$2\sigma_x$	0.002	0.002	0.002	0.003	0.004	0.003	0.004	
$y_{nominal}$	0.020	0.030	0.010	0.008	0.002	0.020	0.040	
y_{WDS}	0.023	0.034	0.006	0.010	0.019	0.022	0.047	
$2\sigma_y$	0.001	0.002	0.002	0.001	0.001	0.002	0.002	

Table 7.2: WDS data for Ba(Fe$_{1-x-y}$Co$_x$Mn$_y$)$_2$As$_2$. N is the number of points measured in each batch, x$_{WDS}$ and y_{WDS} are the average values for that batch, and 2σ is twice the standard deviation of the N values measured.
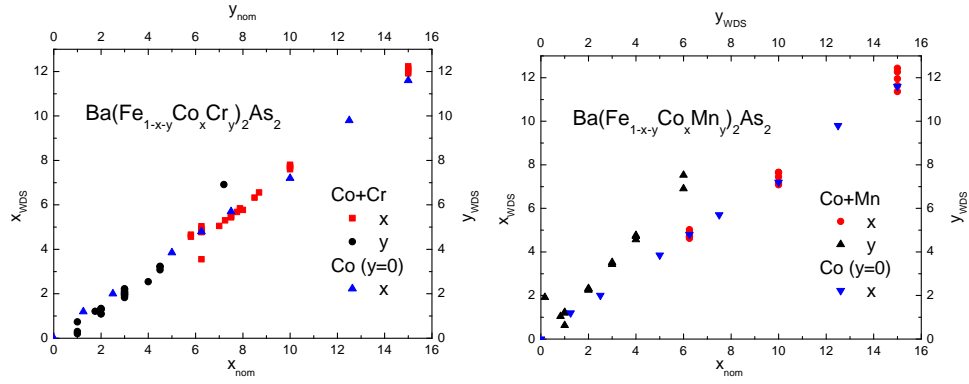
Figure 7.1: Real vs nominal Co, Cr and Mn concentrations for singly-substituted Co ($y = 0$) and doubly-substituted Co+TM (TM=Cr or Mn).
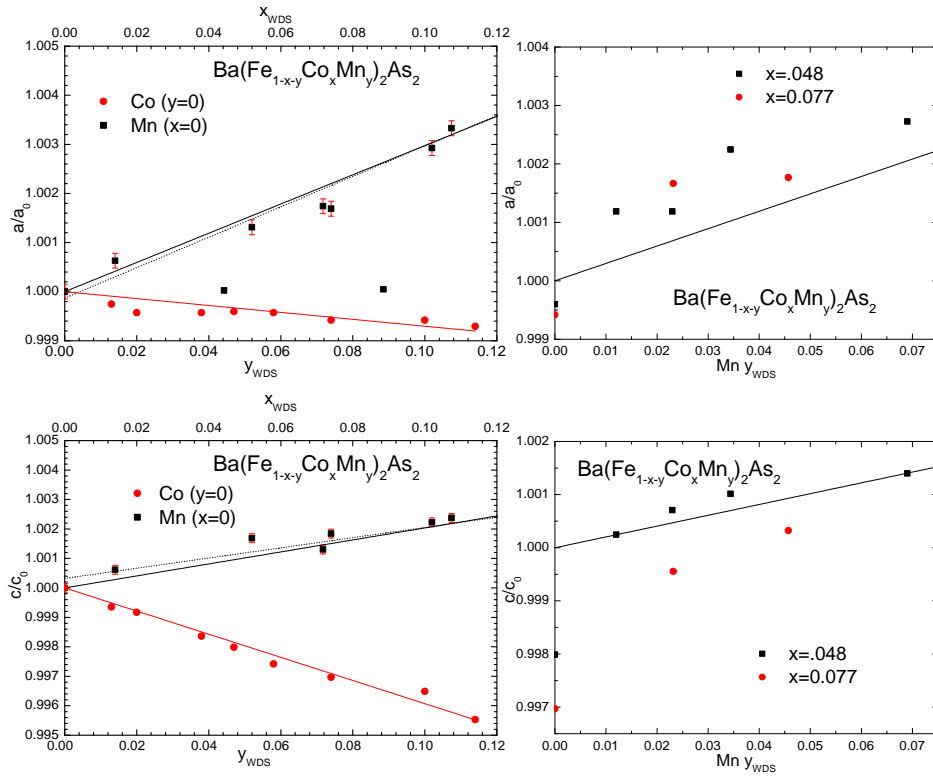
Figure 7.2: Unit cell parameters, a and c for Mn and Co alone (left) and Mn+Co (right), normalized to those of the parent compound $BaFe_2As_2$, for which $a_0 = 3.96$ Å and $c_0 = 13.0$ Å. The lines on the left are linear fits, used to calculate the open points on the right, and the black line on the right is the same as the one on the left.
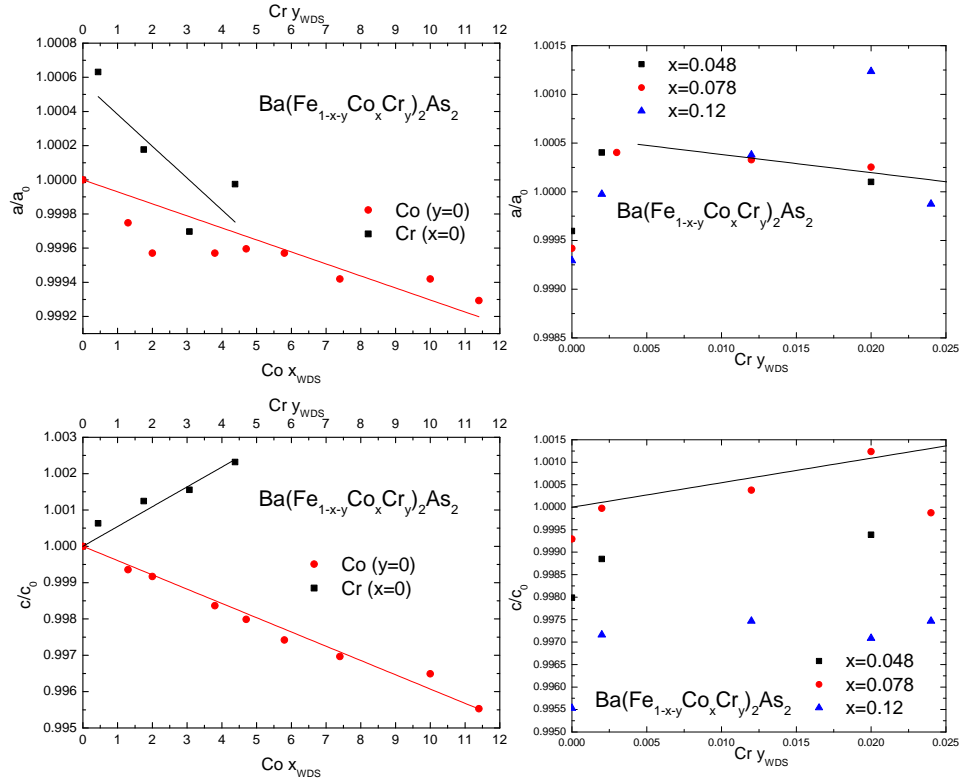
Figure 7.3: Unit cell parameters, a and c for Cr and Co alone (left) and Cr+Co (right), normalized to those of the parent compound BaFe$_2$As$_2$, for which $a_0 = 3.96$ Å and $c_0 = 13.0$ Å. The lines on the left are linear fits, used to calculate the open points on the right, and the black line on the right is the same as the one on the left.

Rietvelt refinement of powder x-ray patterns using Si as a standard allows lattice param-eters to be determined, from which unit cell volumes can be calculated. Normalized lattice parameters and unit cell volumes are displayed in Fig. 7.2 and Fig. 7.3. While the combined effect of Mn and Co on the lattice parameters is consistent with what is predicted from the single Mn and Co substitutions at least in terms of the slope, the combination of Cr and Co is less so. However, the measured values in the combined Cr and Co system follow a much more predictable trend than what is predicted from the Cr substitution alone (especially in the a parameter, Sefat et al. (2009b)), so this is likely the source of the error. Additionally, the slope of the a parameter is very small in the region of interest (as seen by the black line in Fig. 7.3), which is borne out by the $x = 0.048$ and $x = 0.078$ data. The $x = 0.12$ data does not follow the trend as well, but it is also much less consistent in general, so this is not totally unexpected.
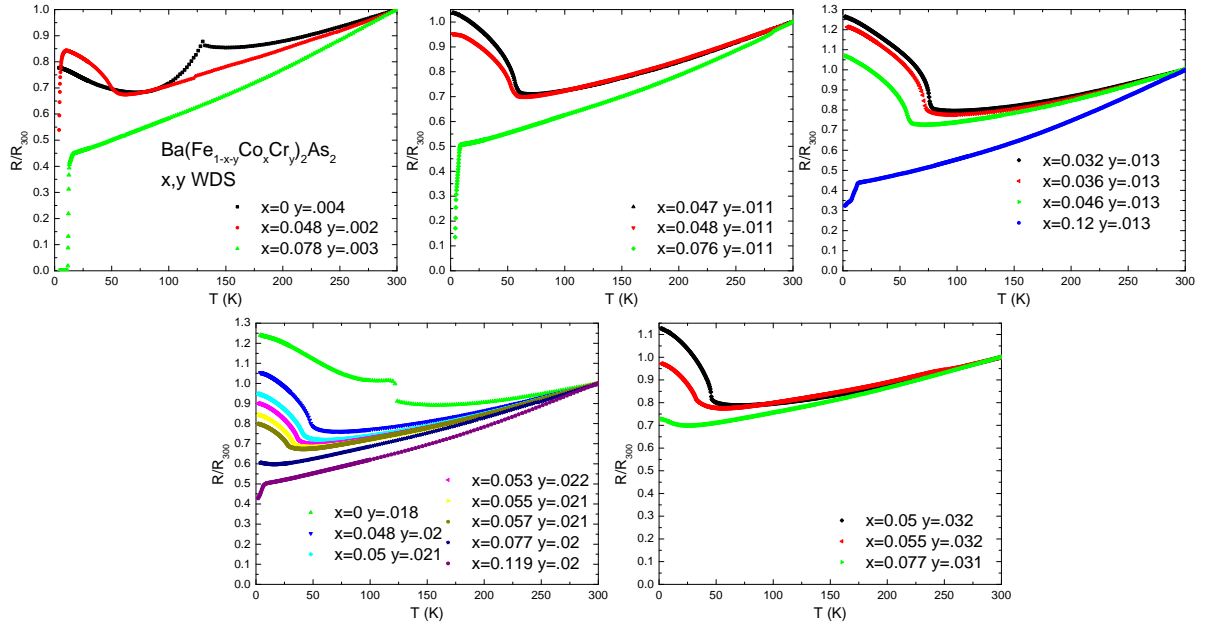
Figure 7.4: Temperature dependent resistivity, normalized to the room temperature value, for Ba(Fe$_{1-x-y}$Co$_x$Cr$_y$)$_2$As$_2$.
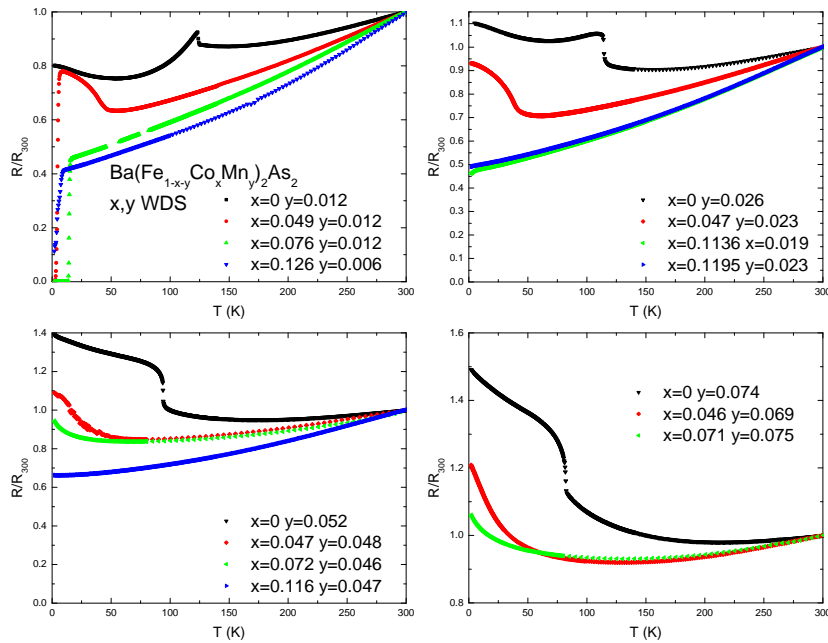
Figure 7.5: Temperature dependent resistivity, normalized to the room temperature value, for Ba(Fe$_{1-x-y}$Co$_x$Mn$_y$)$_2$As$_2$.
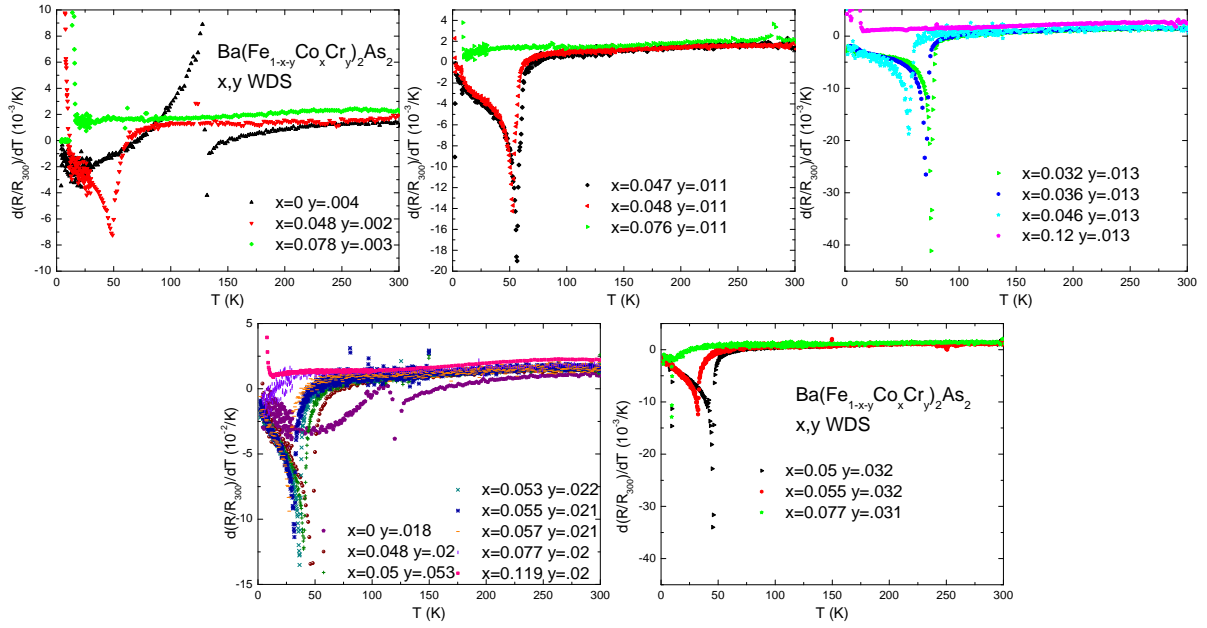
Figure 7.6: First derivative of normalized resistivity for Ba(Fe$_{1-x-y}$Co$_x$Cr$_y$)$_2$As$_2$.
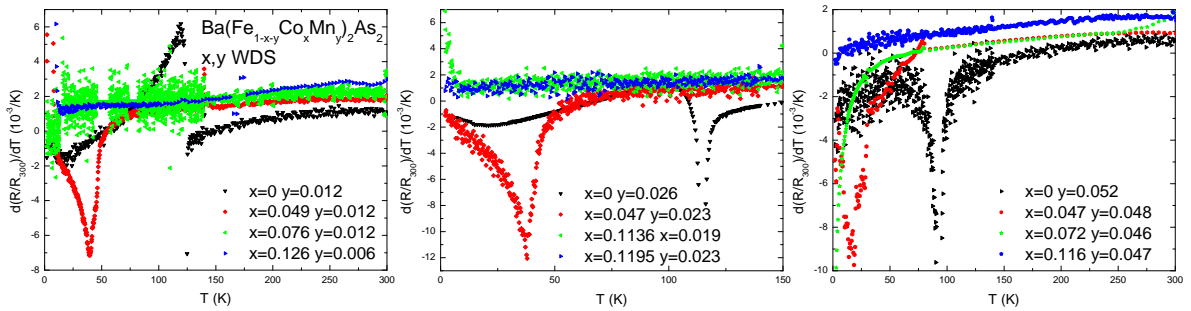
Figure 7.7: First derivative of normalized resistivity for Ba(Fe$_{1-x-y}$Co$_x$Mn$_y$)$_2$As$_2$.
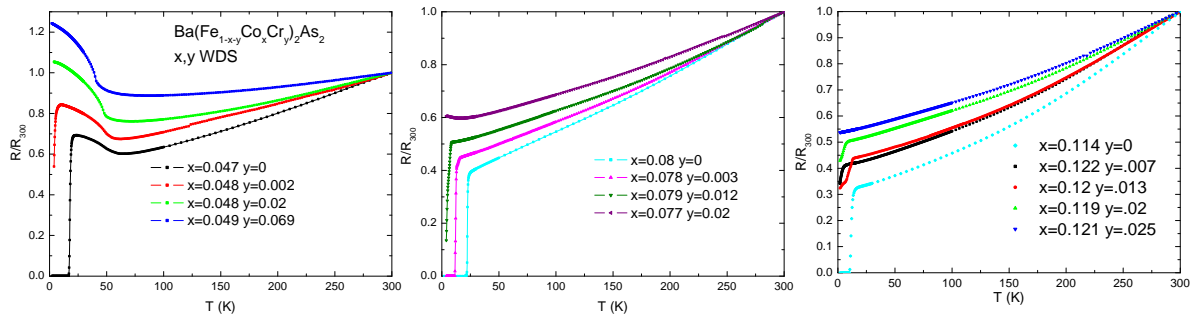
Figure 7.8: Temperature dependent resistivity, normalized to the room temperature value, for Ba(Fe$_{1-x-y}$Co$_x$Cr$_y$)$_2$As$_2$.
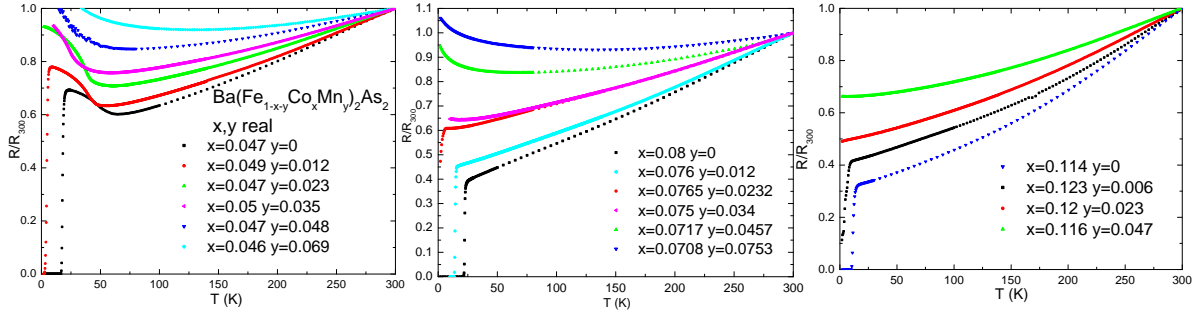
Figure 7.9: Temperature dependent resistivity, normalized to the room temperature value, for $Ba(Fe_{1-x-y}Co_xCr_y)_2As_2$.

Figures 7.4 and 7.5 show the normalized electrical resistivity data of the $Ba(Fe_{1-x-y}Co_xTM_y)_2As_2$ series from 2 K to 300 K. Normalized resistivity is plotted instead of resistivity because of the tendency of these samples to exfoliate or crack. (Ni et al. (2008b); Tanatar et al. (2009a,b)) The anomaly in resistivity at 134 K for pure $BaFe_2As_2$ is associated with the structural/magnetic phase transitions (Rotter et al. (2008b)), and can clearly be seen in the derivative of the resistivity (Ni et al. (2008b)), which is shown in Figs. 7.6 and 7.7. As in the case of single TM substitutions (Ni et al. (2008b); Canfield et al. (2009); Ni et al. (2009); Canfield and Bud'ko (2010)), double substitition suppresses the temperature of the resistive anomaly and changes the shape from a sharp decrease to a broadened increase as x+y increases.

One feature of note in the resistance series is a general trend towards a steeper slope $(\Delta(R/R_{300})/\Delta T)$ for higher Co x for a given Mn or Cr y. This is the opposite of the trend seen the other way around: for a given x, higher y gives a more shallow slope, as seen in Figs. 7.8 and 7.9. This is consistent with the trends seen in Co and Mn single substitutions: higher Co concentration tends to give a steeper slope (Ni et al. (2008b)), whereas higher Mn concentration tends to give shallower slope (Thaler et al. (2011)). However, it is contrary to the results seen when Cr is substituted by itself, where higher Cr concentration tends to give a steeper slope (Sefat et al. (2009b)).
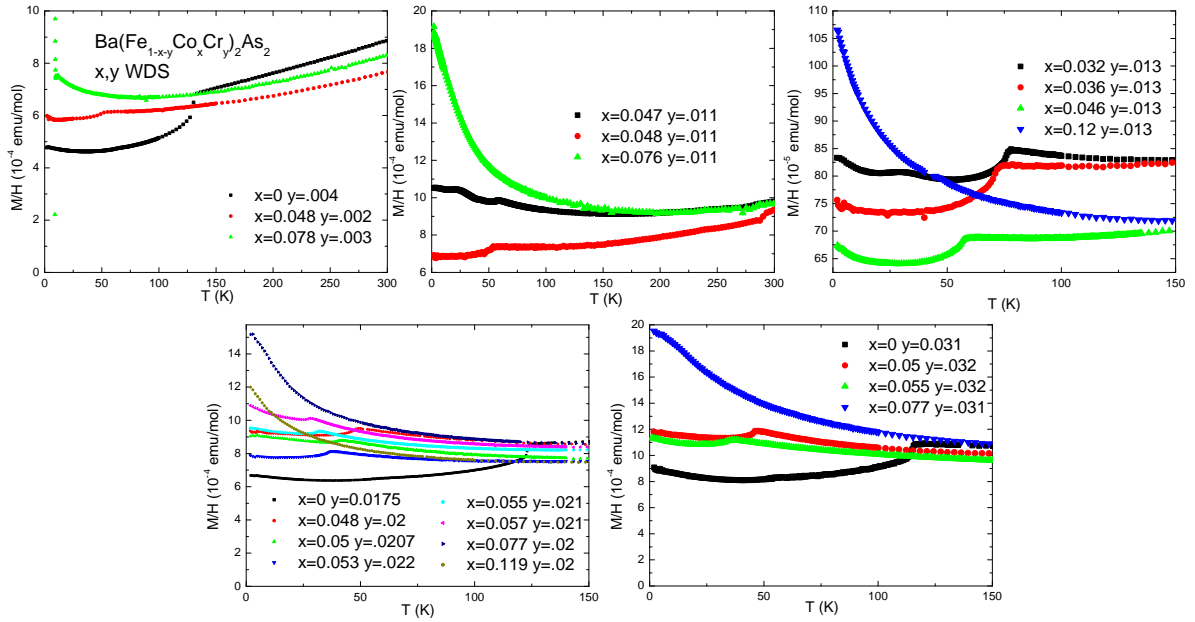
Figure 7.10: Temperature dependent magnetization for $Ba(Fe_{1-x-y}Co_2Cr_y)_2As_2$ with $H||ab$. In all cases, $H = 55\ kOe$.

Figure 7.11: Temperature dependent magnetization for $Ba(Fe_{1-x-y}Co_2Mn_y)_2As_2$ with $H||ab$. In all cases, $H = 55\ kOe$.

Figure 7.12: Derivatives of the temperature dependent magnetization for $Ba(Fe_{1-x-y}Co_xCr_y)_2As_2$ with $H||ab$. In all cases, $H = 55 \ kOe$.
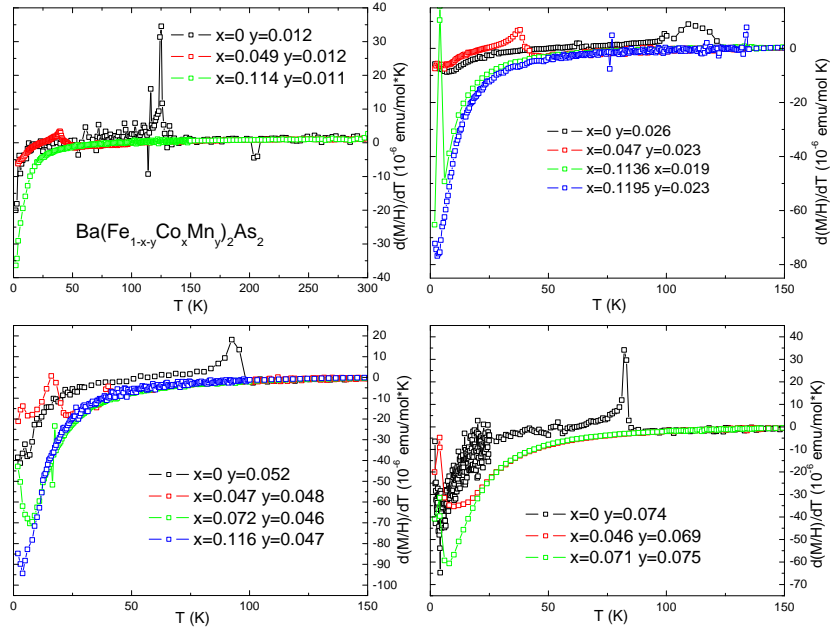
Figure 7.13: Derivatives of the temperature dependent magnetization for $\mathrm{Ba(Fe_{1-x-y}Co_xMn_y)_2As_2}$ with $H||ab$. In all cases, $H = 55\ kOe$.

Signatures of the structural/magnetic phase transition in the lower substitution region are also seen in magnetization data: Figs. 7.10 and 7.11 show temperature dependent magnetization data of the $\mathrm{Ba(Fe_{1-x-y}Co_xTM_y)_2As_2}$ series from 2 K to 300 K and Figs. 7.12 and 7.13 show the derivatives of the temperature dependent magnetization data.

Figures 7.14 and 7.15 show the field dependent magnetization ($H||ab$) of the $\mathrm{Ba(Fe_{1-x-y}Co_xTM_y)_2As_2}$ series at 2 K. These data show that as Co levels are increased for a given Cr or Mn concentration, the M/H (susceptibility) increases, as seen in $M(T)/H$ data presented in Figs. 7.10 and 7.11. This is consistent with the increasing Curie-Weiss like tail that appears for larger $x + y$ values once $T_{s,m}$ is fully suppressed.

7.4 Discussion

As shown in Fig. 7.16, T-x phase diagrams for the $\mathrm{Ba(Fe_{1-x-y}Co_xTM_y)_2As_2}$ (TM=Cr, Mn) systems have been constructed by applying the same criteria as in our single substitution work (see Chapters 5 and 6) to the data from each member of the substituted series. Substitution
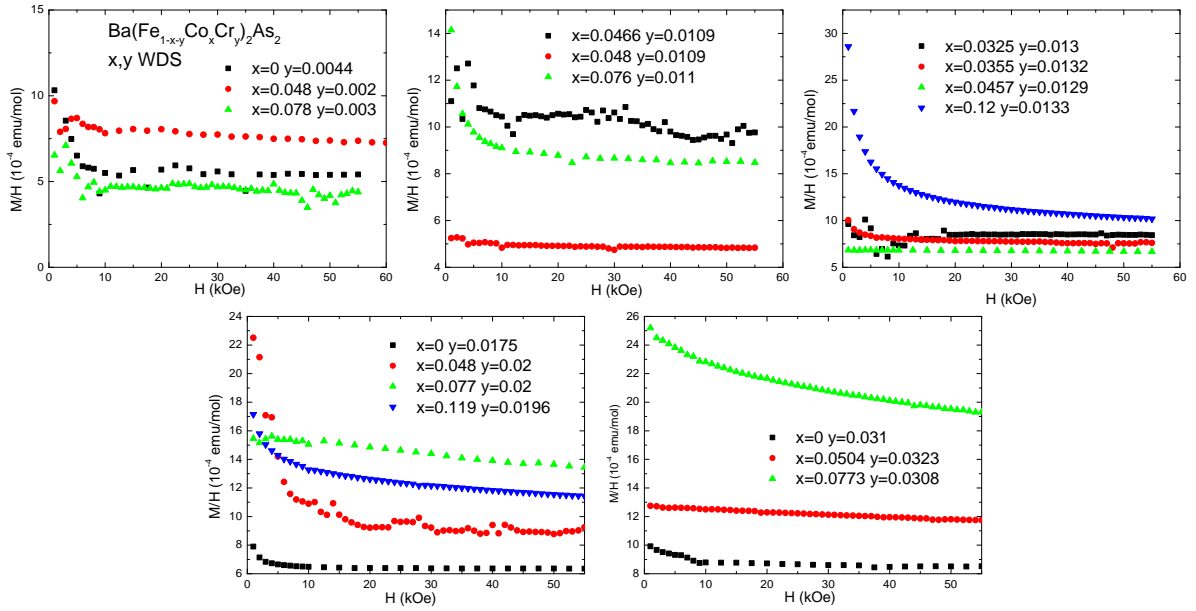
Figure 7.14: Field dependent magnetization for $\mathrm{Ba(Fe_{1-x-y}Co_xCr_y)_2As_2}$, $H||ab$. In all cases, $T = 2K$.
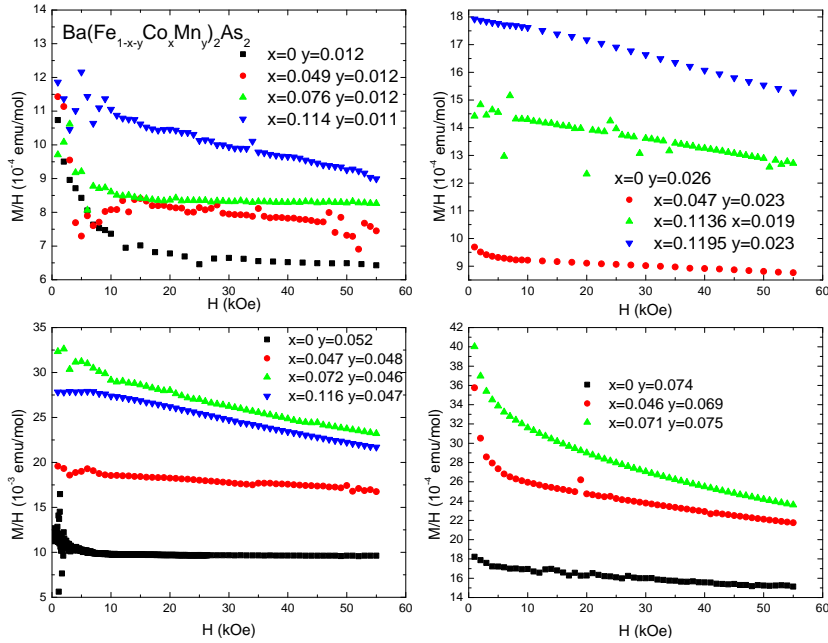
Figure 7.15: Field dependent magnetization for $\mathrm{Ba(Fe_{1-x-y}Co_xMn_y)_2As_2}$, $H||ab$. In all cases, $T = 2K$.
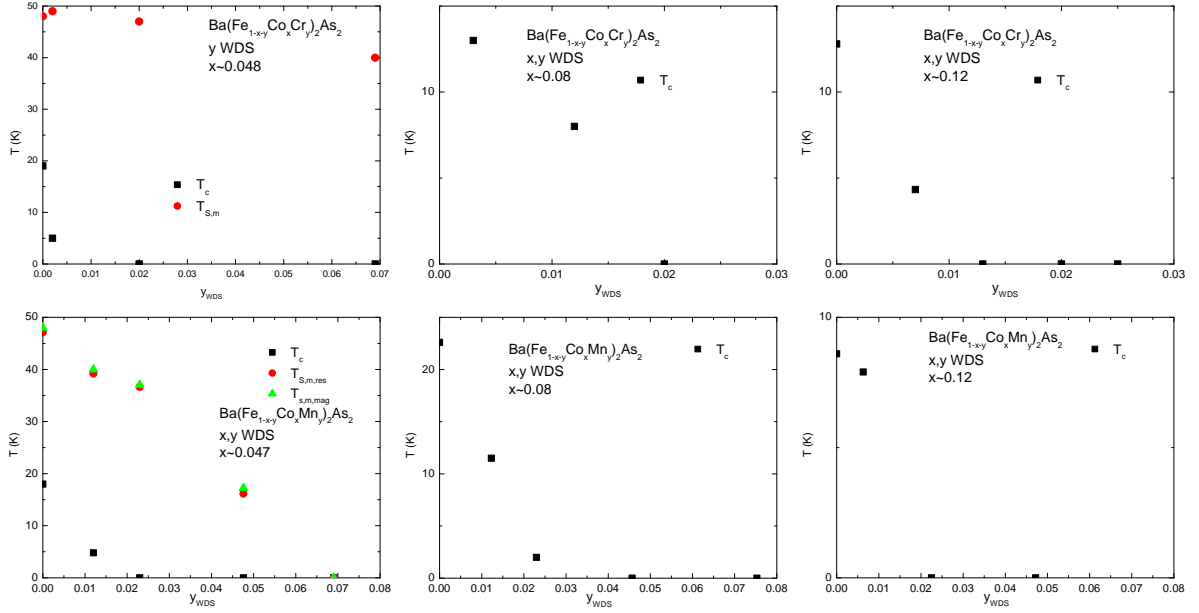
Figure 7.16: Substitution level dependent phase diagrams for $Ba(Fe_{1-x-y}Co_x TM_y)_2As_2$ (TM=Cr, Mn).

of any of the three transition metals for Fe suppresses the high temperature tetragonal to orthorhombic and antiferromagnetic phase transition (Ni et al. (2008b); Sefat et al. (2009b); Thaler et al. (2011)). Adding Cr or Mn to a Co substituted sample further suppresses these transitions.

As discussed above, part of the motivation for this study was to see if Cr and Mn can be treated as some form of hole-donor for the purposes of substitution. If so, it should be possible to 'walk' back and forth along the superconducting dome by first substituting Co then adding either Cr or Mn. If the Cr or Mn contribute hole-like carriers, then substitution of Mn should act the same as removing the same amount of Co as added Mn and substitution of Cr should act the same as removing twice as much Co as added Cr. This is not what is observed, as shown in Figs. 7.15 and 7.17.

Instead of behaving as if it were removing electrons from the system, the addition of Cr or Mn suppresses both the high temperature structural phase transition and the superconducting transition for all Co concentrations. If Cr or Mn were acting as hole donors, then we would expect that the structural transition temperature (T_s) would increase rather than decrease,
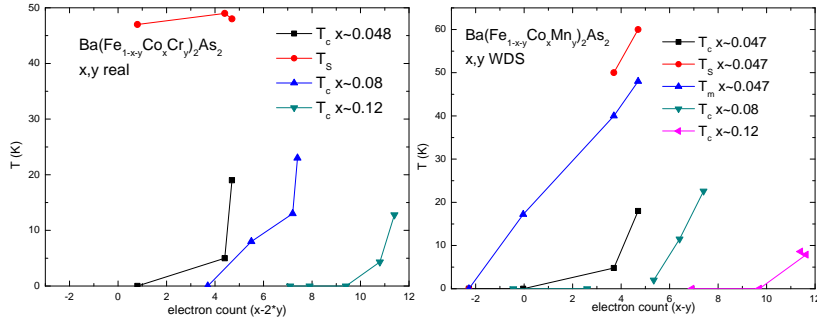
Figure 7.17: Electron count dependent phase diagrams for Ba(Fe$_{1-x-y}$Co$_x$TM$_y$)$_2$As$_2$ (TM=Cr, Mn).

and we might also expect to see reemergence of the structural transition in samples with more Co than optimal, where the transition has been suppressed completely. While we would expect to see suppression of T_c when adding Cr or Mn to Co concentrations below optimal – moving lower on the electron count phase diagram – our observation is that T_c is suppressed even in samples where the Co concentration is well above optimal, where we should see an increase in T_c in the case of simple band filling. Furthermore, we see that the rate of suppression of T_c is very nearly the same independent of the Co concentration.

7.5 Summary

Single crystals of Ba(Fe$_{1-x-y}$Co$_x$TM$_y$)$_2$As$_2$ (TM=Cr,Mn) have been grown out of a TMAs flux for various x and y values up to $x \sim 0.12$ and $y \sim 0.04$. Samples are homogeneous and single phase and are size limited by the growth crucible. Cr and Mn appear to preferentially substitute for Fe, rather than competing with the Co, allowing relatively easy prediction of x_{WDS} and y_{WDS} from $x_{nominal}$ and $y_{nominal}$ using the single substitution values measured and tabulated previously. For all x values, increasing y suppresses $T_{s,m}$ as well as T_c for x values which superconduct when prepared with $y = 0$. These results are inconsistent with either Cr or Mn acting as simple hole donors.

CHAPTER 8.   Effects of annealing on $Ba(Fe_{0.88-y}Co_{0.12}Cr_y)_2As_2$ $(y=0,\ 0.013)$

8.1   Motivation

When discussing multiple TM substitutions onto the Fe site of $BaFe_2As_2$, I noted that superconductivity is rapidly suppressed by the addition of even a small amount of Cr to a sample with a Co substitution which would, by itself, induce superconductivity, and that that this is still the case even in samples with optimal or over substituted Co, where superconductivity is quite robust (see Chapter 7). However, when measuring heavily over-substituted Co with additional Cr, one sample $(Ba(Fe_{0.867}Cr_{0.013}Co_{0.12})_2As_2)$ showed a trace of partial superconductivity in resistive measurements (see Fig. 8.1).

Strain can radically alter the properties of some members of this system and its relatives, and post-growth annealing has been shown to be effective in removing some of the effects of this strain, restoring the properties of the unstressed parent compound (Saha et al. (2009); Ran et al. (2011). With that in mind, it seemed likely that the partial superconductivity seen in this sample was a result of strain of some kind – either in growth, extraction from the melt or attaching the resistance wires – so we decided to attempt to remove the effect through annealing. We sealed the resistance sample as prepared – with wires still attached – in a SiO_2 tube and annealed for $\sim$120 hours at 600° C, then remeasured it. Instead of the expected restoration of normal metallic behavior, the sample displayed full, zero-resistance superconductivity with $T_{c,onset}$ increased from $\sim$13 K to $\sim$26 K. In order to better understand this phenomenon, we began a systematic study of the effects of annealing on TM substituted $BaFe_2As_2$, both with Co alone and with Cr added.
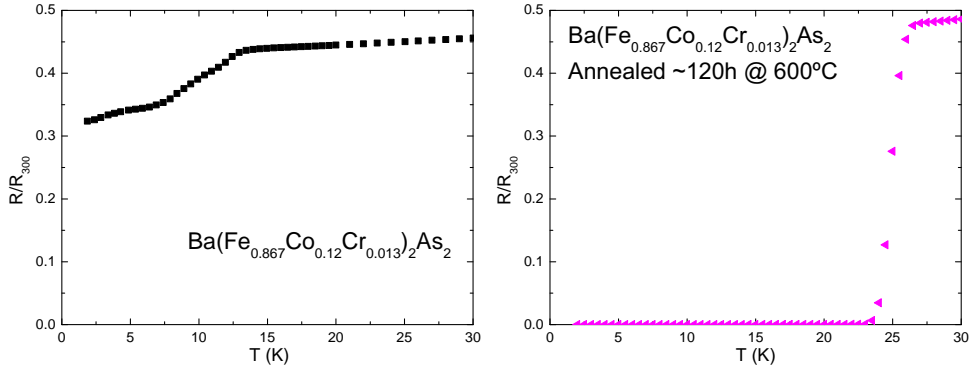
Figure 8.1: Left: normalized resistance of as-grown $Ba(Fe_{0.867}Cr_{0.013}Co_{0.12})_2As_2$ showing a drop in resistance characteristic of partial filamentary superconductivity at approximately 13 K. Right: normalized resistance of the same resistance bar, annealed for $\sim$120 hours at 600°C, showing zero resistance starting at at approximately 23 K.

8.2 Sample Preparation

Samples were prepared in a manner identical to that described in Chapters 3, 4, and 7. Annealing was performed in two slightly different ways. Initially, samples were grown, measured then resealed in SiO_2 tubes and annealed. This allowed us to measure the properties of a particular batch or sample both before and after annealing. Because we did not want to attach wires to the sample – since the Ag epoxy might react with the sample during annealing – we did not, in general, measure the particular crystals being considered prior to annealing but limited ourselves to representatives from the same batch. Because we had concerns about exposure to oxygen, later batches were synthesized as usual, but then annealed in their growth tubes prior to opening. This provided us with samples which were not exposed to atmosphere prior to annealing. Although this latter method should have provided better controlled samples, it had some complexities associated with it that will be discussed below.

8.3 Results

Before diving into a discussion of the data presented in this chapter, I want to comment that this data is somewhat preliminary. It was only discovered late in the progress of the work discussed in Chapter 7. It provided many challenges and surprises, and I did not have

time to fully explore what was happening or correct initial measurements which may have had problems in the data collection. Please take the results presented here with a grain of salt and refer to any subsequent work on the subject for clarification.

Figures 8.2(a) and (c) show normalized, low-temperature resistance for annealed samples of $Ba(Fe_{1-x-y}Co_xCr_y)_2As_2$ annealed at 600°C. These were all from one batch, with the crystals individually annealed after opening. The Co concentration is well above what it should be for optimal T_c. As discussed in Chapter 7, the $\sim 1.3\%$ Cr added in the doubly-substituted compound should destroy the superconductivity normally seen at this Co concentration. Instead, as discussed above, T_c monotonically increases up to six days of annealing, though it is essentially at its maximum value after four days, with max T_c roughly 26 K. Further annealing does not appear to significantly increase T_c, but neither does it decrease it. Fig. 8.2(c) shows the first of the questionable data presented here: the four-day annealed sample shows a sharp decrease in resistance at approximately the temperature we expect for the superconducting transition (based upon the other anneals), but does not reach zero resistance. This is most likely not a real effect, and probably results from bad electrical contacts.

Figures 8.2(b) and (d) show temperature dependent superconducting fraction data for $Ba(Fe_{1-x-y}Co_xCr_y)_2As_2$ annealed at 600°C. Only field cooled data is shown, but T_c is still easily detectable. In fact, it is higher in the doubly-substituted sample post-annealing than it is in the equivalent Co-only sample (see below). However, it is several Kelvins lower than what is seen in resistance. The transition width is also quite wide: approximately 8 K even in the best case. In Fig. 8.2(b), the data shows multiple problems. The five day anneal has a positive uptick in superconducting fraction, then a sharp transition to a well-behaved decrease, indicating increasing superconducting fraction below this sharp feature. Because the positive signal is essentially the opposite of what we expect ($-1\times$ the expected signal), this is probably a result of loss of centering by the MPMS. The one day and 6.5 day anneals show a different problem: much larger superconducting fraction than is possible. Because these measurements were made with $H||ab$, we do not expect geometric demagnetization factor to be a major contributor to discrepancies in the superconducting fraction measurement. The data for these two sets was taken in the same MPMS system as the other three annealing times and the other
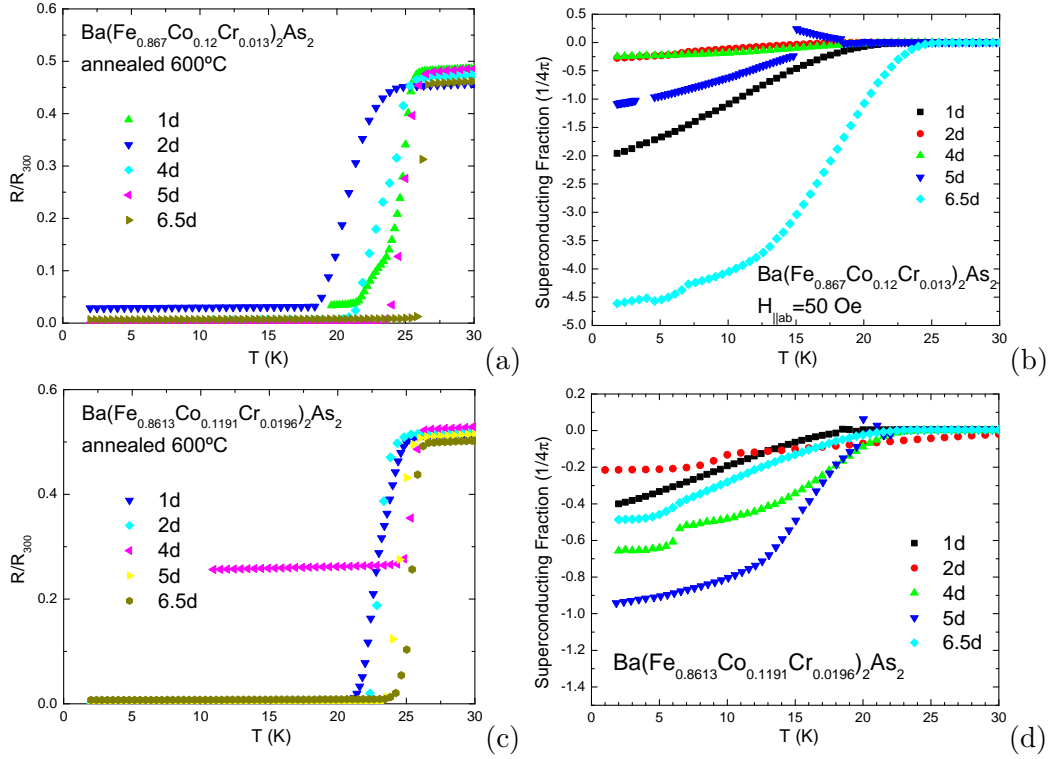
Figure 8.2: Temperature dependent normalized resistance $R(T)/R_{300\,\mathrm{K}}$ (a,c) and superconducting fraction (b,d) for Ba(Fe$_{1-x-y}$Co$_x$Cr$_y$)$_2$As$_2$, annealed for varying lengths of time. In these figures, the samples were annealed after opening the growth tube, and were annealed at 600° C.
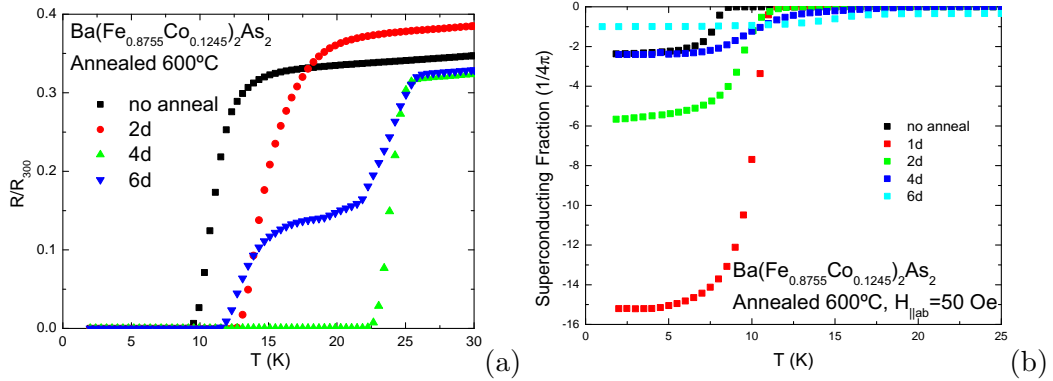
Figure 8.3: Temperature dependent normalized resistance $R(T)/R_{300\,\mathrm{K}}$ (a) and superconducting fraction (b) for Ba(Fe$_{1-x}$Co$_x$)$_2$As$_2$, annealed for varying lengths of time. These samples were annealed post-opening.

samples (such as what is shown in Fig. 8.2(d)) using an identical measurement sequence, which included a demagnetization sequence at the beginning (as described in Section 3.2.4), so it is not clear what the source of this error is. One possibility is that there was a problem with the SQUID calibration which only manifested in these two data sets, but we have not looked for evidence of this.

Figure 8.3(a) shows normalized, low-temperature resistance for annealed samples of $Ba(Fe_{1-x}Co_x)_2As_2$ annealed at $600°C$. These samples were separate parallel batches annealed prior to opening. Co concentration is well above what it should be for optimal T_c. Here, T_c is increased from ~ 10 K in the as-grown sample to ~ 26 K in the four-day anneal. The transition is also significantly sharpened. In the six-day anneal, the transition splits into one at ~ 26 K and another at ~ 15 K, though it is not clear whether this is an effect of the heat treatment or a problem with this sample batch.

Figure 8.3(b) shows temperature dependent superconducting fraction data for $Ba(Fe_{1-x}Co_x)_2As_2$ annealed at $600°C$. Only field cooled data is shown here. Unfortunately, T_c is significantly lower as measured by magnetization than by resistance. In fact, it is nearly unchanged from the as-grown result. This result suggests that the extreme increase in T_c seen in resistance is merely a surface or filamentary effect. As with the data shown in Fig. 8.2(b), the superconducting fraction data shown here has a problem with being somewhat over-exuberant. The usual explanations, geometric demag. factor and remnant field, can be discounted here for the same reasons as described for the double-substituted sample.

Figure 8.4 shows temperature dependent superconducting fraction data for $Ba(Fe_{1-x}Co_x)_2As_2$. These samples were annealed prior to opening the growth tube, and additions to the temperature profile were made: one at $800°C$ and $1000°C$, both after 8 days of annealing at $600°C$. In the $800°C$ case, superconductivity is dramatically suppressed, down to only 20% superconducting fraction and a T_c of only ~ 8 K. The $1000°C$ annealed sample has superconductivity suppressed down to zero. These data imply that if there are any improvements to be gained by annealing, these temperatures and times were too high or long to realize them. One thing to note is that this data does not have the problem with unphysical superconducting fractions that the post-opening anneal samples shown in Fig. 8.3 display. It is not clear why that is.
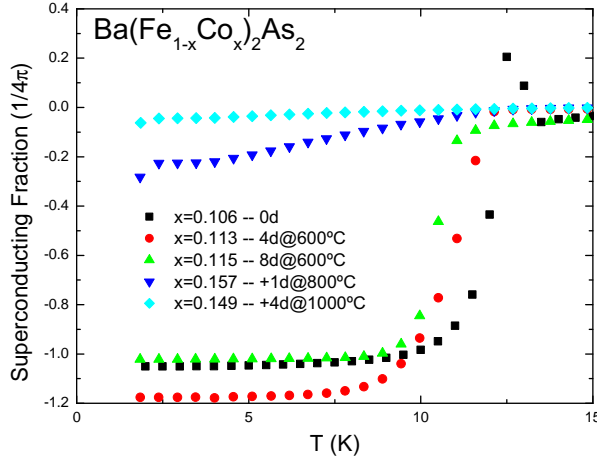
Figure 8.4: Temperature dependent superconducting fraction for Ba(Fe$_{1-x}$Co$_x$)$_2$As$_2$, annealed for varying lengths of time and at varying temperatures. These samples were annealed prior to opening the growth tube.

8.4   Discussion and Future Work

Although annealing the growths prior to opening their amorphous silica tubes allowed us to eliminate exposure to air as a possible culprit in the odd behavior of this system, it did present some issues. First and foremost, batch to batch variation in x could not be eliminated, which makes comparing the same substitution level annealed for differing lengths of time difficult at best. This variation between batches is unfortunately large enough in some cases to make the predicted T_c significantly different, even without considering the effect of annealing: for $x = 0.106$ (the value for the batch which was not annealed), $T_c \approx 14.7\,K$ – higher than what is seen here– while for $x = 0.115$ (the eight day anneal), $T_c \approx 10.8\,K$.

The other, related problem with annealing the samples prior to opening is that they could not be measured prior to annealing. Resistive and magnetic measurements as well as elemental analysis would useful information about the state of the samples before and after annealing. The two batches annealed at higher temperatures both show variation in x. This variation may be coincidence, but it is also possible that the annealing is altering the substitution level. If this is the case in the singly Co-substituted samples, it is possible that is is also what is happening in the doubly-substituted, Ba(Fe$_{1-x-y}$Co$_x$Cr$_y$)$_2$As$_2$ ones. If that is what is happening, then it may
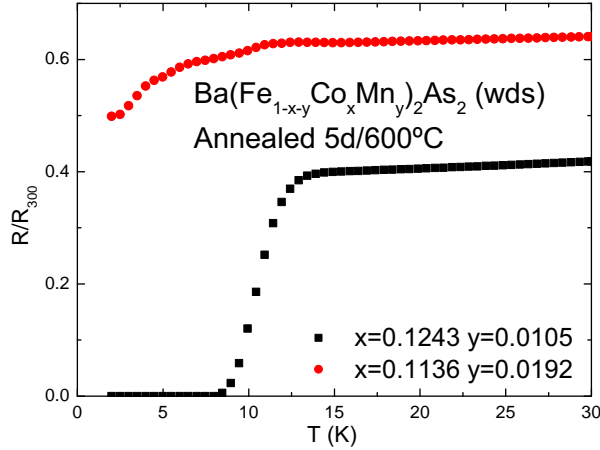
Figure 8.5: Temperature dependent resistivity, normalized to the room temperature value, for Ba(Fe$_{1-x-y}$Co$_x$Mn$_y$)$_2$As$_2$ annealed for 5 days at 600°C. These samples were annealed after opening the growth tube.

not be an annealing issue at all, but simply that heat treatment removes Cr from the lattice. In that case, the reduced Cr concentration might be enough to restore superconductivity.

Any future work should begin with elemental analysis performed both before and after annealing. That would give a clearer idea of whether heat treatment changes the stoichiometry of the samples (at least on the surface) or introduces impurities from the atmosphere, such as oxygen. Another thing to explore is a more detailed study of different Co concentrations. So far, I have only looked at ∼7% Co and ∼12% Co, and only the latter in detail. Annealing studies on under-substituted samples should be considered as well to see how heat treatment affects $T_{s,m}$. Other temperature profiles – lower temperature for example – should be explored as well. Finally, other TM substitutions should be measured. Preliminary data on Ba(Fe$_{1-x-y}$Co$_x$Mn$_y$)$_2$As$_2$ show that it behaves similarly, but not identically, to Ba(Fe$_{1-x-y}$Co$_x$Cr$_y$)$_2$As$_2$ when annealed. As shown in Figure 8.5, annealing restores superconductivity to this system as well, but T_c is considerably lower for comparable substitution level and annealing time.

8.5 Summary

Samples of $Ba(Fe_{1-x}Co_x)_2As_2$ and $Ba(Fe_{1-x-y}Co_xCr_y)_2As_2$ have been prepared and heat treated. We find that heat treatment alters the superconducting properties of both series and that $T_{c,max}$ is nearly identical in both cases. Unfortunately, the effect appears to be filamentary or surface only in the case of $Ba(Fe_{1-x}Co_x)_2As_2$, and appear to be significantly different in the bulk than on the surface in $Ba(Fe_{1-x-y}Co_xCr_y)_2As_2$, as demonstrated by the difference between resistive and magnetization measurements.

CHAPTER 9.   Collaborations Based on the Use of

$Ba(Fe_{1-x}TM_x)_2As_2$ Single Crystals

Much of my time during my graduate work was spent preparing samples requested by others for more detailed or specialized measurements than I could perform myself. These growth requests were normally motivated by work done within our group, so I usually had some experience with the system of interest. This allowed me to assess what would be needed and to provide samples with the requested specifications (eg. sample size or substitution level). An example of this is shown in Fig. 9.1.
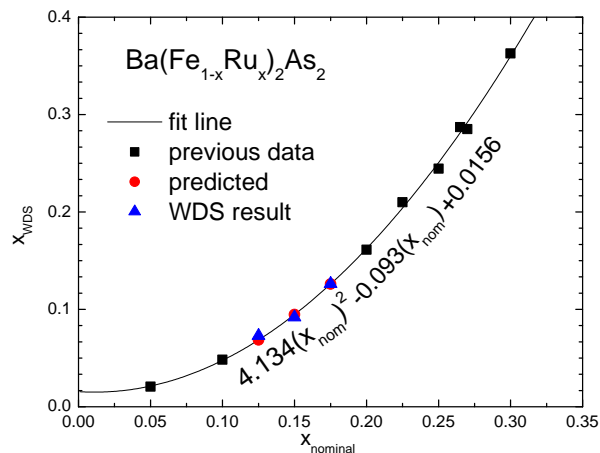
Figure 9.1: Example of how previously grown samples were used to provide samples with requested x values. Black squares are the data before the new growths were made, the black line is a fit to these data and the red circles are the prediction of what three nominal values would give for real x_{Ru}. The blue triangles are the WDS values of these three growths, showing excellent agreement between the prediction and the result.

Some scattering measurements required sample masses far in excess of what could be provided by any one single crystal. For these measurements, a large number of samples with as close to identical composition as possible needed to be synthesized and co-aligned. Two minor

modifications were made to the growth techniques in order to help facilitate meeting this requirement. First, 5 ml alumina growth crucibles were used instead of the standard 2 ml ones. These provide more than twice the volume for crystal growth, which allows much larger single crystals to form during synthesis. Second, multiple identical batches were prepared and grown at the same time under identical conditions. In order to minimize the possibility of batch to batch variation, the TMAs and FeAs powders for all of these batches were mixed together at once to attempt to ensure that each batch had the same proportion of TM:Fe. This large amount of mixed powder was then separated into parts suitable for each batch and combined with Ba in the manner described in Chapter 3.

Presented below are summaries of some of the data taken on samples I prepared for collaborative efforts with other groups.

9.1 X-Ray Scattering

Nandi et al. (2010) described high resolution x-ray diffraction measurements, which revealed an unusually strong response of the lattice to superconductivity in $Ba(Fe_{1-x}Co_x)_2As_2$. The orthohrombic distortion of the lattice is suppressed below T_c and, for Co substitution levels near $x = 0.063$, the orthorhombic structure evolves smoothly back to a tetragonal structure. The authors proposed that the coupling between orthorhombicity and superconductivity is indirect and arises due to the magnetoelastic coupling, in the form of emergent nematic order, and the strong competition between magnetism and superconductivity.

Kim et al. (2010a) gave the results of resonant x-ray diffraction measurements at the Fe K edge of both the parent $BaFe_2As_2$ and superconducting $x = 0.047$ compounds. The authors concluded, from these high-resolution measurements, that the magnetic structure is commensurate for both compositions. The energy spectrum of the resonant scattering was in reasonable agreement with theoretical calculations using the full-potential linear augmented plane-wave method with a local density functional.

Neutron and x-ray diffraction studies of $Ba(Fe_{1-x}Mn_x)_2As_2$ for $x \lesssim 0.176$ were performed in 2010 and are described in Kim et al. (2010b). These revealed that at a critical concentration, $0.102 < x < 0.118$, the tetragonal-to-orthorhombic transition abruptly disappears whereas

magnetic ordering with a propagation vector of (1/2 1/2 1) persists. Among all of the iron arsenides this observation is unique to Mn substitution, and unexpected because all models for "stripe-like" antiferromagnetic order anticipate an attendant orthorhombic distortion due to magnetoelastic effects. They discussed these observations and their consequences in terms of previous studies of $Ba(Fe_{1-x}TM_x)_2As_2$ compounds (TM=transitionmetal), and models for magnetic ordering in the iron arsenide compounds.

Kim et al. (2011a) presented a combined high-resolution x-ray diffraction and x-ray resonant magnetic scattering study of as-grown BaFe2As2. The structural and magnetic transitions must be described as a two-step process. At $T_S = 134.5$ K, they observed the onset of a second-order structural transition from the high-temperature paramagnetic tetragonal structure to a paramagnetic orthorhombic phase, followed by a discontinuous step in the structural order parameter that is coincident with a first-order antiferromagnetic (AFM) transition at $T_N = 133.75$ K. These data, together with detailed, high-resolution x-ray studies of the structural transition in lightly substituted $Ba(Fe_{1-x}Co_x)_2As_2$ and $Ba(Fe_{1-x}Rh_x)_2As_2$ compounds, showed that the structural and AFM transitions do, in fact, occur at slightly different temperatures in the parent $BaFe_2As_2$ compound, and evolve toward split second-order transitions as the substitution level is increased. They estimated the composition for the tricritical point for Co substitution and employ a mean-field approach to show that these measurements can be explained by the inclusion of an anharmonic term in the elastic free energy and magnetoelastic coupling in the form of an emergent Ising-nematic degree of freedom.

Dean et al. (2012) investigated the magnetic polarization of the Ir $5d$ substitutant states in superconducting $Ba(Fe_{1-x}Ir_x)_2As_2$ (with $x = 0.027(2)$) using Ir L_3 edge x-ray resonant magnetic scattering (XRMS). Despite the fact that substitution partially suppresses the antiferromagnetic transition, they found that magnetic order survives around the Ir substitutant sites. The Ir states are magnetically polarized with commensurate stripe-like antiferromagnetic order and long correlations lengths, $\xi_{mag} > 2800$ and > 850Å, in the ab plane and along the c axis, respectively, driven by their interaction with the Fe spins. This Ir magnetic order persists up to the Néel transition of the majority Fe spins at $T_N = 74(2)$ K. At 5 K, the authors find that magnetic order coexists microscopically with superconductivity in $Ba(Fe_{1-x}Ir_x)_2As_2$.

The energy dependence of the XRMS through the Ir L_3 edge showed a non-Lorentzian line shape, which were explained in terms of interference between Ir resonant scattering and Fe nonresonant magnetic scattering.

9.2 Neutron Scattering

Neutron-diffraction and high-resolution x-ray diffraction studies found that, similar to the closely related under-substituted $Ba(Fe_{1-x}Co_x)_2As_2$ superconducting compounds, $Ba(Fe_{1-x}Rh_x)_2As_2$ ($x = 0.039$) showed strong evidence of competition and coexistence between superconductivity and antiferromagnetic order below the superconducting transition, $T_c = 14$ K. The transition temperatures for both the magnetic order and orthorhombic distortion were in excellent agreement with those inferred from resistivity measurements, and both order parameters manifest a distinct decrease in magnitude below T_c. These data suggest that the strong interaction between magnetism and superconductivity is a general feature of electron-carrier substituted $Ba(Fe_{1-x}TM_x)_2As_2$ superconductors (TM=transition metal). (Kreyssig et al. (2010))

Fernandes et al. (2010) showed the results, both theoretical and experimental, of using magnetic long-range order as a tool to probe the Cooper-pair wave function in the iron arsenide superconductors. They demonstrated that the theory shows that antiferromagnetism and superconductivity can coexist in these materials only if Cooper pairs form an unconventional, sign-changing state. This means that the observation of coexistence in $Ba(Fe_{1-x}Co_x)_2As_2$ demonstrates unconventional pairing in this material. The detailed agreement between theory and neutron-diffraction experiments, in particular, for the unusual behavior of the magnetic order below T_c, demonstrates the robustness of these conclusions, and strongly suggests that superconductivity is unconventional in all members of the iron arsenide family.

Pratt et al. (2010) showed results from inelastic neutron-scattering measurements performed on $Ba(Fe_{1-x}Co_x)_2As_2$ with $x = 0.047$, which is in the substitution range where superconductivity and long-range antiferromagnetic (AFM) order coexist. Here, the magnetic excitation spectrum found in the normal state is strongly damped and develops into a magnetic resonance feature below T_c that has appreciable dispersion along c axis with a bandwidth of 34 meV. This

is in contrast to the optimally substituted composition which has no long-range AFM order, and where the resonance exhibits a much weaker dispersion (Lumsden et al. (2009)). The results suggested that the resonance dispersion arises from interlayer spin correlations present in the AFM ordered state.

Kim et al. (2011b) presented a systematic investigation of the antiferromagnetic ordering and structural distortion for the series of $Ba(Fe_{1-x}Ru_x)_2As_2$ compounds ($0 \leq x \leq 0.246$). Neutron and x-ray diffraction measurements demonstrated that, in contrast with compounds containing TM substitutions which provide extra electrons (i.e. TM=Co, Ni, Cu, Rh, Pd, or Ir), the structural and magnetic transitions remained coincident in temperature. Both the magnetic and structural transitions are gradually suppressed with increased Ru concentration and coexist with superconductivity. For samples that are superconducting, the data suggested strong competition between superconductivity, the antiferromagnetic ordering, and the structural distortion.

Pratt et al. (2011) presented the results of neutron diffraction studies of $Ba(Fe_{1-x}Co_x)_2As_2$ which revealed that commensurate antiferromagnetic order gives way to incommensurate magnetic order for Co compositions between $0.056 < x < 0.06$. The incommensurability has the form of a small transverse splitting $(0, \pm\epsilon, 0)$ from the commensurate antiferromagnetic propagation vector $Q_{AFM} = (1, 0, 1)$ (in orthorhombic notation) where $\epsilon \approx 0.02 - 0.03$ and is composition dependent. These results were consistent with the formation of a spin-density wave driven by Fermi surface nesting of electron and hole pockets and confirm the itinerant nature of magnetism in the iron arsenide superconductors.

9.3 Thermodynamic and Transport Measurements

Bud'ko et al. (2009) presented thermodynamic, structural, and transport measurements on $Ba(Fe_{1-x}Cr_x)_2As_2$ ($x = 0.027$) single crystals. All measurements revealed sharp anomalies at ~ 112 K. Single crystal x-ray diffraction identified the structural transition as first order, from the high-temperature tetragonal $I4/mmm$ to the low-temperature orthorhombic $Fmmm$ structure, in contrast to an earlier report (Sefat et al. (2009b)).

Mun et al. (2009) measured temperature-dependent thermoelectric power (TEP) data on $Ba(Fe_{1-x}TM_x)_2As_2$ (TM=Co and Cu) as well as Hall coefficient data on samples from the same batches. For Co substitution there is a clear change in the temperature-dependent TEP and Hall coefficient data when e (the number of extra electrons associated with the TM substitution) is increased sufficiently to stabilize low-temperature superconductivity. Remarkably, a similar change is found in Cu-substituted samples at comparable e value, even though these compounds do not superconduct. These changes may point to a significant modification of the Fermi surface/band structure of $Ba(Fe_{1-x}TM_x)_2As_2$ at low substitution levels. In the case of Co substitution, this is just before, and may allow for, the onset of superconductivity. These data further suggest that suppression of the structural/magnetic phase transition and the establishment of a proper e value are each necessary but not individually sufficient conditions for superconductivity.

The parent compounds of iron-arsenide superconductors, AFe_2As_2 (A=Ca, Sr, Ba), undergo a tetragonal to orthorhombic structural transition at a temperature T_{TO} in the range 135-205 K depending on the alkaline-earth element. Below T_{TO} the free standing crystals twin, splitting into equally populated structural domains, which masks the intrinsic, in-plane, anisotropic properties of the materials. Tanatar et al. (2010a) demonstrated a way of mechanically detwinning $CaFe_2As_2$ and $BaFe_2As_2$. By making one crystallographic orientation more energetically favorable, the material remains single-crystalline below the structural transition temperature, eliminating the domain splitting normally seen. The detwinning was nearly complete, as demonstrated by polarized light imaging and synchrotron x-ray measurements, and reversible, with twin pattern restored after strain release. Electrical resistivity measurements made in the twinned and detwinned states showed that resistivity, ρ, decreased along the orthorhombic a_o axis but increases along the orthorhombic b_o axis in both compounds. Immediately below T_{TO} the ratio $\rho_{bo}/\rho_{ao} = 1.2$ for Ca compounds and 1.5 for Ba compounds. Contrary to $CaFe_2As_2$, $BaFe_2As_2$ revealed an anisotropy in the nominally tetragonal phase, suggesting that either fluctuations play a larger role above T_{TO} in $BaFe_2As_2$ than in $CaFe_2As_2$ or that there is a higher temperature crossover or phase transition.

Colombier et al. (2010) investigated the in-plane resistivity of single crystalline samples of

Ba(Fe$_{1-x}$Co$_x$)$_2$As$_2$ (x=0.038, 0.047, 0.074, 0.1 and 0.114), Ba(Fe$_{0.973}$Cr$_{0.027}$)$_2$As$_2$ and slightly tin-substituted BaFe$_2$As$_2$ under various pressures up to 7.5 GPa, in order to establish temperaturepressure, $T(P)$, phase diagrams and to compare the inuence of pressure and substitution on superconductivity. At ambient pressure, cobalt substitution is known to lead to a decrease in the combined magnetic and structural transition temperature T_0. Likewise, an increase of pressure tends to have the same effect for Ba(Fe$_{1-x}$Co$_x$)$_2$As$_2$ for the various values of x. As was seen in the $T(P)$ phase diagram of BaFe$_2$As$_2$ (Colombier et al. (2009)), a superconducting dome was observed for Ba(Fe$_{1-x}$Co$_x$)$_2$As$_2$ samples with the dome shifted to lower temperatures and pressures with increased cobalt substitution levels. A very different behavior was noticed for Ba(Fe$_{0.973}$Cr$_{0.027}$)$_2$As$_2$ and the slightly tin-substituted BaFe$_2$As$_2$ with the decrease of T_0 being close to linear down to 2 K, and no obvious sign of superconductivity in the pressure range investigated.

Tanatar et al. (2010b) used temperature-dependent interplane resistivity, $\rho_c(T)$, to characterize the normal state of the iron-arsenide superconductor Ba(Fe$_{1-x}$Co$_x$)$_2$As$_2$ over a broad substitution range $0 \leq x < 0.50$. The data were compared with in-plane resistivity, $\rho_a(T)$, and magnetic susceptibility, $\chi(T)$, taken in $H \perp c$, as well as Co NMR Knight shift, ^{59}K, and spin-relaxation rate, $1/T_1T$. The interplane resistivity data showed a clear correlation with the NMR Knight shift, assigned to the formation of the pseudogap. Evolution of $\rho_c(T)$ with substitution level revealed two characteristic energy scales. The temperature of the crossover from nonmetallic, increasing on cooling, behavior of $\rho_c(T)$ at high temperatures to metallic behavior at low temperatures, T, correlated well with an anomaly in all three magnetic measurements. This characteristic temperature, equal to approximately 200 K in the parent compound, $x = 0$, decreased with substitution and vanishes near $x \approx 0.25$. For substitution levels $x \geq 0.166$, an additional feature appeared above T with metallic behavior of $\rho_c(T)$ found above the low-temperature resistivity increase. The characteristic temperature of this charge-gap formation, T_{CG}, vanished at $x_{CG} \approx 0.30$, paving the way to metallic, T linear, $\rho_c(T)$ close to x_{CG} and superlinear T dependence for $x > x_{CG}$. None of these features were evident in the in-plane resistivity $\rho_a(T)$. For substitution levels $x < x_{CG}$, $\chi(T)$ showed a known, anomalous, T-linear dependence, which disappeared for $x > x_{CG}$. These features were consistent with the existence

of a charge gap, accompanying formation of the magnetic pseudogap, and its critical suppression with substitution. The inferred c-axis charge gap reflects the three-dimensional character of the electronic structure and of the magnetism in the iron arsenides.

Hodovanets et al. (2011) presented temperature-dependent, in-plane, thermoelectric power (TEP) data for $Ba(Fe_{1-x}Ru_x)_2As_2$ $(0 \leq x \leq 0.36)$ single crystals. These data confirm the previously outlined $x - T$ phase diagram for this system (Thaler et al. (2010), 5). The analysis of TEP evolution with Ru substitution suggests significant changes in the electronic structure, correlations, and/or scattering occurring near $x_{Ru} \sim 0.07, 0.30$, and possibly 0.20. These results are compared with an extended set of TEP data for the $Ba(Fe_{1-x}Co_x)_2As_2$ series for which initial angle-resolved photoemission spectroscopy (Liu et al. (2010)) and transport studies (Mun et al. (2009)) have identified $x \sim 0.02$ as the concentration at which the Lifshitz transition takes place. In addition to $x \sim 0.02$ the Co levels of $x \approx 0.11$ and 0.22 are identified as concentrations at which similar changes occur.

Blomberg et al. (2011) studied intrinsic, in-plane anisotropy of electrical resistivity on mechanically detwinned single crystals of $SrFe_2As_2$ above and below the temperature of the coupled structural/magnetic transition, T_{TO}. Resistivity is smaller for electrical current flow along the orthorhombic a_o direction (direction of antiferromagnetically alternating magnetic moments) and is larger for transport along the b_o direction (direction of ferromagnetic chains), which is similar to $CaFe_2As_2$ and $BaFe_2As_2$ compounds. A strongly first-order structural transition in $SrFe_2As_2$ was confirmed by high-energy x-ray measurements, with the transition temperature and character unaffected by moderate strain. For small strain levels, which are just sufficient to detwin the sample, they found a negligible effect on the resistivity above T_{TO}. With the increase of strain, the resistivity anisotropy starts to develop above T_{TO}, clearly showing the relation of anisotropy to an anomalously strong response to strain. This study suggests that electronic nematicity cannot be observed in the FeAs-based compounds in which the structural transition is strongly first order.

Tanatar et al. (2011) made systematic measurements of temperature-dependent interplane resistivity $\rho_c(T)$ as a function of transition-metal substitution in the iron-arsenide superconductors $Ba(Fe_{1-x}TM_x)_2As_2$ (TM=Ni, Pd, Rh). The data were compared with the behavior

found in $Ba(Fe_{1-x}Co_x)_2As_2$, revealing resistive signatures of pseudogap. In all compounds the authors find resistivity crossover at a characteristic pseudogap temperature T^* from nonmetallic to metallic temperature dependence on cooling. Suppression of T^* proceeds very similarly in cases of Ni and Pd substitution and much faster than in similar cases of Co and Rh substitution. In cases of Co and Rh substitution an additional minimum in the temperature-dependent ρ_c emerges for high substitution levels, when superconductivity is completely suppressed. These features are consistent with the existence of a charge gap covering part of the Fermi surface. The part of the Fermi surface affected by this gap is notably larger for Ni- and Pd-substituted compositions than in Co- and Rh-substituted compounds.

Kim et al. (2011c) studied the ab plane resistivity of $Ba(Fe_{1-x}Ru_x)_2As_2$ (x=0.00, 0.09, 0.16, 0.21, and 0.28) under nearly hydrostatic pressures up to 7.4 GPa in order to explore the T-P phase diagram and to compare the combined effects of isoelectronic Ru substitution and pressure. The parent compound $BaFe_2As_2$ exhibits a structural/magnetic phase transition near 134 K. At ambient pressure, progressively increasing Ru concentration suppresses this phase transition to lower temperatures at an approximate rate of ~5 K/% Ru correlated with the emergence of superconductivity. By applying pressure to this system, a similar behavior is seen for each concentration: the structural/magnetic phase transition is further suppressed and superconductivity induced and ultimately, for larger x_Ru and P, suppressed. A detailed comparison of the TP phase diagrams for all Ru concentrations shows that a pressure of 3 GPa is roughly equivalent to 10% Ru substitution. Furthermore, due to the sensitivity of $Ba(Fe_{1-x}Ru_x)_2As_2$ to pressure conditions, the melting of the liquid media, 4:6 light mineral oil : n-pentane and 1:1 isopentane : n-pentane, used in this study could be readily seen in the resistivity measurements. This feature was used to determine the freezing curves for these media and to infer their room temperature, hydrostatic limits: 3.5 and 6.5 GPa, respectively.

Blomberg et al. (2012) characterized the effect of uniaxial tensile stress and the resultant strain on the structural/magnetic transition in the parent compound of the iron arsenide superconductor $BaFe_2As_2$ by temperature-dependent electrical resistivity, x-ray diffraction, and quantitative polarized light imaging. They show that strain induces a measurable uniaxial structural distortion above the first-order magnetic transition and significantly smears the struc-

tural transition. This response is different from that found in a related compound, $SrFe_2As_2$, where the coupled structural and magnetic transitions are strongly first order (Blomberg et al. (2011). This difference in the structural responses explains the in-plane resistivity anisotropy above the transition in $BaFe_2As_2$. This conclusion is supported by the Ginzburg-Landau-type phenomenological model for the effect of the uniaxial strain on the resistivity anisotropy.

9.4   ARPES

Liu et al. (2010) reported evidence from angle-resolved photoemission spectroscopy that marked changes in the Fermi surface coincide with the onset of superconductivity in $Ba(Fe_{1-x}Co_x)_2As_2$.The presence of the AFM order leads to a reconstruction of the electronic structure, most significantly the appearance of the petal-like hole pockets at the Fermi level. These hole pockets vanish–that is, undergo a Lifshitz transition (Lifshitz (1960))–as the Co concentration is increased sufficiently to support superconductivity. Superconductivity and magnetism are competing states in this system: when petal-like hole pockets are present, superconductivity is fully suppressed, whereas in their absence the two states can coexist.

Liu et al. (2011) used angle-resolved photoemission spectroscopy and thermoelectric power to study the poorly explored, highly oversubstituted side of the phase diagram of $Ba(Fe_{1-x}Co_x)_2As_2$. Their data demonstrate that several Lifshitz transitions–topological changes of the Fermi surface–occur for large x. The central hole barrel changes to ellipsoids that are centered at Z at $x \sim 0.11$ and subsequently disappear around $x \sim 0.2$; changes in thermoelectric power occur at similar x values (Mun et al. (2009); Hodovanets et al. (2011)). T_c decreases and goes to zero around $x \sim 0.15$–between the two Lifshitz transitions. Beyond $x = 0.2$ the central pocket becomes electron-like and superconductivity does not exist. These observations reveal the importance of the underlying Fermiology in electron-carrier substituted iron arsenides. The authors speculate that a likely necessary condition for superconductivity in these materials is the presence of the central hole pockets rather than nesting between central and corner pockets.

Dhaka et al. (2011) used high resolution angle-resolved photoemission to study the electronic structure of the iron based high-temperature superconductors $Ba(Fe_{1-x}Ru_x)_2As_2$ as a function of Ru concentration. They find that substitution of Ru for Fe is isoelectronic, i.e. it does

not change the value of the chemical potential. More interestingly, there are no measured, significant changes in the shape of the Fermi surface or in the Fermi velocity over a wide range of substitution levels ($0 < x < 0.55$). Given that the suppression of the antiferromagnetic and structural phase is associated with the emergence of the superconducting state, Ru substitution must achieve this via a mechanism that does not involve changes of the Fermi surface. The authors speculate that this mechanism relies on magnetic dilution which leads to the reduction of the effective Stoner enhancement.

9.5   Other Measurements

Martin et al. (2010) compared the temperature dependences of the in-plane London penetration depth ($\Delta\lambda_{ab}(T)$) for several Ba(Fe$_{1x}$TM$_x$)$_2$As$_2$ (TM = Co, Ni, Pd, Co + Cu) superconductors at high concentration of electrons, n_e, added per Fe site. They showed that regardless of the transition metal TM, for $n_e \geq 0.12$, the penetration depth has a power-law temperature dependence $\Delta\lambda_L(T) \propto T_n$, but with the exponent $n \approx 1.65$, thus signicantly lower than the value $n \geq 2$ previously reported for lower electron concentrations. On substituting Fe with electron-carrying transition 3d metals, the magnitude of the variation with temperature of $\Delta\lambda_L(T)$ is larger for Ni substitution than for Co substitution, and larger for Co + Cu double substitution than for Ni alone. However, comparing the effect of 3d and 4d electrons, for the isovalent elements Ni and Pd respectively, they found that the rates of change in penetration depth with temperature are nearly identical for the two compounds.

Wang et al. (2011) reported the results of a ^{57}Fe Mössbauer spectroscopy study of superconducting Ba(Fe$_{1-x}$Rh$_x$)$_2$As$_2$ ($x = 0.039$) between 2 and 294 K. The main component of the electric field gradient tensor at 294 K was shown to be positive and its increase with decreasing temperature is well described by a $T^{3/2}$ power-law relation. The shape of the Mössbauer spectra below the Néel temperature $T_N = 55.5(1)$ K was shown to result from the presence of substitution-induced disorder rather than of incommensurate spin-density-wave order. The measured hyperfine magnetic field reached its maximum value at the critical temperature $T_c = 14$ K and then decreased by 4.2% upon further cooling to 2 K. This constituted direct evidence of the coexistence of and competition between superconductivity and magnetic

order. The extrapolated value of the Fe magnetic moment at 0 K is determined to be $0.35(1)$ μ_B. The Debye temperature of $Ba(Fe_{1-x}Rh_x)_2As_2$ ($x = 0.039$) was found to be $357(3)$ K.

Ofer et al. (2012) measured the absolute value and temperature dependence of the in-plane magnetic penetration depth λ on a single crystal of $Ba(Fe_{1-x}Co_x)_2As_2$ ($x = 0.074$) using low-energy muon-spin rotation and microwave cavity perturbation. The magnetic field profiles in the Meissner state were consistent with a local London model beyond a depth of 15 nm. The authors determined the gap symmetry through measurements of the temperature dependence of the superfluid density which follows a two-gap s-wave model over the entire temperature range below T_c. While the intermediate to high temperature data was well fit by an energy gap model in the BCS-like (weak-coupling) limit, a second smaller gap becomes apparent at low temperatures.

Bossoni et al. (2012) performed ^{75}As NMR spin-lattice relaxation ($1/T_1$) and spin-echo decay ($1/T_2$) rate measurements in a single crystal of superconducting $Ba(Fe_{1-x}Rh_x)_2As_2$ ($x = 0.07$). Below the superconducting transition temperature T_c, when the magnetic field H is applied along the c axis, a peak in both relaxation rates was observed. Remarkably, that peak was suppressed for $H \perp c$. Those maxima in $1/T_1$ and $1/T_2$ were ascribed to the flux lines lattice motions and the corresponding correlation times and pinning energy barriers were derived on the basis of a heuristic model. Further information on the flux lines motion was derived from the narrowing of ^{75}As NMR linewidth below T_c and found to be consistent with that obtained from $1/T_2$ measurements. All the experimental results are described in the framework of thermally activated vortices motions.

CHAPTER 10.   Summary and Conclusions

As discussed in Section 2.3, many superconducting materials belong to families of compounds that can be tuned into or out of superconductivity by one or more tuning parameters. The superconducting state often does not appear in the parent compound under ambient conditions, even at extremely low temperature. Single crystalline $BaFe_2As_2$ undergoes strongly coupled tetragonal to orthorhombic and paramagnetic to antiferromagnetic phase transitions at 134 K (Pfisterer and Nagorsen (1980); Rotter et al. (2008b); Ni et al. (2008b); Colombier et al. (2009); Kim et al. (2011a,c)), but it does not superconduct under ambient conditions all the way down to 2 K. These coupled structural and magnetic transitions can be suppressed by application of mechanical pressure (Torikachvili et al. (2008); Canfield and Bud'ko (2010)) or by various chemical substitutions onto the Ba, Fe or As sites (Ni et al. (2008a,b, 2009, 2010); Luo et al. (2008); Sefat et al. (2008b, 2009b); Li et al. (2009); Ni (2009); Bud'ko et al. (2009); Jiang et al. (2009); Kasahara et al. (2010); Thaler et al. (2010, 2011). Mechanical pressure as well as a subset of these chemical substitutions can also induce superconductivity (Torikachvili et al. (2008); Canfield and Bud'ko (2010); Ni et al. (2008a,b, 2009, 2010); Luo et al. (2008); Sefat et al. (2008b); Li et al. (2009); Ni (2009); Jiang et al. (2009); Kasahara et al. (2010). Motivated by the questions raised in Chapters 1 and 2, we studied the effects on structural and magnetic phase transitions and the emergence of superconductivity in transition metal substituted $BaFe_2As_2$. We grew four series of $Ba(Fe_{1-x}TM_x)_2As_2$ (TM=Ru, Mn, Co+Cr and Co+Mn) and characterized them by crystallographic, magnetic and transport measurements. We also subjected $Ba(Fe_{1-x}Cr_x)_2As_2$ and $Ba(Fe_{1-x}Co_x)_2As_2$ to heat treatment to explore what changes might be induced.

As shown in Fig. 10.1, the phase space of the ferropnictide and cuprate families show similar parallels when we consider the electron and hole-doping induced phase changes. However, the
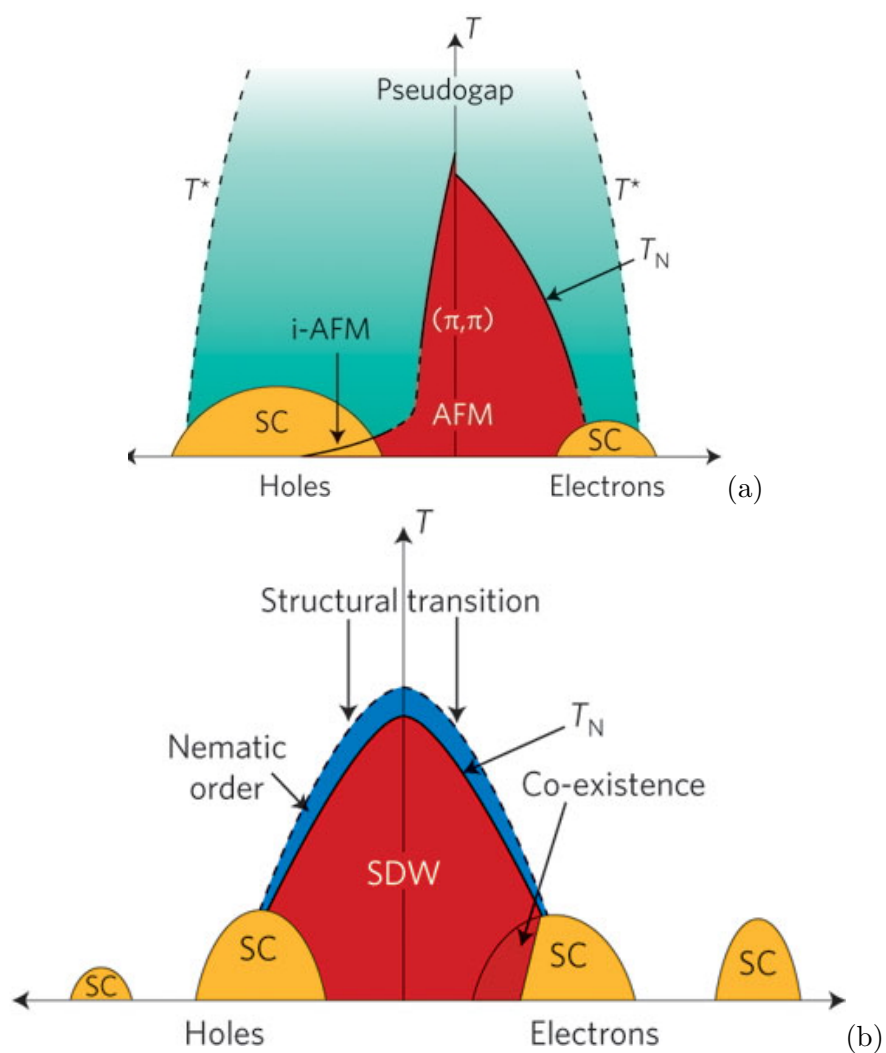
Figure 10.1: Generic electronic phase diagram for layered copper oxide materials (a) and ferro-pnictides (b) (Basov and Chubukov (2011)).

drastic qualitative difference between the left sides of Figs. 10.1 and 6.15 (p. 79) shows that this is not universal. Mn's position on the periodic table suggests that it should contribute one less electron than Fe just as K contributes one less than Ba and Co contributes one more than Fe, but while K substitution on the Ba site and Co substitution on the Fe site of $BaFe_2As_2$ both induce superconductivity, our results – the red dots in Fig. 6.15 – demonstrate that Mn substitution on the Fe site does not. It is not clear whether this is a result of Mn not acting as a hole donor in the same way as K, or if it is a result of some more complex issue, possibly stemming from lattice distortion by the Mn or a magnetic effect of the inclusion of Mn. This point is driven home even more completely when we compare $Ba(Fe_{1-x-y}Co_xCr_y)_2As_2$ and $Ba(Fe_{1-x-y}Co_xMn_y)_2As_2$ with $Ba(Fe_{1-x}Co_x)_2As_2$: simple hole band filling and hole contributions from the Cr or Mn would scale the phase diagram back down when looking at a particular Co substitution. Instead, we observed that the extra inclusion further suppresses $T_{s,m}$ and rapidly suppresses T_c.

Meanwhile, there is another break in the parallel with the cuprates: Ru substitution on the Fe site. Since Ru is isoelectronic with Fe, it provides neither electrons nor holes to the system. Nevertheless, the phase diagram is eerily similar to that seen for K, Co, Ni, Rh and Pd substitutions. As shown in Fig. 5.8, Ru substitution suppresses the structural and magnetic transitions and, with sufficiently large substitution fraction, induces superconductivity. This means that just electron count is not sufficient to account for superconductivity in this system. The parallel between Ru substitution and pressure – suppression of the structural and magnetic transitions and emergence of superconductivity without the contribution of additional electrons as well as wide superconducting transitions – suggests that lattice distortion may be important for the emergence of superconductivity in this system, at least when no extra electrons are added. The evidence for this is particularly strong when we consider that scaling with $\Delta \frac{c/c_0}{a/a_0}$ lines up the structural and magnetic transition suppression very closely for both application of pressure and Ru substitution while also causing the superconducting domes to partially overlap (Fig. 5.12). On the other hand, comparison with another isoelectronic substitution, P on the As site, gives no trend with $\Delta \frac{c/c_0}{a/a_0}$ but does with $\Delta c/c_0$ (Fig. 5.14). It is unclear what the source of this discrepancy is.

Based on the strain sensitivity of some of $BaFe_2As_2$'s relatives, we would expect that annealing, if it were to have any effect at all, would be deleterious for superconductivity in this system. Instead, we have found that at least in some cases, heat treatment of $Ba(Fe_{1-x}Co_x)_2As_2$ samples can increase T_c dramatically. As seen in Fig. 8.3(a), resistive measurement of heat treated $Ba(Fe_{1-x}Co_x)_2As_2$ samples with $x \approx 0.12$ sees an increase in T_c from $\sim$12 K to $\sim$25 K. However, magnetic measurement of the superconducting state does not see this large increase in T_c. Since magnetic measurement of the superconducting state is not nearly as sensitive to surface effects as resistive measurement, this suggests that the increase in T_c may only be a surface effect. In addition, Fig. 8.2 shows that heat treatment of $Ba(Fe_{1-x-y}Co_xCr_y)_2As_2$ samples can induce them to superconduct, even though adding Cr to a Co substitution which would superconduct by itself rapidly suppresses the superconducting state. In this case, magnetic measurements confirm the existence of the superconducting state, though not at quite the same T_c as seen by resistance. Problems with controlling differences between the samples make it difficult to draw conclusions from this data, and further investigation may be warranted.

APPENDIX A.   List of Substitutions

Listed here are the samples prepared in the $BaFe_2As_2$ family, with various dopants and substitution levels. Each table gives our internal batch growth code and the substitution level x_{WDS} as well as y_{WDS} for doubly-substituted growths. Some growths have x_{nom} and y_{nom}, the nominal substitution fraction. As discussed in Chapter 9, the correlation between nominal and WDS values can be used to predict what nominal substitution level is needed to get a desired WDS value. Where available, 2σ and the number of points, N, used to calculate x_{WDS} and 2σ is given. Unfortunately, some entries are incomplete because the data was unavailable.

Table A.1: $BaFe_2As_2$

Batch	Comment
PM657	Sn
PM658	Sn
PM612	Sn
PM682	Sn
PM619	Sn
PM684	Sn
PM888	
SA171-1	
KQ809	
KQ801	
SA171-2	

Table A.2: Batches with 'Sn' in the comment column were grown with Sn flux instead of FeAs flux.

Table A.3: $Ba(Fe_{1-x}Co_x)_2As_2$

Batch	x_{nom}	x_{WDS}	$2\,\sigma$	N
SA899	0.35	0.3244	0.13003	12
SA900	0.675	0.4400	0.164606	12
SA901	1.025	0.7335	0.090389	12
KQ363		0.9352	0.084183	22
SA902	1.35	0.9510	0.163978	12
SA903	17	1.0670	0.149265	12
PM991		1.2846	0.10659	8
SA855	2.1325	1.51159	0.156392	12
KQ808		1.523916	0.155834	13
SA854	2	1.53223	0.127559	12
SA456-1		1.5487	0.17	
SA456-3		1.5523	0.08	
SA856	2.27	1.57983	0.172719	12
SA456-2		1.5959	0.16	
SA456-5		1.6171	0.11	
SA456-4		1.6232	0.14	
KQ364		1.6314	0.071855	14
SA342-5		1.6471	0.089005	12
SA342-4		1.6500	0.195691	12
SA342-2		1.6542	0.112941	12
SA342-1		1.6543	0.119555	12
SA342-3		1.7049	0.119629	12
SA857	2.4	1.84521	0.132432	12
SA858	2.5325	1.87305	0.173722	12
SA859	2.6675	1.87438	0.175343	12
SA780	2.53	1.9442	0.199275	12
PM922		1.9601	0.094032	4
SA781	2.66	2.1064	0.075704	12
SA784	3.06	2.1983	0.111133	12
SA782	2.79	2.2245	0.151375	12
SA785	3.19	2.2688	0.15178	12
SA832	3.27	2.35306	0.158274	12
SA831	3.23	2.39142	0.243609	12
MC292		2.4238	0.172023	
KQ177		2.4500	0.129851	28
MC094	3.7	2.4807	0.307786	
SA833	3.5	2.48222	0.193146	12
SA786	3.32	2.5415	0.25312	12
SA834	3.6	2.54954	0.187849	12
SA787	3.45	2.5577	0.148374	12
MC293		2.6665	0.232993	
KQ365		2.8313	0.08895	19
MC098	4.825	3.0353	0.431516	

$$Ba(Fe_{1-x}Co_x)_2As_2$$

Batch	x_{nom}	x_{WDS}	$2\,\sigma$	N
MC096	4.275	3.0825	0.298385	
MC095	3.975	3.1808	0.268151	
MC097	4.8	3.3973	0.332156	
MC306		3.4329	0.187466	
SA460-1		3.4589	0.136458	12
SA460-3		3.4890	0.138605	12
SA460-2		3.4978	0.108086	12
SA460-4		3.5113	0.127453	12
SA460-5		3.6062	0.173125	12
SA783	2.93	3.6125	0.144746	12
SA345-1		3.6367	0.119274	12
SA345-2		3.6665	0.182288	12
SA345-5		3.6673	0.191988	12
SA345-4		3.7090	0.218981	12
SA345-3		3.7232	0.181738	12
PM891		3.7765	0.208921	7
SA172		3.9008	0.248567	12
KQ270		4.2000	0.152784	12
SA308-3		4.2100	0.14067	12
SA308-2		4.2300	0.085255	12
SA308-1		4.3100	0.169589	12
KQ366		4.3332	0.174023	12
SA255		4.3400	0.177459	12
KQ271		4.3402	0.079361	6
MC295		4.5181	0.184263	
SA835	6.5	4.61063	0.259714	12
PM924		4.7019	0.084734	4
SA095-2		5.357623	0.3756	12
SA095-3		5.376673	0.17633	12
KQ311		5.3852	0.115668	19
SA095-1		5.426341		
SA095-5		5.566811	0.336915	12
SA678-4		5.6400	0.023047	12
SA095-4		5.672503	0.362455	12
KQ533		5.757	0.297305	27
KQ595		5.894473	0.267858	12
KQ534		5.898	0.147933	12
PM902		5.9580	0.907149	5
KQ325		6.0944	0.085371	20
KQ535		6.163	0.174176	12
KQ610		6.208225	0.226217	17
KQ596		6.220908	0.142208	12

$$Ba(Fe_{1-x}Co_x)_2As_2$$
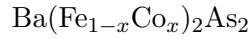
Batch	x_{nom}	x_{WDS}	$2\,\sigma$	N
KQ609		6.295903	0.104299	26
KQ312		6.2986	0.095836	8
KQ594		6.585	0.654843	12
KQ313		6.7416	0.140205	20
KQ051		7.0118	0.132639	6
PM871		7.2051	0.328741	3
SA152-1		7.4030	0.184384	12
PM892		7.6085	0.103331	3
SA257		7.6400	0.141003	12
KQ257		7.6448	0.109475	14
SA152-2		7.7156	0.208311	12
SA362		8.3100	0.123432	12
KQ326		8.5548	0.186622	20
KQ314		9.0668	0.173638	15
PM904		9.9629	0.752801	6
SA789		10.0638	0.192007	12
KQ327		10.7071	0.160155	20
KQ050		10.7406	0.140472	6
PM893		11.3607	0.363062	3
SA256		12.4500	0.535344	12
KQ201		12.7439	0.247933	16
KQ909		13.16775	0.174156	9
KQ175		13.4000	0.22985	5
PM979		14.0254	0.15827	
KQ258		16.6335	0.24958	9
KQ908		16.81435	0.38117	9
KQ858		23.8000	0.46423	12
KQ956		24.79	0.12756	
SA309		25.0800	0.15639	12
SA310		31.0200	0.17272	12
KQ459		31.3000	0.86194	12
KQ202		45.9000	0.388	8
KQ129		66.5000	0.49098	25
MC452	6.75	5.8276	0.267217	
MC453	7.425	5.8636	0.285817	
MC398	15	11.3218	0.323147	
MC449	4.725	3.4464	0.220889	
MC450	5.4	3.8049	0.225403	
MC451	6.075	4.9820	0.25703	
MC399	15	11.5287	0.408643	
MC400	15	11.2329	0.44664	
MC401	15	11.8258	0.712787	

$$Ba(Fe_{1-x}Co_x)_2As_2$$

Batch	x_{nom}	x_{WDS}	$2\,\sigma$	N
MC350	15	10.6468	0.371479	
MC351	15	9.5951	0.551931	
MC352	15	8.4627	0.379697	
MC353	15	15.6942	0.683631	
MC354	15	14.8638	0.788926	
SA508-1		4.6066	0.3596	
SA508-2		4.6507	0.242195	
SA509-1		7.6420	0.341546	
SA509-2		7.5284	0.266275	
SA510-1		9.6570	0.230299	
SA510-2		9.3518	0.333127	

Table A.4: $Ba(Fe_{1-x}Ni_x)_2As_2$

Batch	x_{nom}	x_{WDS}	$2\,\sigma$	N
KQ077		0.67	0.140728	18
KQ078		1.6	0.643945	10
SA284-2		1.997336	0.092827	12
SA284-1		2.108255	0.084142	12
SA814		2.366492	0.16896	12
KQ080		2.64	0.376979	5
SA816		2.942169	0.156244	12
SA815		3.121417	0.150126	12
SA254		3.157112	0.102066	12
KQ081		3.35	0.276956	18
SA817		3.484952	0.170042	12
KQ392		3.618329	0.152599	27
SA952		3.6535	0.229348	12
PM946		4.604626	0.160861	11
PM950		4.613946		
PM949		4.660471		
KQ393		4.734342	0.191273	14
PM948		4.83121		
PM947		4.8469	0.16896	
KQ111		5.4	0.232684	12
KQ370		6.361988	0.170042	14
KQ114		7.13	0.294677	6

Table A.5: Ba(Fe$_{1-x}$Cu$_x$)$_2$As$_2$

Batch	x_{nom}	x_{WDS}	$2\,\sigma$	N
PM973		0.710212	0.13314	5
KQ449		0.932759	0.156247	43
PM974		1.967893	0.203249	5
KQ309-1		2.323871		
PM987		2.56769	0.197329	8
KQ308-1		2.760031	0.379361	37
KQ308-2		2.764398		
KQ034		3.345921	0.467395	17
KQ360		3.923409	0.438751	26
KQ300		3.942971	0.151052	33
KQ309-2		4.106631		
KQ359		4.46239	0.260658	29
KQ275		4.725669	0.359543	13
PM997		4.970077	0.120559	10
KQ043		5.219787	0.469983	40
PM943		6.186095	0.216105	5
KQ044		6.421538	0.169203	7
KQ045		6.822791	0.103178	6
KQ124		9.25	0.846103	10
KQ126		16.49	1.621405	8
KQ131		22.5	0.355646	6
KQ132		25.8	0.556061	6
KQ127		29.23	2.630869	60
KQ133		36.5	0.420645	7

Table A.6: Ba(Fe$_{1-x}$Cr$_x$)$_2$As$_2$

Batch	x_{nom}	x_{WDS}	$2\,\sigma$	N
KQ301	2.5	2.755797		
SA093	15.3075	11.95	0.46	12
SA092	11.11	8.139737	0.233731	24
SA090		4.566294	1.887468	27
KQ763	0.500	0.441	0.095	11
KQ764	2.000	1.754	0.127	13
KQ765	4.000	3.070	0.217	10
KQ766	6.000	4.382	0.249	12
SA838		2.667263	0.217523	12
SA839		2.744932	0.180591	12
SA840		3.654402	0.249561	12
SA841		4.506665	0.252859	12
SA842		5.625459	0.219195	12
SA843		6.599613	0.393473	12

Table A.7: $Ba(Fe_{1-x}Mn_x)_2As_2$

Batch	x_{nom}	x_{WDS}
KQ902		1.3710
KQ971		1.73
KQ204		2.2504
KQ999		2.57
SA008		3.27
KQ203		4.4140
SA766-5		4.6122
SA766-3		4.9727
KQ904		5.1581
SA766-4		5.5662
SA766-2		5.7936
KQ430		5.798318
SA201-4		7.0650
SA201-3		7.0932
SA201-5		7.1678
SA201-1		7.2570
SA201-2		7.2939
KQ905		7.3910
SA151-2		7.6143
SA151-1		7.6570
SA022		9.2359
KQ431		9.93036
KQ972		10.74
SA253-5		11.1732
SA253-4		11.2223
SA253-2		11.2904
SA009		11.33
SA253-3		11.4981
SA377-2		11.5987
SA528-4		11.9536
SA488-1		11.9753
SA377-4		11.9848
SA488-2		11.9917
SA377-3		12.0131
SA377-4		12.0291
SA377-1		12.2807
SA203-5		12.2815
SA377-5		12.4528
SA377-1		12.4626
SA528-2		12.4958
SA528-5		12.5933

$$\mathrm{Ba(Fe_{1-x}Mn_x)_2As_2}$$
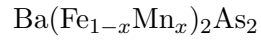
Batch	x_{nom}	x_{WDS}
SA203-3		12.6934
SA203-2		12.7412
SA203-1		12.8259
SA114		12.9000
SA488-4		12.9437
SA203-4		13.1769
SA488-5		13.2258
SA010		14.5030
KQ924		14.7460
KQ925		17.5810
KQ973		33.64
SA186		54.2210
SA622		56.8800
SA187		63.6296
SA623		72.8600
SA188		83.2348
SA190		87.7406
SA189		89.9916
SA011		92.65
SA012		97.10
SA013		99.82
SA113-1		11.7891
SA113-2		12.2199

Because of $\mathrm{Ba(Fe_{1-x}Mn_x)_2As_2}$ phase separation problems, I do not show 2σ here. See Chapter 6 for details.

Table A.8: Ba(Fe$_{1-x}$Ru$_x$)$_2$As$_2$

Batch	x_{nom}	x_{WDS}	2 σ	N
KQ383		2.06957	0.102465	14
KQ384		4.819523	0.122912	16
KQ346		4.844686	0.212074	15
SA222		6.3		
KQ918		7.278804	0.074801	12
KQ919		9.192597	0.328756	12
KQ920		12.6238	0.348059	11
KQ355		16.12094	0.544128	19
KQ564		20.81822	5.474156	23
KQ577		20.97094	0.574887	7
KQ368		23.83658	4.673683	13
SA420-2		25.29	0.50463	12
SA420-1		26.22	1.529378	12
KQ482		28.5299	7.393174	7
KQ565		28.69255	4.686532	14
SA326		30		
KQ578		32.88365	13.50905	15
KQ385		35.88547	4.934513	25
KQ399		55.33971	9.014896	12
MC504		9.32	0.44	12
MC505		7.47	0.24	12

Table A.9: Ba(Fe$_{1-x}$Rh$_x$)$_2$As$_2$

Batch	x_{nom}	x_{WDS}	2 σ	N
KQ231		1.2088	0.1649	10
KQ232		2.5549	0.1598	10
KQ298		3.8100	0.1351	12
KQ302		3.9473	0.1901	22
KQ233		5.6989	0.2544	9
KQ236		7.5555	0.3988	15
SA363		7.8100	0.0497	12
KQ234	15	9.3869	0.7545	32
KQ292	18	13.0035	0.2548	8
KQ286	22	17.1252	0.2363	21
SA626	30	29.9500	0.4426	12
SA627	35	35.8800	1.3254	12
SA698		18.6718	0.2887	12
SA699		22.4360	0.6879	12

Table A.10: Ba(Fe$_{1-x}$Pd$_x$)$_2$As$_2$

Batch	x_{nom}	x_{WDS}	2σ	N
KQ238		1.2	0.105196	10
KQ245		4.3	0.063515	6
KQ247-1		6.330985	0.259226	10
KQ247-2		6.773021	0.130076	10
KQ244		2.001596	0.182443	6
KQ246		5.281463	0.171716	12
KQ287		2.145614	0.147474	9
KQ288		3.033036	0.151182	6
KQ290		6.579693	0.248692	14
KQ289		4.124268	0.270994	10
KQ244		2.478779	0.352784	3
KQ293		7.567101	0.539771	52
KQ247		6.492106	0.867118	10
KQ299		2.632176	0.297783	52
KQ238		1.311755	0.142294	23

Table A.11: Ba(Fe$_{1-x}$Ir$_x$)$_2$As$_2$

Batch	x_{nom}	x_{WDS}	2σ	N
MC341	5	4.090036	1.131586	12
MC342	10	2.748549	0.198958	12
MC363	2.5	1.329464	0.0767	12
MC364	7.5	2.585004	0.173181	12
MC365	12.5	1.897922	0.101547	12
MC444	5	5.801358	2.034468	12
MC445	10	5.730167	1.524754	12

Table A.12: (Ba$_{1-x}$K$_x$)Fe$_2$As$_2$/Sn

Batch	x_{WDS}
PM654	12.96437
PM621	18.92257
PM626	44.75629
KQ-208-1	50.531
KQ-208-2	45.181

Table A.13: Ba(Fe$_{1-x-y}$Co$_x$Mn$_y$)$_2$As$_2$

Batch	Co x_{nom}	Mn y_{nom}	Co x_{WDS}	Co 2σ	Mn y_{WDS}	Mn 2σ	N
SA223	15.00	1.00	12.26	0.2171	0.633623	0.148052	12
KQ910	6.25	1.00	4.90	0.174	1.2	0.105	16
SA597	10.00	1.00	7.64	0.22	1.232786	0.174545	12
SA224	15.00	2.00	11.95	0.3359	2.247136	0.153681	12
KQ911	6.25	2.00	4.70	0.148	2.3	0.125	16
KQ960	10.00	2.00	7.65	16.66	2.322587	6.777227	10
SA598	10.00	3.00	7.45	0.17	3.435406	0.184405	12
SA596	6.25	3.00	5.02	0.14	3.526294	0.142933	12
KQ961	10.00	4.00	7.17	0.21	4.56937	0.148464	9
SA225	15.00	4.00	11.64	0.3863	4.718644	0.17912	12
KQ958	6.25	4.00	4.72	0.211123	4.76393	0.262759	12
KQ959	6.25	6.00	4.62	0.136585	6.904887	0.251671	14
KQ962	10.00	6.00	7.08	0.228809	7.529952	0.263185	13
MC303			12.43	0.311563	1.046801	0.087352	12
MC304			11.36	0.359396	1.917361	0.110726	12

Table A.14: $Ba(Fe_{1-x-y}Co_xCr_y)_2As_2$

Batch	Co x_{nom}	Cr y_{nom}	Co x_{WDS}	Co 2σ	Cr y_{WDS}	Cr 2σ	N
KQ401			3.234587	0.149866	1.336114	0.077016	10
KQ715	6.25	2	3.55	0.255105	1.32	0.156549	27
MC137-2	1.45	0.5	4.57	0.430125	1.29	0.329623	12
MC137-1	1.45	0.5	4.66	0.47467	1.09	0.190394	12
SA639	6.25	2	4.770458	0.205303	1.091619	0.31213	12
KQ714	6.25	1	4.8	0.153294	0.2	0.105778	26
KQ716	6.25	3	4.8	0.213511	2	0.14509	32
KQ989	6.25	7.2	4.91087	0.095539	6.913708	0.282635	13
SA640	6.25	4.5	5.038912	0.355336	3.234241	0.218156	12
MC154	1.75	0.75	5.048243	0.223911	2.066783	0.113008	12
MC155	1.8125	0.75	5.305682	0.295252	2.221001	0.131693	12
MC161	1.875	0.4375	5.440349	0.484572	1.208647	0.108373	12
MC156	1.875	0.75	5.452486	0.252415	2.134773	0.174145	12
MC160	1.875	1.125	5.487988	0.307618	3.210709	0.256761	12
MC157	1.9375	0.75	5.681074	0.136119	2.077096	0.177009	12
MC240			5.773634	0.243478	1.882743	0.156939	12
MC239			5.843602	0.23453	1.829899	0.120714	12
MC242			6.328046	0.278528	2.211901	0.09838	12
MC243			6.559481	0.180477	1.950267	0.11351	12
KQ718	10	2	7.6	0.248151	1.1	0.177504	28
KQ719	10	3	7.7	0.241433	2	0.202484	26
SA641	10	4.5	7.726711	0.373353	3.076067	0.278874	12
KQ717	10	1	7.8	0.254382	0.3	0.14861	27
SA558	15	3	11.9115	0.240864	1.960119	0.202497	12
SA557	15	2	12.00778	0.28601	1.33571	0.241265	12
SA559	15	4	12.13679	0.254738	2.540596	0.18305	12
SA556	15	1	12.23212	0.179143	0.732363	0.171604	12

Table A.15: Ba(Fe$_{1-x-y}$Co$_x$Cu$_y$)$_2$As$_2$

Batch	Co x_{nom}	Cu x_{nom}	Co x_{WDS}	Co 2σ	Cu real	Cu 2σ	N
KQ148			2.13	0.256409	2.23	0.229939	9
KQ160			2.2	0.220133	2.8	0.15301	12
KQ158			2.9	0.79762	1.96	0.167746	10
KQ161			2.6	0.314278	2.7	0.170771	9
KQ162			1.1	0.272638	2.2	0.173053	12
KQ159			3.3	0.219964	2	0.480595	33
KQ174			2.2	0.104129	4	0.728722	50
KQ162			2.2	0.078696	0.95	0.219345	20
KQ183			2.4	0.109813	0.54	0.188348	12
KQ260			1.529207	0.530071	3.611495	1.256212	39
KQ380			4.671077	0.170851	3.384362	0.375126	31
KQ379			5.230806	0.155398	0.445354	0.116707	18
KQ378			4.680743	0.19993	1.90277	0.223141	37
KQ382			5.073104	0.288155	0.448125	0.131788	8
KQ377			4.540154	0.20165	5.811051	0.587815	19
KQ381			4.503764	0.380486	4.662429	2.208552	24
KQ362			2.230901	0.132421	3.129192	0.30875	31

Bibliography

(1996). *Binary alloy phase diagrams.* ASM International, Materials Park, Ohio.

Abrikosov, A. A. (1957). On the magnetic properties of superconductors of the second group. *Zh. Eksp*, 32:1442.

Abrikosov, A. A. and Gor'kov, L. P. (1958). On the theory of superconducting alloys I: The electrodynamics of alloys at absolute zero. *Zh. Eksp. Teor. Fiz.*, 35:1558.

Abrikosov, A. A. and Gor'kov, L. P. (1961). Contribution to the theory of superconducting alloys with paramagnetic impurities. *Sev. Phys. JETP*, 12:1243.

Alireza, P. L., Ko, Y. T. C., Gillett, J., Petrone, C. M., Cole, J. M., Lonzarich, G. G., and Sebastian, S. E. (2009). Superconductivity up to 29 K in $SrFe_2As_2$ and $BaFe_2As_2$ at high pressures. *Journal of Physics: Condensed Matter*, 21(1):012208.

Anderson, P. W. (1959). Theory of dirty superconductors. *J. Phys. Chem. Solids.*, 11:26.

Bardeen, J. (1955). Theory of the Meissner Effect in Superconductors. *Phys. Rev.*, 97:1724.

Bardeen, J., Cooper, L. N., and Schr (1957a). Theory of Superconductivity. *Phys. Rev*, 108:1175.

Bardeen, J., Cooper, L. N., and Schrieffer, J. R. (1957b). Microscopic Theory of Superconductivity. *Phys*, 106:162.

Basov, D. N. and Chubukov, A. V. (2011). Manifesto for a higher T_c. *Nat Phys*, 7(4):272–276.

Batlogg, B., Kourouklis, G., Weber, W., Cava, R. J., Jayaraman, A., White, A. E., Short, K. T., Rupp, L. W., and Rietman, E. A. (1987). *Phys. Rev. Lett.*, 59:912.

Bednorz, J. G. and Müller, K. A. (1986). Possible high T_c superconductivity in the Ba-La-Cu-O system. *Z. Phys. B*, 64 (2):189.

Blomberg, E. C., Kreyssig, A., Tanatar, M. A., Fernandes, R. M., Kim, M. G., Thaler, A., Schmalian, J., Bud'ko, S. L., Canfield, P. C., Goldman, A. I., and Prozorov, R. (2012). Effect of tensile stress on the in-plane resistivity anisotropy in $BaFe_2As_2$. *Phys. Rev. B*, 85:144509.

Blomberg, E. C., Tanatar, M. A., Kreyssig, A., Ni, N., Thaler, A., Hu, R., Bud'ko, S. L., Canfield, P. C., Goldman, A. I., and Prozorov, R. (2011). In-plane anisotropy of electrical resistivity in strain-detwinned $SrFe_2As_2$. *Phys. Rev. B*, 83:134505.

Bossoni, L., Carretta, P., Thaler, A., and Canfield, P. C. (2012). NMR investigation of vortex dynamics in the $Ba(Fe_{0.93}Rh_{0.07})_2As_2$ superconductor. *Phys. Rev. B*, 85:104525.

Brouet, V., Rullier-Albenque, F., Marsi, M., Mansart, B., Aichhorn, M., Biermann, S., Faure, J., Perfetti, L., Taleb-Ibrahimi, A., Le Fèvre, P., Bertran, F., Forget, A., and Colson, D. (2010). Significant Reduction of Electronic Correlations upon Isovalent Ru Substitution of $BaFe_2As_2$. *Phys. Rev. Lett.*, 105(8):087001.

Bud'ko, S. L. and Canfield, P. C. (2006). Magnetism and superconductivity in rare earth-nickel-borocarbides. *Comptes Rendus Physique*, 7:56.

Bud'ko, S. L., Lapertot, G., Petrovic, C., Cunningham, C. E., Anderson, N., and Canfield, P. C. (2001). Boron Isotope Effect in Superconducting MgB_2. *Phys. Rev. Lett.*, 86:1877–1880.

Bud'ko, S. L., Nandi, S., Ni, N., Thaler, A., Kreyssig, A., Kracher, A., Yan, J.-Q., Goldman, A. I., and Canfield, P. C. (2009). Structural phase transition in $Ba(Fe_{0.973}Cr_{0.027})_2As_2$ single crystals. *Phys. Rev. B*, 80(1):014522.

Burns, R. G. (1993). *Mineralogical Applications of Crystal Field Theory*. Cambridge University Press.

Canfield, P. C. and Bud'ko, S. L. (2010). FeAs-Based Superconductivity: A Case Study of the Effects of Transition Metal Doping on $BaFe_2As_2$. *Annual Review of Condensed Matter Physics*, 1(1):27–50.

Canfield, P. C., Bud'ko, S. L., Cho, B. K., Beyermann, W. P., and Yatskar, A. (1997). RNi_2B_2C magnetic superconductors: An update from the front. *J. Alloys Comp.*, 250:596.

Canfield, P. C., Bud'ko, S. L., Ni, N., Yan, J. Q., and Kracher, A. (2009). Decoupling of the superconducting and magnetic/structural phase transitions in electron-doped $BaFe_2As_2$. *Phys. Rev. B*, 80(6):060501.

Canfield, P. C. and Fisher, I. R. (2001). High-temperature solution growth of intermetallic single crystals and quasicrystals. *Journal of Crystal Growth*, 225(2-4):155 – 161. Proceedings of the 12th American Conference on Crystal Growth and Epitaxy.

Canfield, P. C. and Fisk, Z. (1992). Growth of single crystals from metallic fluxes. *Phil. Mag. B*, 65:1117–1123.

Chen, X. J., Liang, B., Ulrich, C., Lin, C. T., Struzhkin, V. V., Wu, Z., Hemsey, R. J., k. Mao, H., and Lin, H. Q. (2007). *Phys. Rev. B*, 76:140502.

Chou, C., White, D., and Johnston, H. L. (1958). Heat Capacity in the Normal and Superconducting States and Critical Field of Niobium. *Phys. Rev.*, 109:788–796.

Chu, C. W., Gao, L., Chen, F., Huang, Z. J., Meng, R. L., and Xue, Y. Y. (1993). Superconductivity above 150 K in $HgBa_2Ca_2Cu_3O_{8+\delta}$ at high pressures. *Nature*, 365(6444):323–325.

Chu, J.-H., Analytis, J. G., Kucharczyk, C., and Fisher, I. R. (2009). Determination of the phase diagram of the electron-doped superconductor $Ba(Fe_{1-x}Co_x)_2As_2$. *Phys. Rev. B*, 79(1):014506.

Coleman, P. (2007). Heavy Fermions: electrons at the edge of magnetism. In Kronmuller, H. and Parkin, S., editors, *Handbook of Magnetism and Advanced Magnetic Materials.*, volume 1: *Fundamentals and Theory*, pages 95–148. John Wiley and Sons.

Colombier, E., Bud'ko, S. L., Ni, N., and Canfield, P. C. (2009). Complete pressure-dependent phase diagrams for $SrFe_2As_2$ and $BaFe_2As_2$. *Phys. Rev. B*, 79(22):224518.

Colombier, E., Torikachvili, M. S., Ni, N., Thaler, A., Bud'ko, S. L., and Canfield, P. C. (2010). Electrical transport measurements under pressure for $BaFe_2As_2$ compounds doped with Co, Cr, or Sn. *Superconductor Science and Technology*, 23:054003.

Cooper, L. N. (1956). Bound Electron Pairs in a Degenerate Fermi Gas. *Phys. Rev.*, 104:1189.

Dean, M. P. M., Kim, M. G., Kreyssig, A., Kim, J. W., Liu, X., Ryan, P. J., Thaler, A., Bud'ko, S. L., Strassheim, W., Canfield, P. C., Hill, J. P., and Goldman, A. I. (2012). Magnetically polarized Ir dopant atoms in superconducting $Ba(Fe_{1-x}Ir_x)_2As_2$. *Phys. Rev. B*, 85:140514.

Dhaka, R. S., Liu, C., Fernandes, R. M., Jiang, R., Strehlow, C. P., Kondo, T., Thaler, A., Schmalian, J., Bud'ko, S. L., Canfield, P. C., and Kaminski, A. (2011). What Controls the Phase Diagram and Superconductivity in Ru-Substituted $BaFe_2As_2$? *Phys. Rev. Lett.*, 107:267002.

Ding, H., Richard, P., Nakayama, K., Sugawara, K., Arakane, T., Sekiba, Y., Takayama, A., Souma, S., Sato, T., Takahashi, T., Wang, Z., Dai, X., Fang, Z., Chen, G. F., Luo, J. L., and Wang, N. L. (2008). Observation of Fermi-surface-dependent nodeless superconducting gaps in $Ba_{0.6}K_{0.4}Fe_2As_2$. *Europhysics Letters*, 83:47001.

Dong, J. K., Zhou, S. Y., Guan, T. Y., Zhang, H., Dai, Y. F., Qiu, X., Wang, X. F., He, Y., Chen, X. H., and Li, S. Y. (2010). Quantum Criticality and Nodal Superconductivitiy in the FeAs-Based superconductor KFe_2As_2. *Phys. Rev. Lett.*, 104:087005.

Doniach, S. (1977). The Kondo lattice and weak antiferromagnetism. *Physica B*, 91:231.

Eliashberg, G. M. (1960). Interactions between electrons and lattice vibrations in a superconductor. *Zh. Eksp. Teor. Fiz.*, 38:966.

Fernandes, R. M., Pratt, D. K., Tian, W., Zarestky, J., Kreyssig, A., Nandi, S., Kim, M. G., Thaler, A., Ni, N., Canfield, P. C., McQueeney, R. J., Schmalian, J., and Gold-

man, A. I. (2010). Unconventional pairing in the iron arsenide superconductors. *Phys. Rev. B*, 81:140501.

Fernandes, R. M., Vavilov, M. G., and Chubukov, A. V. (2012). Enhancement of T_c by disorder in underdoped iron pnictide superconductors. *Physical Review B*, 85(14):140512.

Fisk, Z. and Remeika, J. (1989). Chapter 81 Growth of single crystals from molten metal fluxes. volume 12 of *Handbook on the Physics and Chemistry of Rare Earths*, pages 53 – 70. Elsevier.

Fletcher, J. D., Serafin, A., Malone, L., Analytis, J. G., Chu, J.-H., Erickson, A. S., Fisher, I. R., and Carrington, A. (2008). Evidence for a Nodal-Line Superconducting State in LaFePO. *Phys. Rev. Lett.*, 102:147001.

Flouquet, J., Knebel, G., Braithwaite, D., Aoki, D., Brison, J.-P., Hardy, F., Huxley, A., Raymond, S., Salce, B., and Sheikin, I. (2006). Magnetism and superconductivity of heavy fermion matter. *Comptes Rendus Physique*, 7(1):22.

Franck, J. P., Jung, J., Mohamed, M.-K., Gygax, S., and Sproule, G. I. (1991). *Phys. Rev. B*, 44:5318.

Frohlich, H. (1952). Interaction of electrons with lattice vibrations. *Proc. Roy. Soc. Lond. A*, 215:291.

Ginzburg, V. L. and Laundau, L. D. (1950). On the theory of superconductivity. *Zh. Eksp. Teor. Fiz.*, 20:1064.

Goldstein, J., Newbury, D., Joy, D., Lyman, C., Echlin, P., Lifshin, E., Sawyer, L., and Michael, J. (2003). *Scanning Electron Microscopy and X-Ray Microanalysis, 3rd edition*. Springer Science+Business Media, Inc.

Gor'kov, L. P. (2008). *Superconductivity: Volume 1, Conventional and Unconventional Superconductors*. Springer.

Hashimoto, K., Kasahara, S., Katsumata, R., Mizukami, Y., Yamashita, M., Ikeda, H., Terashima, T., Carrington, A., Matsuda, Y., and Shibauchi, T. (2012). Nodal versus Nodeless Behavior of the Order Parameters of LiFeP and LiFeAs Superconductors from Magnetic Penetration-Depth Measurements. *Phys. Rev. Lett.*, 108:047003.

Hashimoto, K., Yamashita, M., Kasahara, S., Senshu, Y., Nakata, N., Tonegawa, S., Ikada, K., Serafin, A., Carrington, A., Terashima, T., Ikeda, H., Shibauchi, T., and Matsuda, Y. (2010). Line nodes in the energy gap of superconducting $BaFe_2(As_{1-x}P_x)_2$ single crystals as seen via penetration depth and thermal conductivity. *Phys. Rev. B. Rapid*, 81:220501.

Helfand, E. and Werthamer, N. R. (1964). Temperature and Purity Dependence of the Superconducting Critical Field, H_{c2}. *Phys. Rev. Lett.*, 13:686.

Helfand, E. and Werthamer, N. R. (1966). Temperature and Purity Dependence of the Superconducting Critical Field H_{c2} II. *Phys. Rev. Lett.*, 147:288.

Hodovanets, H., Mun, E. D., Thaler, A., Bud'ko, S. L., and Canfield, P. C. (2011). Thermoelectric power of $Ba(Fe_{1-x}Ru_x)_2As_2$ and$Ba(Fe_{1-x}Co_x)_2As_2$: Possible changes of Fermi surface with and without changes in electron count. *Phys. Rev. B*, 83(9):094508.

Hohenberg, P. C. and Werthamer, N. R. (1967). Anisotropy and Temperature Dependence of the Upper Critical Field of Type-II Superconductors. *Phys. Rev.*, 153:493.

Hu, R., Bud'ko, S. L., Straszheim, W. E., and Canfield, P. C. (2011). Phase diagram of superconductivity and antiferromagnetism in single crystals of $Sr(Fe_{1-x}Co_x)_2As_2$ and $Sr_{1-y}Eu_y(Fe_{0.88}Co_{0.12})_2As_2$. *Phys. Rev. B*, 83:094520.

Huang, Q., Qiu, Y., Bao, W., Green, M. A., Lynn, J. W., Gasparovic, Y. C., T. Wu, G. W., and Chen, X. H. (2008). Neutron-Diffraction Measurements of Magnetic Order and a Structural Transition in the Parent $BaFe_2As_2$ Compound of FeAs-Based High-Temperature Superconductors. *Phys. Rev. Lett.*, 101:257003.

Jiang, S., Xing, H., Xuan, G., Wang, C., Ren, Z., Feng, C., Dai, J., Xu, Z., and Cao, G.

(2009). Superconductivity up to 30 K in the vicinity of the quantum critical point in $BaFe_2(As_{1-x}P_x)_2$. *Journal of Physics: Condensed Matter*, 21(38):382203.

Kamihara, Y., Hiramatsu, H., Hirano, M., Kawamura, R., Yanagi, H., Kamiya, T., and Hosono, H. (2006). Iron-Based Layered Superconductor: LaOFeP. *Journal of the American Chemical Society*, 128(31):10012–10013. PMID: 16881620.

Kamihara, Y., Watanabe, T., Hirano, M., and Hosono, H. (2008). Iron-Based Layered Superconductor $La(O_{1-x}F_x)FeAs$ (x = 0.05-0.12) with T_c = 26 K. *Journal of the American Chemical Society*, 130(11):3296.

Kasahara, S., Shibauchi, T., Hashimoto, K., Ikada, K., Tonegawa, S., Okazaki, R., Shishido, H., Ikeda, H., Takeya, H., Hirata, K., Terashima, T., and Matsuda, Y. (2010). Evolution from non-Fermi- to Fermi-liquid transport via isovalent doping in $BaFe_2(As_{1-x}P_x)_2$ superconductors. *Phys. Rev. B*, 81(18):184519.

Khasanov, R., Bendele, M., Bussmann-Holder, A., and Keller, H. (2010a). Intrinsic and structural isotope effects in iron-based superconductors. *Phys. Rev. B*, 82:212505.

Khasanov, R., Bendele, M., Conder, K., Keller, H., Pomjakushina, E., and Pomjakushin, V. (2010b). Iron isotope effect on the superconducting transition temperature and the crystal structure of $FeSe_{1-x}$. *New Journal of Physics*, 12:073024.

Khasanov, R., Shengelaya, A., Castro, D. D., Morenzoni, E., Maisuradze, A., Savic, I. M., Conder, K., Pomjakushina, E., Bussmann-Holder, A., and Keller, H. (2008). *Phys. Rev. Lett.*, 101:077001.

Khasanov, R., Shengelaya, A., Morenzoni, E., Conder, K., Savić, I. M., and Keller, H. (2004). *J. Phys.: Condens. Matter*, 16:S4439.

Kim, M. G., Fernandes, R. M., Kreyssig, A., Kim, J. W., Thaler, A., Bud'ko, S. L., Canfield, P. C., McQueeney, R. J., Schmalian, J., and Goldman, A. I. (2011a). Character of the structural and magnetic phase transitions in the parent and electron-doped $BaFe_2As_2$ compounds. *Phys. Rev. B*, 83:134522.

Kim, M. G., Kreyssig, A., Lee, Y. B., Kim, J. W., Pratt, D. K., Thaler, A., Bud'ko, S. L., Canfield, P. C., Harmon, B. N., McQueeney, R. J., and Goldman, A. I. (2010a). Commensurate antiferromagnetic ordering in $Ba(Fe_{1-x}Co_x)_2As_2$ determined by x-ray resonant magnetic scattering at the Fe, K edge. *Phys. Rev. B.*, 82:180412.

Kim, M. G., Kreyssig, A., Thaler, A., Pratt, D. K., Tian, W., Zarestky, J. L., Green, M. A., Bud'ko, S. L., Canfield, P. C., McQueeney, R. J., and Goldman, A. I. (2010b). Antiferromagnetic ordering in the absence of structural distortion in $Ba(Fe_{1-x}Mn_x)_2As_2$. *Phys. Rev. B*, 82(22):220503.

Kim, M. G., Pratt, D. K., Rustan, G. E., Tian, W., Zarestky, J. L., Thaler, A., Bud'ko, S. L., Canfield, P. C., McQueeney, R. J., Kreyssig, A., and Goldman, A. I. (2011b). Magnetic ordering and structural distortion in Ru-doped $BaFe_2As_2$ single crystals studied by neutron and x-ray diffraction. *Phys. Rev. B*, 83:054514.

Kim, S. K., Torikachvili, M. S., Colombier, E., Thaler, A., Bud'ko, S. L., and Canfield, P. C. (2011c). Combined effects of pressure and Ru substitution on $BaFe_2As_2$. *Phys. Rev. B*, 84:134525.

Kimber, S. A. J., Kreyssig, A., Zhang, Y.-Z., Jeschke, H. O., Valenti, R., Yokaichiya, F., Colombier, E., Yan, J., Hansen, T. C., Chatterji, T., McQueeney, R. J., Canfield, P. C., Goldman, A. I., and Argyriou, D. N. (2009). Similarities between structural distortions under pressure and chemical doping in superconducting $BaFe_2As_2$. *Nat Mater*, 8(6):471–475.

Kogan, V. G. (2009). Pair breaking in iron pnictides. *Phys. Rev. B*, 80:214532.

Kogan, V. G. and Schmalian, J. (2011). Ginzburg-landau theory of two-band superconductors: Absence of type-1.5 superconductivity. *Phys. Rev. B*, 83:054515.

Kreyssig, A., Kim, M. G., Nandi, S., Pratt, D. K., Tian, W., Zarestky, J. L., Ni, N., Thaler, A., Bud'ko, S. L., Canfield, P. C., McQueeney, R. J., and Goldman, A. I. (2010). Suppression of antiferromagnetic order and orthorhombic distortion in superconducting $Ba(Fe_{0.961}Rh_{0.039})_2As_2$. *Phys. Rev. B*, 81(13):134512.

Lester, C., Chu, J.-H., Analytis, J. G., Capelli, S. C., Erickson, A. S., Condron, C. L., Toney, M. F., Fisher, I. R., and Hayden, S. M. (2009). Neutron scattering study of the interplay between structure and magnetism in Ba(Fe$_{1-x}$Co$_x$)$_2$As$_2$. *Phys. Rev. B*, 79(14):144523.

Li, L. J., Luo, Y. K., Wang, Q. B., Chen, H., Ren, Z., Tao, Q., Li, Y. K., Lin, X., He, M., Zhu, Z. W., Cao, G. H., and Xu, Z. A. (2009). Superconductivity induced by Ni doping in BaFe$_2$As$_2$ single crystals. *New Journal of Physics*, 11(2):025008.

Lifshitz, I. M. (1960). Anomalies of electron characteristics of a metal in the high pressure region. *Soviet Physics JETP*, 11:1130–1135.

Liu, C., Kondo, T., Fernandes, R. M., Palczewski, A. D., Mun, E. D., Ni, N., Thaler, A. N., Bostwick, A., Rotenberg, E., Schmalian, J., Bud'ko, S. L., Canfield, P. C., and Kaminski, A. (2010). Evidence for a Lifshitz transition in electron-doped iron arsenic superconductors at the onset of superconductivity. *Nat Phys*, 6(6):419–423.

Liu, C., Palczewski, A. D., Dhaka, R. S., Kondo, T., Fernandes, R. M., Mun, E. D., Hodovanets, H., Thaler, A. N., Schmalian, J., Bud'ko, S. L., Canfield, P. C., and Kaminski, A. (2011). Importance of the Fermi-surface topology to the superconducting state of the electron-doped pnictide Ba(Fe$_{1-x}$Co$_x$)$_2$As$_2$. *Phys. Rev. B*, 84:020509.

Liu, R. H., Wu, T., Wu, G., Chen, H., Wang, X. F., Xie, Y. L., Yin, J. J., Yan, Y. J., Li, Q. J., Shi, B. C., Chu, W. S., Wu, Z. Y., and Chen, X. H. (2009). *Nature*, 459:64.

London, F. and London, H. (1935). The Electromagnetic Equations of the Supraconductor. *Proc. Roy. Soc. A*, 149:71.

Luetkens, H., Klauss, H. H., Kraken, M., Litterst, F. J., Dellmann, T., Klingeler, R., Hess, C., Khasanov, R., Amato, A., Baines, C., Kosmala, M., Schumann, O. J., Braden, M., Hamann-Borrero, J., Leps, N., Kondrat, A., Behr, G., Werner, J., and Buchner, B. (2009). The electronic phase diagram of the LaO$_{1-x}$F$_x$FeAs superconductor. *Nat Mater*, 8(4):305–309.

Lumsden, M. D., Christianson, A. D., Parshall, D., Stone, M. B., Nagler, S. E., MacDougall, G. J., Mook, H. A., Lokshin, K., Egami, T., Abernathy, D. L., Goremychkin, E. A., Osborn,

R., McGuire, M. A., Sefat, A. S., Jin, R., Sales, B. C., and Mandrus, D. (2009). Two-dimensional resonant magnetic excitation in $BaFe_{1.84}Co_{0.16}As_2$. *Phys. Rev. Lett.*, 102:107005.

Luo, H., Wang, Z., Yang, H., Cheng, P., Zhu, X., and Wen, H.-H. (2008). Growth and characterization of $A_{1-x}K_xFe_2As_2$ (A = Ba, Sr) single crystals with $= 0 - 0.4$. *Superconductor Science and Technology*, 21(12):125014.

Maple, M. B., Bauer, E. D., Zapf, V. S., and Wosnitza, J. (2008). *Superconductivity: Volume 1, Conventional and Unconventional Superconductors*. Springer.

Martin, C., Kim, H., Gordon, R. T., Ni, N., Thaler, A., Kogan, V. G., Bud'ko, S. L., Canfield, P. C., Tanatar, M. A., and Prozorov, R. (2010). The London penetration depth in $BaFe_2As_2$ superconductors at high electron doping level. *Superconductor Science and Technology*, 23:065022.

Marty, K., Christianson, A. D., Wang, C. H., Matsuda, M., Cao, H., VanBebber, L. H., Zarestky, J. L., Singh, D. J., Sefat, A. S., and Lumsden, M. D. (2011). Competing magnetic ground states in nonsuperconducting $Ba(Fe_{1-x}Cr_x)_2As_2$ as seen via neutron diffraction. *Phys. Rev. B*, 83(6):060509.

Maxwell, E. (1950). Isotopy effect in the superconductivity of mercury. *Phys. Rev.*, 78:477.

Meissner, W. and Ochsenfeld, R. (1933). Ein neuer Effekt bei Eintritt der Supraleitfähigkeit. *Naturwissenschaften*, 21:787–788. 10.1007/BF01504252.

Miao, H., Richard, P., Tanaka, Y., Nakayama, K., Qian, T., Umezawa, K., Sato, T., Xu, Y.-M., Shi, Y. B., Xu, N., Wang, X.-P., Zhang, P., Yang, H.-B., Xu, Z.-J., Wen, J. S., Gu, G.-D., Dai, X., Hu, J.-P., Takahashi, T., and Ding, H. (2012). Isotropic superconducting gaps with enhanced pairing on electron fermi surfaces in $FeTe_{0.55}Se_{0.45}$. *Phys. Rev. B*, 85:094506.

Mun, E. D., Bud'ko, S. L., Ni, N., Thaler, A. N., and Canfield, P. C. (2009). Thermoelectric power and Hall coefficient measurements on $Ba(Fe_{1-x}T_x)_2As_2$ (T=Co and Cu). *Phys. Rev. B*, 80(5):054517.

Nakai, Y., Iye, T., Kitagawa, S., Ishida, K., Kasahara, S., Shibauchi, T., Matsuda, Y., and Terashima, T. (2010). ^{31}P and ^{75}As NMR evidence for a residual density of states at zero energy in superconducting BaFe$_2$(As$_{0.67}$P$_{0.33}$)$_2$. *Phys. Rev. B. Rapid*, 81:020503.

Nandi, S., Kim, M. G., Kreyssig, A., Fernandes, R. M., Pratt, D. K., Thaler, A., Ni, N., Bud'ko, S. L., Canfield, P. C., Schmalian, J., McQueeney, R. J., and Goldman, A. I. (2010). Anomalous Suppression of the Orthorhombic Lattice Distortion in Superconducting Ba(Fe$_{1-x}$Co$_x$)$_2$As$_2$ Single Crystals. *Phys. Rev. Lett.*, 104:057006.

Neupane, M., Richard, P., Xu, Y.-M., Nakayama, K., Sato, T., Takahashi, T., Federov, A. V., Xu, G., Dai, X., Fang, Z., Wang, Z., Chen, G.-F., Wang, N.-L., Wen, H.-H., and Ding, H. (2011). Electron-hole asymmetry in the superconductivity of doped BaFe$_2$As$_2$ seen via the rigid chemical-potential shift in photoemission. *Phys. Rev. B*, 83:094522.

Ni, N. (2009). *Structural / magnetic phase transitions and superconductivity in Ba(Fe$_{1-x}$TM$_x$)$_2$As$_2$ (TM=Co, Ni, Cu, Co / Cu, Rh and Pd) single crystals*. PhD thesis, Iowa State University.

Ni, N., Bud'ko, S. L., Kreyssig, A., Nandi, S., Rustan, G. E., Goldman, A. I., Gupta, S., Corbett, J. D., Kracher, A., and Canfield, P. C. (2008a). Anisotropic thermodynamic and transport properties of single-crystalline (Ba$_{1-x}$K$_x$)Fe$_2$As$_2$ ($x = 0$ and 0.45). *Phys. Rev. B*, 78:014507.

Ni, N., Thaler, A., Kracher, A., Yan, J. Q., Bud'ko, S. L., and Canfield, P. C. (2009). Phase diagrams of Ba(Fe$_{1-x}$TM$_x$)$_2$As$_2$ (TM = Rh, Pd) single crystals. *Phys. Rev. B*, 80(2):024511.

Ni, N., Thaler, A., Yan, J. Q., Kracher, A., Colombier, E., Bud'ko, S. L., Canfield, P. C., and Hannahs, S. T. (2010). Temperature versus doping phase diagrams for Ba(Fe$_{1-x}$TM$_x$)$_2$As$_2$ (TM=Ni, Cu, Cu/Co) single crystals. *Phys. Rev. B*, 82:024519.

Ni, N., Tillman, M. E., Yan, J.-Q., Kracher, A., Hannahs, S. T., Bud'ko, S. L., and Canfield, P. C. (2008b). Effects of Co substitution on thermodynamic and transport properties and anisotropic H$_{c2}$ in Ba(Fe$_{1-x}$Co$_x$)$_2$As$_2$ single crystals. *Phys. Rev. B*, 78(21):214515.

Ofer, O., Baglo, J. C., Hossain, M. D., Kiefl, R. F., Hardy, W. N., Thaler, A., Kim, H., Tanatar, M. A., Canfield, P. C., Prozorov, R., Luke, G. M., Morenzoni, E., Saadaoui, H., Suter, A., Prokscha, T., Wojek, B. M., and Salman, Z. (2012). Absolute value and temperature dependence of the magnetic penetration depth in $Ba(Co_{0.074}Fe_{0.926})_2As_2$. *Phys. Rev. B*, 85:060506.

Okada, H., Igawa, K., Takahashi, H., Kamihara, Y., Hirano, M., Hosono, H., Matsubayashi, K., and Uwatoko, Y. (2008). Superconductivity under High Pressure in LaFeAsO. *Journal of the Physical Society of Japan*, 77(11):113712.

Onnes, H. K. (1911). The resistance of pure mercury at helium temperatures. *Commun. Phys. Lab. Univ. Leiden*, 12:120.

Pandey, A., Anand, V. K., and Johnston, D. C. (2011). Large miscibility gap in the $Ba(Mn_xFe_{1-x})_2As_2$ system. *Phys. Rev. B*, 84:014405.

Pfisterer, M. and Nagorsen, G. (1980). *Zeitschrift für Naturforschung*, 35:703.

Pratt, D. K., Kim, M. G., Kreyssig, A., Lee, Y. B., Tucker, G. S., Thaler, A., Tian, W., Zarestky, J. L., Bud'ko, S. L., Canfield, P. C., Harmon, B. N., Goldman, A. I., and McQueeney, R. J. (2011). Incommensurate Spin-Density Wave Order in Electron-Doped $BaFe_2As_2$ Superconductors. *Phys. Rev. Lett.*, 106:257001.

Pratt, D. K., Kreyssig, A., Nandi, S., Ni, N., Thaler, A., Lumsden, M. D., Tian, W., Zarestky, J. L., Bud'ko, S. L., Canfield, P. C., Goldman, A. I., and McQueeney, R. J. (2010). Dispersion of the superconducting spin resonance in underdoped and antiferromagnetic $BaFe_2As_2$. *Phys. Rev. B*, 81:140510.

Pratt, D. K., Tian, W., Kreyssig, A., Zarestky, J. L., Nandi, S., Ni, N., Bud'ko, S. L., Canfield, P. C., Goldman, A. I., and McQueeney, R. J. (2009). Coexistence of Competing Antiferromagnetic and Superconducting Phases in the Underdoped $Ba(Fe_{0.953}Co_{0.047})_2As_2$ Compound Using X-ray and Neutron Scattering Techniques. *Phys. Rev. Lett.*, 103(8):087001.

Qi, Y., Wang, L., Gao, Z., Wang, D., Zhang, X., and Ma, Y. (2009). Superconductivity induced by doping Ru in SrFe$_{2-x}$Ru$_x$As$_2$. *Physica C: Superconductivity*, 469(21):1921 – 1924.

Qiu, X., Zhou, S. Y., Zhang, H., Pan, B. Y., Hong, X. C., Dai, Y. F., Eom, M. J., Kim, J. S., Ye, Z. R., Zhang, Y., Feng, D. L., and Li, S. Y. (2012). Robust Nodal Superconductivity Induced by Isovalent Doping in Ba(Fe$_{1-x}$Ru$_x$)$_2$As$_2$ and BaFe$_2$(As$_{1-x}$P$_x$)$_2$. *Phys. Rev. X.*, 2:011010.

Ran, S., Bud'ko, S. L., Pratt, D. K., Kreyssig, A., Kim, M. G., Kramer, M. J., Ryan, D. H., Rowan-Weetaluktuk, W. N., Furukawa, Y., Roy, B., Goldman, A. I., and Canfield, P. C. (2011). Stabilization of an ambient-pressure collapsed tetragonal phase in CaFe$_2$As$_2$ and tuning of the orthorhombic-antiferromagnetic transition temperature by over 70 K via control of nanoscale precipitates. *Phys. Rev. B*, 83:144517.

Reynolds, C. A., Serin, B., Wright, W. H., and Nesbitt, L. B. (1950). Superconductivity of Isotopes of Mercury. *Phys. Rev.*, 78:487.

Rotter, M., Tegel, M., and Johrendt, D. (2008a). Superconductivity at 38 K in the Iron Arsenide (Ba$_{1-x}$K$_x$)Fe$_2$As$_2$. *Phys. Rev. Lett.*, 101(10):107006.

Rotter, M., Tegel, M., Johrendt, D., Schellenberg, I., Hermes, W., and Pottgen, R. (2008b). Spin-density-wave anomaly at 140 K in the ternary iron arsenide BaFe$_2$As$_2$. *Phys. Rev. B*, 78(2):020503.

Rullier-Albenque, F., Colson, D., Forget, A., Thuéry, P., and Poissonnet, S. (2010). Hole and electron contributions to the transport properties of Ba(Fe$_{1-x}$Ru$_x$)$_2$As$_2$ single crystals. *Phys. Rev. B*, 81(22):224503.

Saha, S. R., Butch, N. P., Kirshenbaum, K., Paglione, J., and Zavalij, P. Y. (2009). Superconducting and Ferromagnetic Phases Induced by Lattice Distortions in Stoichiometric SrFe$_2$As$_2$ Single Crystals. *Phys. Rev. Lett.*, 103:037005.

Schnelle, W., Leithe-Jasper, A., Gumeniuk, R., Burkhardt, U., Kasinathan, D., and Rosner,

H. (2009). Substitution-induced superconductivity in $SrFe_{2-x}Ru_xAs_2$ ($0 \leq x \leq 2$). *Phys. Rev. B*, 79(21):214516.

Sefat, A. S., Huq, A., McGuire, M. A., Jin, R., Sales, B. C., Mandrus, D., Cranswick, L. M. D., Stephens, P. W., and Stone, K. H. (2008a). Superconductivity in $LaFe_{1-x}Co_xAsO$. *Phys. Rev. B*, 78(10):104505.

Sefat, A. S., Jin, R., McGuire, M. A., Sales, B. C., Singh, D. J., and Mandrus, D. (2008b). Superconductivity at 22 K in Co-Doped $BaFe_2As_2$ Crystals. *Phys. Rev. Lett.*, 101(11):117004.

Sefat, A. S., Singh, D. J., Jin, R., McGuire, M. A., Sales, B. C., and Mandrus, D. (2009a). Renormalized behavior and proximity of $BaCo_2As_2$ to a magnetic quantum critical point. *Phys. Rev. B*, 79(2):024512.

Sefat, A. S., Singh, D. J., VanBebber, L. H., Mozharivskyj, Y., McGuire, M. A., Jin, R., Sales, B. C., Keppens, V., and Mandrus, D. (2009b). Absence of superconductivity in hole-doped $BaFe_{2-x}Cr_xAs_2$ single crystals. *Phys. Rev. B*, 79(22):224524.

Senga, Y. and Kontani, H. (2008). Impurity effects in sign-reversing fully gapped superconductors: Analysis of feas superconductors. *Journal of the Physical Society of Japan*, 77(11):113710.

Sharma, S., Bharathi, A., Chandra, S., Reddy, V. R., Paulraj, S., Satya, A. T., Sastry, V. S., Gupta, A., and Sundar, C. S. (2010). Superconductivity in Ru-substituted polycrystalline $BaFe_{2-x}Ru_xAs_2$. *Phys. Rev. B*, 81(17):174512.

Shirage, P. M., Kihou, K., Miyazawa, K., Lee, C. H., Kito, H., Eisaki, H., Yanagisawa, T., Tanaka, Y., and Iyo, A. (2009). *Phys. Rev. Lett.*, 103:257003.

Shirage, P. M., Miyazawa, K., Kihou, K., Kito, H., Yoshida, Y., Tanaka, Y., Eisaki, H., and Iyo, A. (2010). *Phys. Rev. Lett.*, 105:037004.

Singh, Y., Ellern, A., and Johnston, D. C. (2009). Magnetic, transport, and thermal properties of single crystals of the layered arsenide $BaMn_2As_2$. *Phys. Rev. B*, 79(9):094519.

Skalski, S., Betbeder-Matibet, O., and Weiss, P. R. (1964). Properties of Superconducting Alloys Containing Paramagnetic Impurities. *Phys. Rev.*, 136:A1500.

Song, C.-L., Wang, Y.-L., Cheng, P., Jiang, Y.-P., Li, W., Zhang, T., Li, Z., He, K., Wang, L., Jia, J.-F., Hung, H.-H., Wu, C., Ma, X., Chen, X., and Xue, Q.-J. (2011). Direct Observation of Nodes and Twofold Symmetry in FeSe Superconductor. *Science*, 332(6036):1410–1413.

Stewart, G. R. (2001). Non-Fermi-liquid behavior in d- and f-electron metals. *Rev. Mod. Phys.*, 73:797–855.

Takahashi, H., Kazumi Igawa, K. A., Kamihara, Y., Hirano, M., and Hosono, H. (2008). Superdonductivity at 43 K in an iron-based layered compound $LaO_{1-x}F_xFeAs$. *Nature*, 453:376–378.

Tallon, J. L., Islam, R. S., Storey, J., Williams, G. V. M., and Cooper, J. R. (2005). *Phys. Rev. Lett.*, 94:237002.

Tanatar, M. A., Blomberg, E. C., Kreyssig, A., Kim, M. G., Ni, N., Thaler, A., Bud'ko, S. L., Canfield, P. C., Goldman, A. I., Mazin, I. I., and Prozorov, R. (2010a). Uniaxial-strain mechanical detwinning of $CaFe_2As_2$ and $BaFe_2As_2$ crystals: Optical and transport study. *Phys. Rev. B*, 81:184508.

Tanatar, M. A., Ni, N., Martin, C., Gordon, R. T., Kim, H., Kogan, V. G., Samolyuk, G. D., Bud'ko, S. L., Canfield, P. C., and Prozorov, R. (2009a). Anisotropy of the iron pnictide superconductor $Ba(Fe_{1-x}Co_2)_2As_2$ (x = 0.074, T_c = 23 K). *Phys. Rev. B*, 79(9):094507.

Tanatar, M. A., Ni, N., Samolyuk, G. D., Bud'ko, S. L., Canfield, P. C., and Prozorov, R. (2009b). Resistivity anisotropy of AFe_2As_2 (A = Ca, Sr, Ba): Direct versus Montgomery technique measurements. *Phys. Rev. B*, 79(13):134528.

Tanatar, M. A., Ni, N., Thaler, A., Bud'ko, S. L., Canfield, P. C., and Prozorov, R. (2010b). Pseudogap and its critical point in the heavily doped $Ba(Fe_{1-x}Co_x)_2As_2$ from c-axis resistivity measurements. *Phys. Rev. B*, 82:134528.

Tanatar, M. A., Ni, N., Thaler, A., Bud'ko, S. L., Canfield, P. C., and Prozorov, R. (2011). Systematics of the temperature-dependent interplane resistivity in Ba(Fe$_{1-x}$M$_x$)$_2$As$_2$ (M=Co, Rh, Ni, and Pd). *Phys. Rev. B*, 84:014519.

Terashima, K., Sekiba, Y., Bowen, J. H., Nakayama, K., Kawahara, T., Sato, T., Richard, P., Xu, Y.-M., Li, L. J., Cao, G. H., Xu, Z.-A., Ding, H., and Takahashi, T. (2009). Fermi surface nesting induced strong pairing in iron-based superconductors. *Proc. Natl. Acad. Sci. U.S.A.*, 106(18):7330.

Thaler, A., Hodovanets, H., Torikachvili, M. S., Ran, S., Kracher, A., Straszheim, W., Yan, J. Q., Mun, E., and Canfield, P. C. (2011). Physical and magnetic properties of Ba(Fe$_{1-x}$Mn$_x$)$_2$As$_2$ single crystals. *Phys. Rev. B*, 84:144528.

Thaler, A., Ni, N., Kracher, A., Yan, J. Q., Bud'ko, S. L., and Canfield, P. C. (2010). Physical and magnetic properties of Ba(Fe$_{1-x}$Ru$_x$)$_2$As$_2$ single crystals. *Phys. Rev. B*, 82(1):014534.

Tinkham, M. (2004). *Introduction to Superconductivity*. Dover, 2nd edition.

Torikachvili, M. S., Bud'ko, S. L., Ni, N., and Canfield, P. C. (2008). Effect of pressure on the structural phase transition and superconductivity in (Ba$_{1-x}$K$_x$)Fe$_2$As$_2$($x = 0$ and 0.45) and SrFe$_2$As$_2$ single crystals. *Phys. Rev. B*, 78(10):104527.

Torikachvili, M. S., Bud'ko, S. L., Ni, N., Canfield, P. C., and Hannahs, S. T. (2009). Effect of pressure on transport and magnetotransport properties in CaFe$_2$As$_2$ single crystals. *Phys. Rev. B*, 80:014521.

Vavilov, M. G. and Chubukov, A. V. (2011). Phase diagram of iron pnictides if doping acts as a source of disorder. *Physical Review B*, 84(21):214521–.

Wang, P., Stadnik, Z. M., Żukrowski, J., Thaler, A., Bud'ko, S. L., and Canfield, P. C. (2011). Coexistence of antiferromagnetic ordering and superconductivity in the Ba(Fe$_{0.961}$Rh$_{0.039}$)$_2$As$_2$ compound studied by Mössbauer spectroscopy. *Phys. Rev. B*, 84:024509.

Werthamer, N. R., Helfand, E., and Hohenberg, P. C. (1966). Temperature and Purity Dependence of the Superconducting Critical Field H_{c2} III Electron Spin and Spin-Orbit Effects. *Phys. Rev.*, 147:295.

Werthamer, N. R. and McMillan, W. L. (1967). Temperature and Purity Dependence of the Superconducting Critical Field H_{c2} IV. Strong-Coupling Effects. *Phys. Rev.*, 158:415.

Wu, J. and Phillips, P. (2011). Magnon-mediated pairing and isotope effect in iron-based superconductors. *Journal of Physics: Condensed Matter*, 23(9):094203.

Wu, M. K., Ashburn, J. R., Torng, C. J., Hor, P. H., Meng, R. L., Gao, L., Huang, Z. J., Wang, Y. Q., and Chu, C. W. (1987). Superconductivity at 93 K in a new mixed-phase Yb-Ba-Cu-O compound system at ambient pressure. *Phys. Rev. Lett.*, 58:908.

Xu, Y.-M., Richard, P., Nakayama, K., Kawahara, T., Sekiba, Y., Qian, T., Neupane, M., Souma, S., Sato, T., Takahashi, T., Luo, H.-Q., Wen, H.-H., Chen, G.-F., Wang, N.-L., Wang, Z., Fang, Z., Dai, X., and Ding, H. (2011). Fermi surface dichotomy of the superconducting gap and pseudogap in underdoped pnictides. *Nature Communications*, 2:392.

Yamashita, M., Senshu, Y., Shibauchi, T., Kasahara, S., Hashimoto, K., Watanabe, D., Ikeda, H., Terashima, T., Vekhter, I., Vorontsov, A. B., and Matsuda, Y. (2011). Nodal gap structure of superconducting $BaFe_2(As_{1-x}P_x)_2$ from angle-resolved thermal conductivity in a magnetic field. *Phys. Rev. B. Rapid*, 84:060507.

Yu, W., Aczel, A. A., Williams, T. J., Bud'ko, S. L., Ni, N., Canfield, P. C., and Luke, G. M. (2009). Absence of superconductivity in single-phase $CaFe_2As_2$ under hydrostatic pressure. *Phys. Rev. B*, 79:020511.

Zech, D., Keller, H., Conder, K., Kaldis, E., Liarokapis, E., Poulakis, N., and Müller, K. A. (1994). *Nature*, 371:681.

Zhang, Y., Yang, L. X., Xu, M., Ye, Z. R., Chen, F., He, C., Xu, H. C., Jiang, J., Xie, B. P., Ying, J. J., Wang, X. F., Chen, X. H., Hu, J. P., Matsunami, M., Kimura, S., and

Feng, D. L. (2011). Nodeless superconducting gap in $A_x Fe_2 Se_2$ (A=K,Cs) revealed by angle-resolved photoemission spectroscopy. *Nature Materials*, 10:273–277.

Zhang, Y., Ye, Z. R., Ge, Q. Q., Chen, F., Jiang, J., Xu, M., Xie, B. P., and Feng, D. L. (2012). Nodal superconducting-gap stricture in ferropnictide superconductor $BaFe_2(As_{0.7}P_{0.3})_2$. *Nature Physics*, 8(5):371–375.

Zhao, G. M., Keller, H., and Conder, K. (2001). *J. Phys.: Condens. Matter*, 13:R569.

Zhao, J., Huang, Q., de la Cruz, C., Li, S., Lynn, J. W., Chen, Y., Green, M. A., Chen, G. F., Li, G., Li, Z., Luo, J. L., Wang, N. L., and Dai, P. (2008). Structural and magnetic phase diagram of $CeFeAsO_{1-x}F_x$ and its relation to high-temperature superconductivity. *Nat Mater*, 7(12):953–959.

Zhi-An, R., Wei, L., Jie, Y., Wei, Y., Xiao-Li, S., Zheng-Cai, Guang-Can, C., Xiao-Li, D., Li-Ling, S., Fang, Z., and Zhong-Xian, Z. (2008). Superconductivity at 55 K in Iron-Based F-Doped Layered Quaternary Compound $Sm[O_{1-x}F_x]FeAs$. *Chinese Physics Letters*, 25(6):2215.